Ørnulf Nordseth

Ferroelectric Thin Films for Planar Photonic Device Applications

Thesis for the degree of Philosophiae Doctor

Trondheim, May 2010

Faculty of Information Technology, Mathematics
and Electrical Engineering
Department of Electronics and Telecommunications

NTNU
Norwegian University of
Science and Technology

NTNU
Norwegian University of Science and Technology

Thesis for the degree of Philosophiae Doctor

Faculty of Information Technology, Mathematics and Electrical Engineering
Department of Electronics and Telecommunications

© Ørnulf Nordseth

ISBN 978-82-471-2076-7 (printed ver.)
ISBN 978-82-471-2077-4 (electronic ver.)
ISSN 1503-8181

Doctoral theses at NTNU, 2010:60

Printed by NTNU-trykk

Preface

This dissertation is submitted in partial fulfillment of the requirements for the degree of Philosophae Doctor (PhD) at the Norwegian University of Science and Technology (NTNU). The work was carried out at Department of Electronics and Telecommunications with Prof. Jostein K. Grepstad and Prof. Thomas Tybell as thesis supervisors. Parts of the dissertation have been published in the scientific literature.

- Ø. Nordseth, C. C. You, E. Folven, S. Gariglio, A. Sambri, J. -M. Triscone, J. W. Reiner, C. H. Ahn, T. Tybell, and J. K. Grepstad, "Growth and characterization of (Pb,La)(Zr,Ti) O_3 thin film epilayers on $SrTiO_3$-buffered Si(001)," accepted for publication in Thin Solid Films.
- Ø. Nordseth, J. Ø. Kjellman, C. C. You, A. Røyset, T. Tybell, and J. K. Grepstad, "The case for electro-optic waveguides in ferroelectric (Pb,La)(Zr,Ti)O_3 thin film epilayers," Proc. of SPIE vol. 7381, pp. 73810F-1–73810F-13 (2009).
- Ø. Nordseth, A. Røyset, T. Tybell, and J. K. Grepstad, "Sputter-deposited (Pb,La)(Zr,Ti)O_3 thin films: Effect of substrate and optical properties," J. Vac. Sci. Technol. A vol. 27, pp. 548–553 (2009).
- Ø. Nordseth, T. Tybell, and J. K. Grepstad, "Epitaxial (Pb,La) (Zr,Ti)O_3 thin films on buffered Si(100) by on-axis radio frequency magnetron sputtering," Thin Solid Films vol. 517, pp. 2623–2626 (2009).

- Ø. Nordseth, T. Tybell, and J. K. Grepstad, "Simulation of photonic band gap waveguides in lead-lanthanum zirconate-titanate," in: 2006 Northern Optics Conference Proceedings, pp. 51-54 (2007).

All experiments and numerical modelling reported in this thesis were conducted by the author, except for the following. The model used for numerical fitting of the prism coupling data was developed by Dr. Arne Røyset, SINTEF Materials and Chemistry. The STO-buffered Si(001) substrates were obtained from Prof. Charles Ahn's group at Yale University, Connecticut, via Dr. Stefano Gariglio at Dept. of Condensed Matter Physics, University of Geneva. The XPS analysis of the STO-buffered Si(001) substrates was performed by Erik Folven, Dept. of Electronics and Telecommunications, NTNU. The grazing incidence x-ray diffraction measurements were carried out by Chang Chuan You, Dept. of Electronics and Telecommunications, NTNU, and Jon Øyvind Kjellman, Dept. of Electronics and Telecommunications, NTNU, helped with the electro-optic modulation experiments.

Acknowledgements

I am very grateful for having been offered the opportunity to work at an academic institution for several years, where I have found great inspiration from experienced and enthusiastic colleagues. I would like to acknowledge Jostein K. Grepstad and Thomas Tybell for assistance during the project. I also wish to acknowledge Ralph W. Bernstein for his contributions in the early stage of the project. The assistance and support from other PhD students and post docs in the *oxide electronics group* have been of great value. Chang Chuan You is acknowledged for technical assistance with the atomic force microscope measurements and for his efforts in the Nanoxide project. I wish to thank Øystein Dahl for assistance with operation of the sputter deposition system and the ferroelectric characterization tool. Espen Eberg offered help with the x-ray diffraction measurements and the tripod polishing. Erik Folven is acknowledged for providing detailed instructions on the operation of the x-ray photoelectron and Auger electron spectrometers. Several researchers and staff members

of the Department research groups in Electro-optics and Electronic Devices and Materials are also acknowledged for fruitful discussions and help during the course of my research project.

I greatly value the collaboration that was initiated with Arne Røyset at SINTEF Materials and Chemistry. We were both involved in the nationally coordinated FUNMAT (Functional Materials and Nanotechnology) program and realized a noticeable overlap for our research projects. Hence, valuable knowledge was exchanged. Lars Johnsen, also with SINTEF Materials and Chemistry, is acknowledged for sharing his experience with photolithography and chemical wet etching.

During 2008, I spent five weeks at Stanford University carrying out experiments with the focused ion beam tool of the Stanford Nanocharacterization Laboratory (SNL). I wish to acknowledge Dr. Il Woong Jung and Dr. J Provine for valuable assistance during my stay at Stanford University.

The process of learning the procedures of fundamental research, as well as facing challenging tasks along the road, have made me develop both professionally and personally. Some of the responsibilities I have undertaken include providing teaching assistance in several MSc courses given at Department of Electronics and Telecommunications and supervising Master students with their thesis assignments. When carrying out a research project that involves experimental physics, it is generally a good idea to look out for options, including opportunities that may shift the direction and focus of the thesis work. As for my project, I certainly have learned that it is very difficult to foresee progression of experimental work. Experiments often tend to be more protracted and time consuming than expected. Sometimes, it feels like all you can do is to perform one more adjustment of a process parameter, be patient, and hope for a more successful outcome the next time. The constant awareness of the fact that it may take weeks and months for a prospering result to occur can be mentally challenging. Fortunately, you attain a considerable amount of knowledge during periods fumbling in the dark, and when you eventually move on to the next stage you may have gained valuable experience. Moreover, you really learn to appreciate the occasions on which you obtain auspicious results. The feeling you get when stumbling across a really interesting observation outweighs all the setbacks and frustration by far.

The project was funded by The Research Council of Norway, under the NANOMAT nationally coordinated project "Oxides for Future Information and Communication Technology", contract no. 158-518/431. A part of the work was financially supported by the EU FP6 project NANOXIDE, NMP contract no. 033191.

Ørnulf Nordseth
Trondheim, Norway
February 2010

Summary

Complex oxides with the perovskite structure offer a variety of physical properties useful to electronic devices. Among this class of *functional* oxides, (Pb,La)(Zr,Ti)O_3 (PLZT) has emerged as an attractive material for photonic device applications by virtue of its high transparency to infrared light and a strong electro-optic response. Although the properties of PLZT were extensively charted in recent decades, this ferroelectric compound has not yet found widespread use in optics. The aim of the present thesis project has been to explore the case for fabrication of planar electro-optic and photonic waveguide devices in epitaxial PLZT thin films. Such devices require films of high crystalline quality and a smooth surface morphology, in order to minimize scattering losses, as well as precise control with the cation stoichiometry to ensure homogeneous physical properties. To this end, on-axis radio frequency magnetron sputtering was adopted for growth of epitaxial PLZT thin films on $SrTiO_3$(001), MgO(001), and buffered Si(001) substrates. The composition of PLZT was chosen with 8 % lanthanum substitution for Pb and a Zr:Ti cation ratio of 40:60, in order to obtain the tetragonal phase with a linear electro-optic response and a large coercive field, characteristics attractive to optical devices, such as modulators, switches, and directional couplers.

X-ray diffraction analysis showed *c*-axis oriented PLZT thin films grown on these substrates, with a rocking curve full width at half maximum of less than 0.3° for the PLZT(001) reflection. It was found that the films were prone to formation of the PLZT pyrochlore phase for substrate temperatures below ∼500°C. The surface and bulk chemical composition of the films were assessed from x-ray photoelectron spectroscopy (XPS) and Auger depth profiling measure-

ments, respectively. The XPS measurements revealed a growing deficiency in Pb with increasing substrate temperature, which spells a deviation from the perovskite cation stoichiometry at the films surface. The recorded Auger depth profiles showed good composition uniformity throughout the PLZT layer. Also, the depth profiles suggest that the $SrTiO_3$ buffer layer serves not only as a template for epitaxial growth, but also as a barrier suppressing Pb-Si interdiffusion between the PLZT layer and the Si substrate.

The ferroelectric characteristics of the films were assessed from recorded polarization vs. electric field (P–E) loops, which showed a remanent polarization $P_\mathrm{r} \approx 35$–40 µm/cm^2 and a coercive field in the range $E_\mathrm{c} = 100$–250 kV/cm. Moreover, it was established from atomic force microscopy measurements that the film surface roughness complies with the requirement for low-loss wave propagation in waveguide devices defined in such films. Optical characterization by prism coupling and spectroscopic ellipsometry measurements was carried out in order to check the thickness and determine the refractive index of the PLZT thin films. For $\lambda = 1.55$ µm, the refractive index was measured at $\sim$2.45. The strong ferroelectric response combined with a smooth surface morphology and a high refractive index open up perspectives for a number of potential applications of these epilayers, ranging from integrated electro-optic devices to non-volatile memory.

The electro-optic properties for PLZT on MgO(001) were investigated by fabrication of a ridge-type Mach-Zehnder interferometer, using UV lithography and chemical wet etching. Transverse electric (TE) polarized light ($\lambda = 1.55$ µm) was coupled into the waveguide device by means of tapered lensed fibers. With a co-planar electrode geometry, electro-optic modulation up to 80 % of the guided light intensity was achieved at a half-wave voltage $V_\pi \approx 150$ V. The corresponding Pockels coefficient was estimated at $\mathfrak{r}_{51} \approx 8.3$ pm/V.

Furthermore, this thesis work includes a theoretical and experimental study of thin film photonic crystals, also known as photonic crystal slabs (PCSs), which offer a promising potential for miniaturization of integrated photonic devices. For a hole-type, air-suspended PLZT PCS with a hexagonal 2D lattice, a photonic band gap for TE-like modes of $\sim$27 % of the mid-gap frequency was obtained

from numerical simulations. PCSs and line-defect waveguides were defined, using focused ion beam etching, in ridge-type waveguides preprocessed in PLZT on MgO(001). Finite-difference time-domain calculations showed that out-of-plane structural asymmetry, such as that introduced by a conical shape of the FIB-etched air holes and the presence of an underlying substrate, impairs the optical isolation properties of the PCS.

List of Abbreviations

AES	Auger Electron Spectroscopy
AFM	Atomic Force Microscope/Microscopy
CW	Continuous Wave
CW	Continuous Wave
ESCA	Electron Spectroscopy for Chemical Analysis
FDTD	Finite-Difference Time-Domain
FIB	Focused Ion Beam
FWHM	Full Width at Half Maximum
HF	Hydrogen Fluoride
HMDS	Hexamethyl Disulizid
IPA	Isopropyl Alcohol
LMIS	Liquid Metal Ion Source
MBE	Molecular Beam Epitaxy
MPB	MIT Photonic-Bands
MZ	Mach-Zehnder
NEMS	Nano-Electro-Mechanical Systems
PBG	Photonic Band Gap

PCS	Photonic Crystal Slab
PLZT	(Pb,La)(Zr,Ti)O_3
PML	Perfectly Matched Layer
PWE	Plane Wave Expansion
RF	Radio Frequency
RMS	Root Mean Square
RSM	Reciprocal Space Map
SEM	Scanning Electron Microscope/Microscopy
SRO	$SrRuO_3$
STO	$SrTiO_3$
TE	Transverse Electric
TM	Transverse Magnetic
TOA	Take-Off Angle
UV	Ultraviolet
XPS	X-ray Photoelectron Spectroscopy
XRD	X-Ray Diffraction
YSZ	Yttria-Stabilized Zirconia

Contents

Chapter 1

Introduction

Future advances of electronic devices and circuitry for sensor technology and information processing are set to rely on new materials as well as on fundamentally new approaches [1]. For example, increased performance of electronic systems may be realized by integrating optical circuits and photonic components with current silicon-based technology [2, 3].

1.1 Perovskite oxides and photonic device applications

Materials with physical properties responding to external forces and variables, such as electric and magnetic fields, temperature, pressure, radiation, etc., are commonly referred to as functional materials. These include a family of ceramic compounds, known as perovskite oxides, which offer a number of attractive functional properties [4], i.e.,

- piezoelectricity - the generation of an electric field in response to applied mechanical stress,
- pyroelectricity - the generation of an electric field in response to a change in temperature,

- ferroelectricity - the presence of a spontaneous electric dipole moment, the direction of which can be switched by application of an external electric field,
- ferromagnetism - the presence of a spontaneous magnetization, the direction of which can be reversed by application of an external magnetic field
- electro-optic effect - a change of optical properties in response to an applied electric field.
- non-linear optic effect - the induction of non-linear polarization in response to an applied electric field.

These functional properties are utilized in a wide variety of electronic devices and microsystem applications, including nonvolatile memory (FeRAM, MRAM) [5–9], ferroelectric field effect transistors [10–12], microelectromechanical systems (MEMS) [13–15], surface acoustic wave devices [16–19], and electroacoustic transducers [20, 21].

Epitaxial integration of perovskite oxide thin films in photonic microsystems is of major technological interest in terms of increased design flexibility and reduced production cost for integrated optics, compared to devices based on bulk crystalline materials. Moreover, such thin film integration opens up for new device concepts. Following recent advances in oxide thin film epitaxy, perovskite oxides have found use in optical waveguides [22–25], diffraction gratings [26], beam deflectors [27], sensors [28, 29], optical storage [30], frequency doublers [31], electroluminescence devices [32], pyroelectric infrared detectors [33, 34], and various electro-optic components [35, 36].

By force of their large electro-optic coefficient, ferroelectric crystals are recognized as an important class of materials for device applications. The electro-optic effect is commonly used for beam steering and shaping, dynamic focusing, switching, and optical modulation. $LiNbO_3$ has long been the material of choice for such applications. Numerous electro-optic modulators and waveguide components have been fabricated in $LiNbO_3$ [37–39]. Other ferroelectrics with a strong electro-optic response include $BaTiO_3$, $KNbO_3$, $K(Ta,Nb)O_3$, $LiTaO_3$, $(Sr,Ba)Nb_2O_6$, and $(Pb,La)(Zr,Ti)O_3$ (PLZT).

The development of optically transparent PLZT ceramics [40], with electro-optic properties that can be controlled by adjusting the cation composition, renders this materials system highly attractive for optical applications [41, 42]. Ceramic PLZT was first applied in optical shutter technology [43–46]. In the 1970's, optical components based on this principle were commercialized, including eye protective devices (flash goggles) and linear gate arrays for optical encoding [47–49]. Moreover, PLZT ceramics were studied extensively in efforts to develop page composers and image storage devices [50, 51]. Land *et al.* [52] demonstrated that optical images could be stored (nonvolatile) in PLZT ceramics. The stored data could be erased and rewritten using a combination of light and an applied bias voltage. Lenses with variable focal length and dual focal points were demonstrated in the 1990's using PLZT with transparent electrodes [53–55]. A high diffraction efficiency electro-optic phase grating fabricated on a PLZT ceramic wafer was reported by Song *et al.* [56]. PLZT ceramics were also introduced in applications such as displays and optical modulators [57–62].

The successful fabrication of optically transparent, crystalline PLZT thin films with strong electro-optic effects [63–66] lead to the development of thin film devices with substantial potential for applications in integrated optics. Kawaguchi *et al.* [67] reported thin-film ridge-type waveguides formed in PLZT, for which the electro-optic response was investigated by fabrication of a Mach-Zehnder type interferometer. The experiments showed that the magnitude of the quadratic electro-optic effect was several times larger than that of conventional Ti-diffused $LiNbO_3$ waveguides. Jin *et al.* [68] constructed a Mach-Zehnder type electro-optic modulator from reversed-ridge PLZT thin film waveguides. For $\lambda_0 = 1.55$ µm, the propagation losses of the reversed-ridge waveguides were measured at 2.7 dB/cm. The extinction ratio and the half-wave modulation voltage for the Mach-Zehnder modulator were reported at 14.4 dB and $V_\pi = 8.5$ V, respectively. Wang *et al.* [69] demonstrated PLZT thin film interferometers with fast switching and low driving voltage, characteristics beneficial to spatial light modulators. In a recent work, Fujii *et al.* [70] reported a 180 × 180 pixel electro-optic spatial light modulator with 7 ns switching speed fabricated in thin-film PLZT. Optical waveguide switches based on the electro-optic effect are promising devices for the realization of high-speed multiplexers in optical communication networks. A four-port channel waveguide switch with 3 dB modulation depth, GHz switching speed, and switching voltages less than 5 V was demonstrated in PLZT thin films [71]. Glebov *et al.* reported electro-optic planar deflector switches with thin film PLZT active elements [72, 73].

The developments referred to above have motivated the research discussed in this thesis on the PLZT materials system. The work is focussed on epitaxial growth of ferroelectric PLZT thin films for electro-optic device applications.

1.1.1 Ferroelectricity and the electro-optic effect

The origin of ferroelectricity derives from the crystalline structure of the material. Only non-centrosymmetric crystals, i.e., crystals without an inversion center, possess polar properties. All of the 21 non-centrosymmetric point groups (except for point group 432) exhibit the piezoelectric effect. Ten out of these possess a unique polar axis and exhibit the pyroelectric effect. In such crystals the spontaneous polarization vector has two or more equilibrium orientations. Pyroelectric crystals in which the spontaneous polarization can be switched between these equilibrium orientations by application of an external electric field are classified as ferroelectric [4, 74].

Ferroelectric oxides with the perovskite structure possess a unique polar axis and have the stoichiometric formula ABO_3. Common examples of such materials include $BaTiO_3$, $BiFeO_3$, $PbTiO_3$, and $SrTiO_3$. Figure 1.1(a) shows a schematic of the ABO_3 unit cell in the paraelectric cubic phase. The A-cations sit at the corners of the unit cell, and the B-cation is located in the center. The oxygen anions (O) are octahedrally coordinated with respect to the smaller B-cation. In general, ferroelectric materials undergo a structural phase transition from a high temperature paraelectric phase to a low temperature ferroelectric phase of lower symmetry. For a perovskite oxide, the transition from the cubic paraelectric phase to the tetragonal ferroelectric phase is associated with a displacement of the B-cation along the unit cell c-axis, as depicted in Figures 1.1(b)

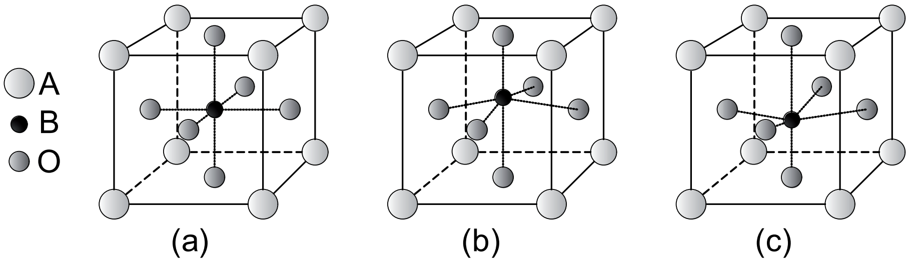

Figure 1.1: Schematic of the unit cell of the ABO_3 perovskite oxide in (a) the paraelectric phase, (b) the ferroelectric phase with the B-cation displaced upwards, and (c) the ferroelectric phase with the B-cation displaced downwards.

and (c). The displacement of the B-cation relative to the centrosymmetric position results in a net charge displacement, i.e., an electric dipole moment [74].

The direction of this charge displacement, or dipole moment, depends on the mechanical and electrical boundary conditions imposed on the ferroelectric crystal. A region of uniform spontaneous polarization is referred to as a ferroelectric domain. Domains of opposite directions are formed during the ferroelectric phase transition in order to minimize the electrostatic energy of the depolarizing field, as well as the elastic energy associated with mechanical constraints. The reversal of the spontaneous polarization by an applied electric field is referred to as *polarization switching* and results in a characteristic hysteresis behavior for polarization vs. electric field, also known as a P–E loop. Figure 1.2 shows a typical P–E loop for a crystal with an ideal ferroelectric response. The polarization at zero applied field ($E = 0$) is referred to as the remanent polarization, P_r, whereas the minimum electric field required to switch the polarization direction ($P = 0$) is referred to as the coercive field, E_c.

The electro-optic response of perovskite oxides has important implications for devices, as it permits modification of the phase velocity of electromagnetic waves in the material by application of an external electric field. In general, the propagation of electromagnetic waves in a dielectric crystal can be described in terms of the

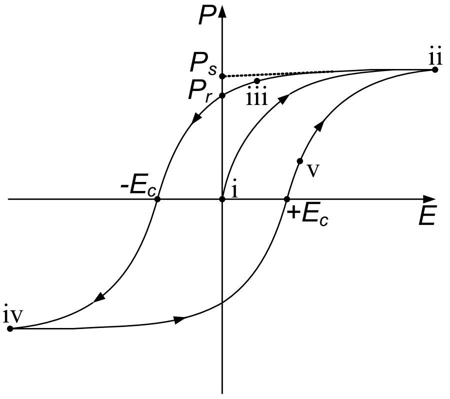

Figure 1.2: Polarization (P) versus electric field (E) hysteresis curve for a ferroelectric crystal. P_s, P_r, and E_c denote the saturation polarization, remanent polarization, and coercive field, respectively. Upon initial poling of a ferroelectric crystal and subsequent polarization reversals, the trace of P vs. E follows the hysteresis loop from i to v.

impermeability tensor $\eta = \varepsilon_0 \boldsymbol{\epsilon}^{-1}$. The elements η_{ij} of this tensor are altered when an electric field $\vec{E} = (E_1, E_2, E_3)$ is applied to the crystal, i.e., η_{ij} becomes a function of $\vec{E}$. $\eta_{ij}(\vec{E})$ may be expanded in a Taylor's series about $\vec{E} = 0$,

$$\eta_{ij}(\vec{E}) = \eta_{ij}(0) + \sum_k \mathfrak{r}_{ijk} E_k + \sum_{kl} \mathfrak{s}_{ijkl} E_k E_l, \quad i,j,k,l = 1,2,3, \quad (1.1)$$

where $\mathfrak{r}_{ijk}$ and $\mathfrak{s}_{ijkl}$ are the linear (Pockels) and the quadratic (Kerr) electro-optic coefficients, respectively [75].

The Pockels coefficients $\mathfrak{r}_{ijk}$ form a tensor of third rank. A contracted notation of the index tensor is frequently adopted, i.e., i and j combine to a single index I, according to a given set of rules.[1] The Pockels coefficients of ferroelectric crystals are typically an order of magnitude higher than those of nonferroelectric materials, which makes such oxides a favored class of materials for electro-optic devices [40, 76–79]. Moreover, the electro-optic coefficients show a distinct anisotropy, which derives from the presence of a polar axis.

---

[1] $ij \to I:\ 11 \to 1,\ 22 \to 2,\ 33 \to 3,\ (23,32) \to 4,\ (13,31) \to 5,\ (12,21) \to 6.$

An external electric field applied along the c-axis of the crystal gives rise to a change in the extraordinary ($n_e = n_3$) and the ordinary ($n_o = n_1 = n_2$) refractive indices [75],

$$\Delta n_e = -\left(\frac{1}{2}\right) n_e^3 \mathfrak{r}_{33} E_3 \quad \text{and} \quad \Delta n_o = -\left(\frac{1}{2}\right) n_o^3 \mathfrak{r}_{13} E_3. \tag{1.2}$$

In absolute terms, the magnitude of the Pockels effect is quite small. Changes in the refractive index are typically less than 10^{-4}, and thus, a propagation distance on the order of several thousand wavelengths ($\sim$1 mm) is normally required in order to obtain a phase change of π radians. In practical terms, this implies that an electro-optic device requires large dimensions compared to the typical integrated electronic circuit.

1.2 Photonic crystals

Photonic crystals constitute a novel class of engineered metamaterials, with ample potential for photonic device applications. Since their inception in the late 1980's [80, 81], such periodic dielectric structures have developed into a rapidly growing field of research, mainly due to their vast potential for device miniaturization and light manipulation [82]. The underlying physical concept of a photonic crystal can be understood by reviewing the fundamental properties of electromagnetic waves.[2] The photonic crystal prohibits propagation of electromagnetic radiation of certain wavelengths due to periodic scattering. This makes their transmission characteristics the electromagnetic analogue of the electronic band structure of a crystalline solid, with bands of permitted propagating electromagnetic states separated by forbidden energy gaps, commonly referred to as photonic band gaps [83].

The capability of photonic crystals to guide and direct light on the scale of the optical wavelength by means of coherent localization of photons, is an important step towards realization of all optical,

---

[2] Electromagnetic wave propagation in periodic dielectric media is briefly described in Appendix A

low-loss circuitry for optical telecommunications and high speed optical computers [84–86]. The photonic band gap makes it possible to construct high-Q cavities for effective radiation sources with zero or low pumping threshold [87, 88], negative refractive index metamaterials [89] and nano-optical microlenses with ultrashort focal length [90], as well as micromechanically tunable optical sensors and filters with a wide range of transmission and reflection coefficients [91]. Moreover, advanced sensing, enhanced nonlinear effects, and reduced radiation losses in optical fibers can be realized by incorporating photonic crystals [92].

Photonic crystals are categorized according to the number of dimensions in which the dielectric function is periodic. Figure 1.3 illustrates periodic dielectric structures in one, two, and three dimensions. An omnidirectional photonic band gap, i.e., a band gap exists for propagation of light in all directions, is only possible for three-dimensional (3D) periodic crystals.

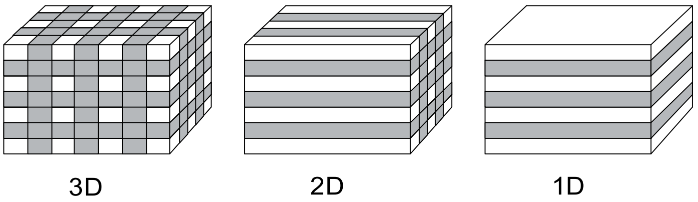

Figure 1.3: Illustration of periodic dielectric structures in one, two, and three dimensions. Gray color indicate regions of high dielectric constant.

Experimental realization of such 3D periodic structures is a challenge. However, several promising designs and fabrication strategies have been proposed [93–96]. The strict requirements placed on alignment and the complex connectivity of 3D photonic crystals make low-dimensional periodic structures highly attractive, due to their ease of fabrication. For example, two-dimensional (2D) periodic structures are utilized in photonic crystal fibers in order to confine light in the fiber core and diminish the impact of certain materials phenomena, such as dispersion and non-linear optical effects [97]. One-dimensional (1D) photonic crystals are commonly utilized in multilayered thin film stacks, acting as compact optical isolators (Bragg reflectors) [98] and stop band filters [99, 100].

Photonic crystal slabs, also known as planar or thin film photonic crystals, are periodic dielectric structures with periodicity in two dimensions. In the third dimension, i.e., the direction perpendicular to the plane of the slab, light is confined by index guiding. Such quasi-2D periodic structures are readily fabricated in dielectric thin films using standard processing techniques. For this reason, a considerable amount of research has lately been devoted to photonic crystal slabs [101–104].

1.3 Scope and thesis outline

The key challenge of this work has been to establish experimental routes to the synthesis of epitaxial thin films of optically transparent PLZT, intended for applications in integrated photonics and electro-optic devices. A central issue in this endeavor is to combine such thin films epitaxially with silicon, the industrially predominant semiconductor material. This should greatly enhance the feasibility of manufacturing integrated devices with ferroelectric oxides. Fabrication of such devices from monocrystalline thin film epilayers provides for control and utilization of physical properties which depend on crystalline direction, such as the linear electro-optic effect.

The final part of the thesis is focussed on the design and fabrication of photonic crystal slabs and line-defect waveguides, as well as a ridge-type Mach-Zehnder interferometer, in optically transparent, epitaxial PLZT thin films. Figure 1.4 depicts a line-defect waveguide, formed in a photonic crystals slab by a perturbation of the 2D periodicity of the crystal lattice. Compared to conventional thin-film optical waveguides based on index guiding, line-defect waveguides have the advantage of low radiation losses and the possibility to bend and manipulate light on a length scale comparable to the optical wavelength [105–107], characteristics important to implementation of optical circuitry and integrated photonic chips. Besides the potential for device miniaturization with such waveguides, the strong electro-optic response of PLZT may serve to change the transmission properties of the photonic crystal, by applying an external electric field to modulate the refractive index of the material [108–111].

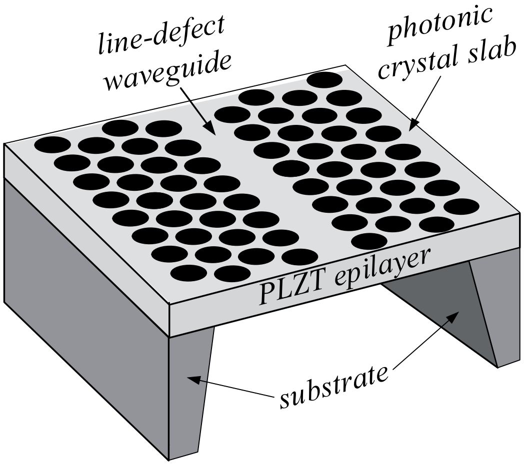

Figure 1.4: Line-defect waveguide in a photonic crystal slab formed by removing a row of holes from the 2D crystal lattice. The underlying substrate is removed to form an air-suspended membrane. The slab thickness and the diameter of the air holes are typically one third of the optical wavelength.

The outline of this thesis is arranged as follows. The materials system investigated is introduced in Chapter 2, while experimental techniques for thin film growth, materials characterization, and device fabrication are addressed in Chapter 3. Thin film waveguides, photonic crystal slabs, and line-defect waveguides are briefly reviewed in Chapter 4, highlighting those properties important to device applications. The synthesis of PLZT thin film epilayers on various substrates is reported in detail in Chapters 5–7. The results of numerical simulations of photonic crystal slabs and line-defect waveguides are discussed in Chapter 8. The design and fabrication of an electro-optic modulator as well as the processing of photonic crystal slabs by focused ion beam etching are described in Chapter 9. Chapter 10 holds the main conclusions and an outlook for further work.

References

[1] "International Technology Roadmap for Semiconductors (ITRS): Process Integration, Devices, and Structures," 2007.

[2] Vlasov, Y. A., O'Boyle, M., Hamann, H., and McNab, S. J., "Active control of slow light on a chip with photonic crystal waveguides," *Nature*, vol. 438, pp. 65–69, 2005.

[3] Vlasov, Y., Green, W. M. J., and Xia, F., "High-throughput silicon nanophotonic wavelength-insensitive switch for on-chip optical networks," *Nat. Photonics*, vol. 2, pp. 242–246, 2008.

[4] Lines, M. E., and Glass, A. M., *Principles and applications of ferroelectric and related materials.* Oxford, UK: Clarendon Press, 1988.

[5] Scott, J. F., and Araujo, C. A., "Ferroelectric memories," *Science*, vol. 246, pp. 1400–1405, 1989.

[6] Auciello, O., Scott, J. F., and Ramesh, R., "The physics of ferroelectric memories," *Phys. Today*, vol. 50, pp. 22–27, 1998.

[7] Ramesh, R., Aggarwal, S., and Auciello, O., "Science and technology of ferroelectric films and heterostructures for non-volatile ferroelectric memories," *Mater. Sci. Eng.*, vol. 32, pp. 191–236, 2001.

[8] Béa, H., Gajek, M., Bibes, M., and Barthélémy, A., "Spintronics with multiferroics," *J. Phys.: Condens. Matter*, vol. 20, p. 434221, 2008.

[9] Bibes, M., and Barthélémy, A., "Multiferroics: Towards a magnetoelectric memory," *Nat. Mater.*, vol. 7, pp. 425–426, 2008.

[10] Hirai, T., Nagashima, K., Koike, H., Matsuno, S., and Tarui, Y., "Crystal and electrical characterizations of epitaxial $Ce_xZr_{1-x}O_2$ buffer layer for the

metal/ferroelectric/insulator/semiconductor field effect transistor," *Jpn. J. Appl. Phys.*, vol. 35, pp. 5150–5153, 1996.

[11] Mathews, S., Ramesh, R., Venkatesan, T., and Benedetto, J., "Ferroelectric field effect transistor based on epitaxial perovskite heterostructures," *Science*, vol. 276, pp. 238–240, 1997.

[12] Dawber, M., Rabe, K. M., and Scott, J. F., "Physics of thin-film ferroelectric oxides," *Rev. Mod. Phys.*, vol. 77, pp. 1083–1130, 2005.

[13] Muralt, P., "Ferroelectric thin films for micro-sensors and actuators: a review," *J. Micromech. Microeng.*, vol. 10, pp. 136–146, 2000.

[14] Ren, T.-L., Zhao, H.-J., Liu, L.-T., and Li, Z.-J., "Piezoelectric and ferroelectric films for microelectronic applications," *Mater. Sci. Eng. B*, vol. 99, pp. 159–163, 2003.

[15] Srinivasan, S., Hiller, J., Kabius, B., and Auciello, O., "Piezoelectric/ultrananocrystalline diamond heterostructures for high-performance multifunctional micro/nanoelectromechanical systems," *Appl. Phys. Lett.*, vol. 90, p. 134101, 2007.

[16] Adachi, H., Mitsuyu, T., and Wasa, K., "SAW properties of PLZT epitaxial thin films," *Jpn. J. Appl. Phys.*, vol. 24, pp. 121–123, 1985.

[17] Shih, W.-C., and Wu, M.-S., "Propagation characteristics of surface acoustic waves in perovskite-type ferroelectric films/MgO/GaAs structure," *J. Phys. D: Appl. Phys.*, vol. 30, pp. 151–160, 1997.

[18] Du, H., Johnson, D. W., Zhu, W., Graebner, J. E., Kammlott, G. W., Jin, S., Rogers, J., Willett, R., and Fleming, R. M., "Growth and measurements of ferroelectric lead zirconate titanate on diamond by pulsed laser deposition," *J. Appl. Phys.*, vol. 86, p. 2220, 1999.

[19] Kumar, A. K. S., Paruch, P., Triscone, J.-M., Daniau, W., Ballandras, S., Pellegrino, L., Marré, D., and Tybell, T., "High-frequency surface acoustic wave device based on thin-film piezoelectric interdigital transducers," *Appl. Phys. Lett.*, vol. 85, pp. 1757–1759, 2004.

[20] Ichiki, M., Morikawa, Y., and Nakada, T., "Electrical properties of ferroelectric lead lanthanum zirconate titanate as an energy transducer for application to electrostatic-optical motor," *Jpn. J. Appl. Phys.*, vol. 41, pp. 6993–6996, 2002.

[21] Machura, D., Rymarczyk, J., and Ilczuk, J., "Ceramic bismuth titanate for high-temperature electro-acoustic transducers," *Eur. Phys. J. Special Topics*, vol. 154, pp. 131–134, 2008.

[22] Baude, P. F., Ye, C., Tamagawa, T., and Polla, D. L., "Fabrication of sol-gel derived ferroelectric $Pb_{0.865}La_{0.09}Zr_{0.65}Ti_{0.35}O_3$ optical waveguides," *J. Appl. Phys.*, vol. 73, pp. 7960–7962, 1993.

[23] Nashimoto, K., Nakamura, S., Morikawa, T., Moriyama, H., Watanabe, M., and Osakabe, E., "Fabrication of electro-optic $Pb(Zr,Ti)O_3$ heterostructure waveguides on Nb-doped $SrTiO_3$ by solid-phase epitaxy," *Appl. Phys. Lett.*, vol. 74, pp. 2761–2763, 1999.

[24] Escoubas, L., Huguet-Chantome, P., Jelinek, M., Flory, F., Drouard, E., Lancok, J., Simon, J. J., and Mazingue, T., "Optical and electro-optical properties of pulse laser deposited PLZT thin films," *Opt. Eng.*, vol. 42, pp. 3579–3584, 2003.

[25] Wang, D. Y., Lor, K. P., Chung, K. K., Chan, H. P., Chiang, K. S., Chan, H. L. W., and Choy, C. L., "Optical rib waveguide based on epitaxial $Ba_{0.7}Sr_{0.3}TiO_3$ thin film grown on MgO," *Thin Solid Films*, vol. 510, pp. 329–333, 2006.

[26] Yasumoto, M., Suzuki, T., Tsuda, H., Raj, M., Kudzuma, D., Dawley, J., Ritums, D., Tanaka, Y., and

Nashimoto, K., "Fabrication of (Pb,La)(Zr,Ti)O_3 thin-film arrayed waveguide grating," *Electron. Lett.*, vol. 43, pp. 24–25, 2007.

[27] Nashimoto, K., Nakamura, S., Moriyama, H., Watanabe, M., and Osakabe, E., "Electro-optic beam deflector using epitaxial Pb(Zr,Ti)O_3 waveguides on Nb-doped $SrTiO_3$," *Appl. Phys. Lett.*, vol. 73, pp. 303–305, 1998.

[28] Raviprakash, J., Trolier-McKinstry, S., Cheng, J.-G., McNeal, M., Greenwald, A., Puscasu, I., Johnson, E., Pralle, M., and Shah, A., "Ferroelectric PTCR films for photonic crystal gas sensor," *Mater. Res. Soc. Symp. Proc.*, vol. 952, 2007.

[29] Tang, X., Remmel, K., Lan, X., Deng, J., Xiao, H., and Dong, J., "Perovskite-type oxide thin film integrated fiber optic sensor for high-temperature hydrogen measurement," *Anal. Chem.*, vol. 81, pp. 7844–7848, 2009.

[30] Dimos, D., Warren, W. L., Sinclair, M. B., Tuttle, B. A., and Schwartz, R. W., "Photoinduced hysteresis changes and optical storage in (Pb,La)(Zr,Ti)O_3, thin films and ceramics," *J. Appl. Phys.*, vol. 76, pp. 4305–4315, 1994.

[31] Hewig, G. H., and Jain, K., "Frequency doubling in a $LiNbO_3$ thin film deposited on sapphire," *J. Appl. Phys.*, vol. 54, pp. 57–61, 1983.

[32] Takashima, H., Shimada, K., Miura, N., Katsumata, T., Inaguma, Y., Ueda, K., and Itoh, M., "Low-driving-voltage electroluminescence in perovskite films," *Adv. Mater.*, vol. 21, pp. 3699–3702, 2009.

[33] Chang, C. C., and Tang, C. S., "An integrated pyroelectric infrared sensor with a PZT thin film," *Sensors and Actuators A: Phys.*, vol. 65, pp. 171–174, 1998.

[34] Guggilla, P., Batra, A. K., Currie, J. R., Aggarwal, M. D., Alim, M. A., and Lal, R. B., “Pyroelectric ceramics for infrared detection applications,” *Mater. Lett.*, vol. 60, pp. 1937–1942, 2006.

[35] Gill, D. M., Conrad, C. W., Ford, G., Wessels, B. W., and Ho, S. T., “Thin film channel waveguide electro-optic modulator in epitaxial $BaTiO_3$,” *Appl. Phys. Lett.*, vol. 71, pp. 1783–1785, 1997.

[36] Petraru, A., Schubert, J., Schmid, M., and Buchal, C., “Ferroelectric $BaTiO_3$ thin-film optical waveguide modulators,” *Appl. Phys. Lett.*, vol. 81, pp. 1375–1377, 2002.

[37] Thylen, L., “Integrated optics in $LiNbO_3$: recent developments in devices for telecommunications,” *J. Lightwave Technol.*, vol. 6, pp. 847–861, 1988.

[38] Abouelleil, M. M., and Leonberger, F. J., “Waveguides in lithium niobate,” *J. Am. Ceram. Soc.*, vol. 72, pp. 1311–1321, 1988.

[39] Lee, S.-H., Noh, T. W., and Lee, J.-H., “Control of epitaxial growth of pulsed laser deposited $LiNbO_3$ films and their electro-optic effects,” *Appl. Phys. Lett.*, vol. 68, pp. 472–474, 1996.

[40] Haertling, G. H., and Land, C. E., “Hot pressed $(Pb,La)(Zr,Ti)O_3$ ferroelectric ceramics for electrooptic applications,” *J. Am. Ceram. Soc.*, vol. 54, pp. 1–11, 1971.

[41] Mukherjee, A., Brueck, S. R. J., and Wu, A. Y., “Electro-optic effects in thin-film lanthanum-doped lead zirconate titanate,” *Opt. Lett.*, vol. 15, pp. 151–153, 1990.

[42] Nakada, M., Ohashi, K., and Akedo, J., “Optical and electro-optical properties of $Pb(Zr,Ti)O_3$ and $(Pb,La)(Zr,Ti)O_3$ films prepared by aerosol deposition method,” *J. Cryst. Growth*, vol. 275, pp. 1275–1280, 2005.

[43] Landry, M. J., and McCarthy, A. E., "Transmission switching characteristics of PLZT shutters," *Appl. Opt.*, vol. 12, pp. 2312–2319, 1973.

[44] Seino, T., and Watanabe, M., "Development and application of optical shutter made of PLZT ceramics," *Electronics and Communications in Japan Part II: Electronics*, vol. 77, pp. 77–87, 1994.

[45] Tanaka, K., Yamaguchi, M., Seto, H., Murata, M., and Wakino, K., "Analyses of PLZT electrooptic shutter and shutter array," *Jpn. J. Appl. Phys.*, vol. 24, pp. 177–182, 1985.

[46] Taniguchi, Y., Murakami, K., Kobayashi, H., and Tanaka, S., "A (Pb,La)(Zr,Ti)O_3 (PLZT) polarization-plane rotator with a buried electrode structure for a mid-infrared electro-optical shutter," *Jpn. J. Appl. Phys.*, vol. 36, pp. 2709–2714, 1997.

[47] Haertling, G. H., "PLZT electrooptic materials and applications – a review," *Ferroelectrics*, vol. 75, pp. 25–55, 1987.

[48] Cutchen, J. T., Harris, J. O., and Laguna, G. R., "PLZT electro-optic shutters: Applications," *Appl. Opt.*, vol. 14, pp. 1866–1873, 1975.

[49] Kirkby, C. J., "Electro-optic switching response in cubic phase PLZT ceramic materials," *Appl. Opt.*, vol. 15, pp. 828–830, 1976.

[50] Land, C. E., "Optical information storage and spatial light modulation in PLZT ceramics," *Appl. Eng.*, vol. 17, pp. 317–326, 1978.

[51] Roberts, P., "Strain-biased PLZT input devices (page composers) for holographic memories and optical data processing," *Appl. Opt.*, vol. 11, pp. 397–404, 1972.

[52] Land, C. E., and Smith, W. D., "Reflective-mode ferroelectric-photoconductor image storage and display devices," *Appl. Phys. Lett.*, vol. 23, pp. 57–59, 1973.

[53] Tatebayashi, T., Yamamoto, T., and Sato, H., "Electro-optic variable focal-length lens using PLZT ceramic," *Appl. Opt.*, vol. 30, pp. 5049–5055, 1991.

[54] Shibaguchi, T., and Funato, H., "Lead-lanthanum zirconate-titanate (PLZT) electrooptic variable focal-length lens with stripe electrodes," *Jpn. J. Appl. Phys.*, vol. 31, pp. 3196–3200, 1992.

[55] Castro, F., and Nabet, B., "Design of a dual-effect lens on lanthanum-modified lead zirconate titanate for continuous variation of focal length," *Appl. Opt.*, vol. 34, pp. 2317–2323, 1995.

[56] Song, Q. W., Talbot, P. J., and Maurice, J. H., "PLZT based high-efficiency electro-optic grating for optical switching," *J. Mod. Opt.*, vol. 41, pp. 717–727, 1994.

[57] Thapliya, R., Okano, Y., and Nakamura, S., "Electrooptic characteristics of thin-film PLZT waveguide using ridge-type Mach-Zehnder modulator," *J. Lightwave Technol.*, vol. 21, pp. 1820–1827, 2003.

[58] Rouchon, J. M., and Micheron, F., "Electrooptical properties and photoinduced effects in PLZT ceramics applications to optical storage and processing of information," *Czech. J. Phys. B*, vol. 25, pp. 575–584, 1975.

[59] Goldstein, D. H., "PLZT modulator characterization," *Opt. Eng.*, vol. 34, pp. 1589–1592, 1995.

[60] Sakuma, H., and Matsumura, M., "A new operating method for PLZT display devices," *Jpn. J. Appl. Phys.*, vol. 14, pp. 1845–1846, 1975.

[61] Young, D., Li, H., Choopun, S., Wang, L., Salamanca-Riba, L., Ramesh, R., and Christou, A., "Optical phase and amplitude modulation in (9/65/35) Pb-La-Zr-Ti-O thin films," *Mater. Res. Soc. Symp. Proc.*, vol. 541, pp. 753–758, 1999.

[62] Jin, M. S., Wang, J. H., Ozguz, V., and Lee, S. H., "Monolithic integration of a silicon driver circuit onto a lead lanthanum zirconate titanate substrate for smart spatial light modulator fabrication," *Appl. Opt.*, vol. 33, pp. 2842–2848, 1994.

[63] Nashimoto, K., Nakamura, S., Morikawa, T., Moriyama, H., Watanabe, M., and Osakabe, E., "Electrooptical properties of heterostructure (Pb,La)(Zr,Ti)O_3 waveguides on Nb-$SrTiO_3$," *Jpn. J. Appl. Phys.*, vol. 38, pp. 5641–5645, 1999.

[64] Adachi, H., Kawaguchi, T., Setsune, K., Ohji, K., and Wasa, K., "Electro-optic effects of (Pb,La)(Zr,Ti)O_3 thin films prepared by rf planar magnetron sputtering," *Appl. Phys. Lett.*, vol. 42, pp. 867–869, 1983.

[65] Uchiyama, K., Kasamatsu, A., Otani, Y., and Shiosaki, T., "Electro-optic properties of lanthanum-modified lead zirconate titanate thin films epitaxially grown by the advanced sol-gel method," *Jpn. J. Appl. Phys.*, vol. 46, pp. L244–L246, 2007.

[66] Shima, H., Iijima, T., Funaku, H., Nakajima, T., Naganuma, H., and Okamura, S., "Electrooptic and piezoelectric properties of (Pb,La)(Zr,Ti)O_3 films with various Zr/Ti ratios," *Jpn. J. Appl. Phys.*, vol. 47, pp. 7541–7544, 2008.

[67] Kawaguchi, T., Adachi, H., Setsune, K., Yamazaki, O., and Wasa, K., "PLZT thin-film waveguides," *Appl. Opt.*, vol. 23, pp. 2187–2191, 1984.

[68] Jin, G. H., Zou, Y. K., Fuflyigin, V., Liu, S. W., Lu, Y. L., Zhao, J., and Cronin-Golomb, M., "PLZT film waveguide Mach-Zehnder electrooptic modulator," *J. Lightwave Technol.*, vol. 18, pp. 807–812, 2000.

[69] Wang, F., Li, K. K., Fuflyigin, V., Jiang, H., Zhao, J., Norris, P., and Goldstein, D., "Thin ferroelectric interferometer for spatial light modulations," *Appl. Opt.*, vol. 37.

[70] Fujii, T., Suzuki, T., Fujimori, Y., Nakamura, T., Moriwake, M., and Takasu, H., "Development of (Pb,La)(Zr,Ti)O_3 electro-optic thin film for high-speed spatial light modulator," *Jpn. J. Appl. Phys.*, vol. 45, pp. 7520–7524, 2006.

[71] Wasa, K., Yamazaki, ., Adachi, H., Kawaguchi, T., and Setsune, K., "Optical TIR switches using PLZT thin-film waveguides on sapphire," *J. Lightwave Technol.*, vol. LT-2, pp. 710–714, 1984.

[72] Glebov, A. L., Lee, M. G., Lidu, H., Aoki, S., Yokouchi, K., Ishii, M., and Kato, M., "Electrooptic planar deflector switches with thin-film PLZT active elements," *IEEE J. Selected Topics in Quantum Electron.*, vol. 11, pp. 422–430, 2005.

[73] Glebov, A. L., Sugama, A., Smirnov, V. I., Aoki, S., Rotar, V., Lee, M. G., and Glebov, L. B., "Angle selective enhancement of beam deflection in high-speed electrooptic switches," *IEEE Photon. Technol. Lett.*, vol. 19, pp. 701–703, 2007.

[74] Damjanovic, D., "Ferroelectric, dielectric and piezoelectric properties of ferroelectric thin films and ceramics," *Rep. Prog. Phys*, vol. 61, pp. 1267–1324, 1998.

[75] Saleh, B. E. A., and Teich, M. C., *Fundamentals of Photonics.* Wiley-Interscience, 1991.

[76] Zgonik, M., Bernasconi, P., Duelli, M., Schlesser, R., Gunter, P., Garrett, M. H., Rytz, D., Zhu, Y., and Wu, X., "Dielectric, elastic, piezoelectric, electro-optic, and elasto-optic tensors of $BaTiO_3$ crystals," *Phys. Rev. B*, vol. 50, pp. 5941–5949, 1994.

[77] Zgonik, M., Schlesser, R., Biaggio, I., Voit, E., Tscherry, J., and Gunter, P., “Materials constants of $KNbO_3$ relevant for electro- and acousto-optics,” *J. Appl. Phys.*, vol. 74, pp. 1267–1297, 1993.

[78] Jazbinsek, M., and Zgonik, M., “Material tensor parameters of $LiNbO_3$ relevant for electro- and elasto-optics,” *Appl. Phys. B*, vol. 74, pp. 407–414, 2002.

[79] Lenzo, P. V., Spencer, E. G., and Ballman, A. A., “Electro-optic coefficients of ferroelectric strontium barium niobate,” *Appl. Phys. Lett.*, vol. 11, pp. 23–24, 1967.

[80] Yablonovitch, E., “Inhibited spontaneous emission in solid-state physics and electronics,” *Phys. Rev. Lett.*, vol. 58, pp. 2059–2062, 1987.

[81] John, S., “Strong localization of photons in certain disordered dielectric superlattices,” *Phys. Rev. Lett.*, vol. 58, pp. 2486–2489, 1987.

[82] Krauss, T. F., and Rue, R. M. D. L., “Photonic crystals in the optical regime – past, present and future,” *Prog. Quantum Electron.*, vol. 23, pp. 51–96, 1999.

[83] Ho, K. M., Chan, C. T., and Soukoulis, C. M., “Existence of a photonic band gap in periodic dielectric structures,” *Phys. Rev. Lett.*, vol. 65, pp. 3152–3155, 1990.

[84] Yablonovitch, E., Gmitter, T. J., Meade, R. D., Rappe, A. M., Brommer, K. D., and Joannopoulos, J. D., “Donor and acceptor modes in photonic band structure,” *Phys. Rev. Lett.*, vol. 67, pp. 3380–3383, 1991.

[85] Joannopoulos, J. D., Meade, R. D., and Winn, J. N., *Photonic Crystals - Molding the Flow of Light.* New Jersey, USA: Princeton University Press, 1995.

[86] Arsenault, A., Fournier-Bidoz, S., Hatton, B., Miguez, H., Tetreault, N., Vekris, E., Wong, S.,

Yang, S. M., Kitaev, V., and Ozin, G. A., "Towards the synthetic all-optical computer: science fiction or reality?," *J. Mater. Chem.*, vol. 14, pp. 781–794, 2004.

[87] Akahane, Y., Asano, T., Song, B.-S., and Noda, S., "High-Q photonic nanocavity in a two-dimensional photonic crystal," *Nature*, vol. 425, pp. 944–947, 2003.

[88] Nozaki, K., Nakagawa, A., Sano, D., and Baba, T., "Ultralow threshold and singlemode lasing in microgear lasers and its fusion with quasiperiodic photonic crystals," *IEEE J. Sel. Top. Quantum Electron.*, vol. 9, pp. 1355–1360, 2003.

[89] Menon, L., Lu, W. T., Friedman, A. L., Bennett, S. P., Heiman, D., and Sridhar, S., "Negative index metamaterials based on metal-dielectric nanocomposites for imaging applications," *Appl. Phys. Lett.*, vol. 93, pp. 123117–123119, 2008.

[90] Casse, B. D. F., Lu, W. T., Huang, Y. J., and Sridhar, S., "Nano-optical microlens with ultrashort focal length using negative refraction," *Appl. Phys. Lett.*, vol. 93, pp. 053111–053113, 2008.

[91] Suh, W., Yanik, M. F., Solgaard, O., and Fan, S., "Displacement-sensitive photonic crystal structures based on guided resonance in photonic crystal slabs," *Appl. Phys. Lett.*, vol. 82, pp. 1999–2001, 2003.

[92] Roberts, P., Couny, F., Sabert, H., Mangan, B., Williams, D., Farr, L., Mason, M., Tomlinson, A., Birks, T., Knight, J., and Russell, P. S. J., "Ultimate low loss of hollow-core photonic crystal fibres," *Opt. Express*, vol. 13, pp. 236–244, 2005.

[93] Qi, M., Lidorikis, E., Rakich, P. T., Johnson, S. G., Joannopoulos, J. D., Ippen, E. P., and Smith, H. I., "A three-dimensional optical photonic crystal with designed point defects," *Nature*, vol. 429, pp. 538–542, 2004.

[94] Blanco, A., Chomski, E., Grabtchak, S., Ibisate, M., John, S., Leonard, S. W., Lopez, C., Meseguer, F., Miguez, H., Mondia, J. P., Ozin, G. A., Toader, O., and van Driel, H. M., "Large-scale synthesis of a silicon photonic crystal with a complete three-dimensional bandgap near 1.5 micrometres," *Nature*, vol. 405, pp. 437–440, 2000.

[95] Vlasov, Y. A., Bo, X. Z., Sturm, J. C., and Norris, D. J., "On-chip natural assembly of silicon photonic bandgap crystals," *Nature*, vol. 414, pp. 289–293, 2001.

[96] Rinne, S. A., Garcia-Santamaria, F., and Braun, P. V., "Embedded cavities and waveguides in three-dimensional silicon photonic crystals," *Nature Photonics*, vol. 2, pp. 52–56, 2008.

[97] Chen, M., and Xie, S., "New nonlinear and dispersion flattened photonic crystal fiber with low confinement loss," *Opt. Comm.*, vol. 281, pp. 2073–2076, 2008.

[98] Beggs, D. M., Kaliteevski, M. A., and Abram, R. A., "Etched bragg reflectors as two-dimensional photonic crystals," *J. Phys.: Condens. Matter*, vol. 16, pp. 8093–8099, 2004.

[99] Kuo, M., Poxson, D. J., Kim, Y. S., Mont, F. W., Kim, J. K., Schubert, E. F., and Lin, S., "Realization of a near-perfect antireflection coating for silicon solar energy utilization," *Opt. Lett.*, vol. 33, pp. 2527–2529, 2008.

[100] Zhou, D., and Biswas, R., "Photonic crystal enhanced light-trapping in thin film solar cells," *J. Appl. Phys.*, vol. 103, p. 093102, 2008.

[101] Johnson, S. G., Fan, S., Villeneuve, P. R., Joannopoulos, J. D., and Kolodziejski, L. A., "Guided modes in photonic crystal slabs," *Phys. Rev. B*, vol. 60, pp. 5751–5758, 1999.

[102] Chow, E., Lin, S. Y., Johnson, S. G., Villeneuve, P. R., Joannopoulos, J. D., Wendt, J. R., Vawter,

G. A., Zubrzycki, W., Hou, H., and Alleman, A., “Three-dimensional control of light in a two-dimensional photonic crystal slab,” *Nature*, vol. 407, pp. 983–986, 2000.

[103] Krauss, T. F., “Planar photonic crystal waveguide devices for integrated optics,” *Phys. Stat. Sol.*, vol. 197, pp. 688–702, 2003.

[104] Loncar, M., Nedeljkovic, D., Doll, T., Vuckovic, J., Scherer, A., and Pearsall, T. P., “Waveguiding in planar photonic crystals,” *Appl. Phys. Lett.*, vol. 77, pp. 1937–1939, 2000.

[105] Johnson, S. G., Fan, S., Villeneuve, P. R., and Joannopoulos, J. D., “Linear waveguides in photonic-crystal slabs,” *Phys. Rev. B*, vol. 62, pp. 8212–8222, 2000.

[106] Prather, D. W., Shi, S., Pustai, D. M., Chen, C., Venkataraman, S., Sharkawy, A., Schneider, G. J., and Murakowski, J., “Dispersion-based optical routing in photonic crystals,” *Opt. Lett.*, vol. 29, pp. 50–52, 2004.

[107] Sharkawy, A., Pustai, D., Shi, S., Prather, D., McBride, S., and Zanzucchi, P., “Modulating dispersion properties of low index photonic crystal structures using microfluidics,” *Opt. Express*, vol. 13, pp. 2814–2827, 2005.

[108] Takeda, H., and Yoshino, K., “Tunable photonic bandgap in two-dimensional photonic crystals by temporal modulation based on the Pockels effect,” *Phys. Rev. E*, vol. 69, p. 016605, 2004.

[109] Li, B., Zhou, J., Li, L., Wang, X. J., Liu, X. H., and Zi, J., “Ferroelectric inverse opals with electrically tunable photonic band gap,” *Appl. Phys. Lett.*, vol. 83, pp. 4704–4706, 2003.

[110] Scrymgeour, D., Malkova, N., Kim, S., and Gopalan, V., “Electro-optic control of the superprism effect in photonic crystals,” *Appl. Phys. Lett.*, vol. 82, pp. 3176–3178, 2003.

[111] Xiong, S., and Fukshima, H., "Analysis of light propagation in index-tunable photonic crystals," *J. Appl. Phys.*, vol. 94, pp. 1286–1288, 2003.

Chapter 2

Materials system

High performance photonic devices call for materials with attractive optical properties, such as high transparency, high refractive index, high photostability, fast response, efficient fluorescence and electroluminescence, and strong second harmonic generation. The ferroelectric perovskite (Pb,La)(Zr,Ti)O_3 (PLZT) features a number of these properties, including low absorption at infrared frequencies [1–3], strong electro-optic and nonlinear effects with subnanosecond response [4–6], and high remanent polarization [7]. Thus, PLZT thin films may offer an attractive choice for electro-optic devices and integrated optics, in terms of low power dissipation, high-speed control, and device miniaturization.

2.1 (Pb,La)(Zr,Ti)O_3

The physical properties of La-substituted Pb(Zr,Ti)O_3 (PZT) ceramics were identified in the early 1970's at the Sandia Laboratories [7, 8]. Optical transparency of this ferroelectric oxide is achieved by substitution of lanthanum on the A (Pb) sites of the PZT perovskite unit cell, cf. Figure 1.1. The valence of this dopant (La^{3+}) exceeds that of the substituted Pb^{2+} ions. This type of substitution is referred to as soft doping, i.e., the optical anisotropy of the crystalline grains is reduced, which transforms the ceramic compound from opaque to transparent. The general formula for PLZT,

$$Pb_{1-x}La_x(Zr_yTi_{1-y})_{1-x/4}O_3,$$

presumes that charge neutrality is maintained through the formation of one B site vacancy (Zr,Ti) for every 4 at.% La [7].

The properties and applications of PLZT ceramics are to a large extent governed by the elemental composition [8, 9]. Figure 2.1 displays the room-temperature phase diagram for the PLZT system. Compositions from the $PbTiO_3$ rich end of the solution tend to favor a tetragonal distortion of the cubic unit cell. The composition of PLZT for the sputter target used in this work, PLZT 8/40/60 ($x = 0.08$, $y = 0.40$), crystallizes in the tetragonal ferroelectric phase and exhibits a linear electro-optic response (Pockels effect). PLZT with this composition renders hysteresis loops with a large coercive field E_c, high remanent polarization P_r, and a linear relation between the index change Δn and the applied electric field for $E < E_c$, without causing polarization reversal after initial poling of the crystal.

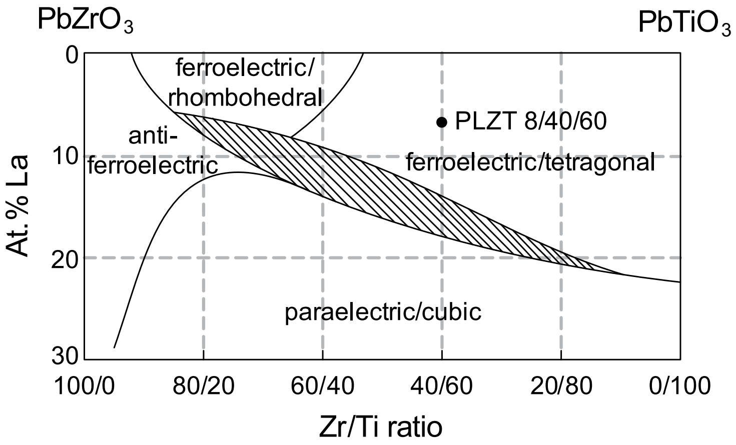

Figure 2.1: Phase diagram for (Pb,La)(Zr,Ti)O_3 at room temperature [7]. The hatched part of the diagram corresponds to a transition region between the ferro- and paraelectric phases, as well as the ferro- and antiferroelectric phases. The composition used in this study was $Pb_{0.92}La_{0.08}Zr_{0.4}Ti_{0.6}O_3$, or PLZT 8/40/60.

Such characteristics near $E = 0$ are useful for optical components operating without a biasing field.

PLZT 8/40/60 exhibits a high Curie temperature ($T_\mathrm{c} = 250°\mathrm{C}$), which implies a stable tetragonal phase for temperatures relevant to optical and electronic device applications. The a- and c-axis lattice parameters of bulk PLZT 8/40/60 are 4.029 Å and 4.074 Å, respectively, and the material density is 7.84 g/cm^3 [7]. PLZT 8/65/35 has been widely investigated due to its strong electro-optic response [4, 10–13]. This composition lies near the rhombohedral-tetragonal morphotropic phase boundary and exhibits a quadratic electro-optic response (Kerr effect). Lanthanum-rich compositions, e.g., PLZT 14/70/30, show ferroelectric characteristics such as narrow hysteresis loops and relaxor behavior [7], which implies that an applied electric field will force a transition from the paraelectric (cubic) to the ferroelectric (tetragonal or rhombohedral) phase at room temperature. Table 2.1 summarizes selected material parameters for different compositions of bulk PLZT ceramics.

Table 2.1: Selected materials parameters for different compositions of bulk (Pb,La)(Zr,Ti)O$_3$ [7]. κ, $\mathfrak{r}_c$, and T_c are the dielectric constant, the effective Pockels coefficient, and the Curie temperature, respectively.

Composition La/Zr/Ti	**Phase**$^{i)}$	κ	$\mathfrak{r}_\mathbf{c}{}^{ii)}$ pm/V	$T_\mathbf{c}$ °C	$P_\mathbf{r}$ µC/cm^2	$E_\mathbf{c}$ kV/cm
8/40/60	Tetragonal	982	102	250	28	20.7
8/65/35	Rhombohedral	3350	612	120	30	6.8
14/30/70	Tetragonal	1025	112	<100	25	15.4

$^{i)}$at room temperature, $^{ii)}\mathfrak{r}_c = (n_o/n_e)\mathfrak{r}_{33} - \mathfrak{r}_{13}$, where n_o and n_e denote the ordinary and the extraordinary refractive index, respectively.

The refractive index of PLZT thin films for the principal communication wavelength $\lambda_0 = 1.55$ µm is reported in the range 2.2–2.5 [2, 14]. Moreover, there is numerous reports on the electro-optic properties of PLZT thin films of different compositions. Nashimoto *et al.* [15] quote a linear electro-optic coefficient of ∼50 pm/V for PLZT 9/65/35 thin films grown by solid-phase epitaxy on Nb-doped SrTiO$_3$, which is approximately 10 % of the reported bulk value for

PLZT 9/65/35 ($\mathfrak{r}_c$ = 612 pm/V) [7]. Haertling [16] cites a Pockels coefficient of 53 pm/V for a 600 µm thick polycrystalline film of PLZT 8/65/35 prepared by dip coating. The electro-optic properties of PLZT 8/65/35 thin films fabricated by the sol-gel technique [17] were reported to exhibit a Pockels coefficient similar to that reported by Nashimoto [15]. A Pockels coefficient of 1000 pm/V was reported for bulk PLZT 8/65/35, prepared using a two-step annealing process [18]. These findings illustrate that the optical and electro-optic properties for PLZT ceramics are highly dependent on a number of factors, including the chemical composition, the material form (thin film vs. bulk), the crystalline structure, and the fabrication process. Table 2.2 summarizes the refractive indices and Pockels coefficients reported for other materials commonly used in electro-optic device applications [19–22].

Table 2.2: Physical properties for common electro-optic materials. The values pertain to bulk material.

Material	**Point group symmetry**	**Refractive index**	**Pockels coefficient pm/V**
$BaTiO_3$ [19]	4mm	$n_o = 2.412$	$\mathfrak{r}_{13} = 12$
		$n_e = 2.360$	$\mathfrak{r}_{33} = 110$
			$\mathfrak{r}_{51} = 1300$
$KNbO_3$ [20]	mm2	$n_a = 2.280$	$\mathfrak{r}_{13} = 34$
		$n_b = 2.330$	$\mathfrak{r}_{33} = 64$
		$n_c = 2.168$	$\mathfrak{r}_{32} = 450$
$LiNbO_3$ [21]	3m	$n_o = 2.286$	$\mathfrak{r}_{13} = 8$
		$n_e = 2.202$	$\mathfrak{r}_{33} = 31$
			$\mathfrak{r}_{51} = 28$
(Sr,Ba)Nb_2O_6 [22]	4mm	$n_o = 2.312$	$\mathfrak{r}_{13} = 67$
		$n_e = 2.273$	$\mathfrak{r}_{33} = 1340$

2.2 Substrate materials for thin film deposition

The growth of epitaxial oxide thin films is influenced by several factors, such as the growth parameters (substrate temperature, ambient pressure, growth rate, etc.) and the lattice structure and thermal expansion of the substrate. Controlling the crystalline orientation during thin film growth is vital for a number of reasons. For optical device applications, single-crystal growth is desirable in order to prevent light scattering at grain boundaries. Moreover, the physical properties of most complex oxides are anisotropic, and thus, epitaxial growth is favorable to fabrication of devices with a strong electro-optic response [23]. Other important criteria for introduction of PLZT in planar photonic devices include compatibility with established processing techniques and materials, as well as optical confinement, i.e., the light must be kept inside the PLZT layer by index guiding.

In recent years, epitaxial and textured PLZT thin films were grown on various oxide and semiconductor substrates, including fused silica [5, 24], quartz [14, 25, 26], sapphire [9, 27], glass [28–30], magnesium oxide [31–33], strontium titanate [3, 34–36], gallium arsenide [32], and silicon [10, 13, 37, 38]. In the present study, PLZT thin films were grown on $SrTiO_3(001)$, MgO(001), and Si(001) substrates. $SrTiO_3$ has a modest (3.1 %) lattice mismatch with PLZT. However, the use of $SrTiO_3$ for thin film waveguide devices is hampered by the relatively high refractive index of this substrate. MgO on the other hand has a low refractive index, a prerequisite for strong optical mode confinement in the PLZT active layer. Epitaxial growth is, however, complicated by the comparatively large (4.6 %) lattice mismatch between MgO and PLZT. Silicon is the predominant semiconductor material in integrated electronic circuits. Thus, integration of ferroelectric oxide thin films with silicon is of considerable interest [39–41]. Epitaxial growth of such oxides on silicon is challenging, however, due to the formation of an amorphous SiO_2 surface layer, which implies that the crystallinity of the substrate is discontinued. For this reason, the introduction of a buffer layer is generally required in order to achieve epitaxial growth [33].

2.2.1 Buffer layers for epitaxial growth on Si

There are a number of binary oxides that are thermodynamically stable in contact with silicon, such as CaO, MgO, SrO, HfO_2, ZrO_2, Al_2O_3, Gd_2O_3, Lu_2O_3, Sc_2O_3, Sm_2O_3, and Y_2O_3 [42]. Yttria-stabilized zirconia, $(Y_2O_3)_x(ZrO_2)_{1-x}$ or YSZ, is thermodynamically stable in contact with silicon [43] and is widely used as a buffer layer to facilitate epitaxial growth of complex oxides on silicon [44–48]. The lattice parameters of YSZ depend on the composition and increase with the amount of added yttria [49]. The phase is cubic for yttria contents in excess of 5 mol%, whereas a tetragonal phase prevails for an yttria content less than 5 mol% [50]. (001)-oriented YSZ thin films were previously reported to grow with a cube-on-cube epitaxial relationship with Si(001), even without stripping the silicon wafer of its native surface oxide prior to deposition [51–54], i.e., for a native oxide layer already present on the silicon substrate surface, zirconium reacts with SiO_2 to produce zirconia and SiO according to

$$\mathrm{Zr} + 2\mathrm{SiO_2} \rightarrow \mathrm{ZrO_2} + 2\mathrm{SiO}.$$

This reaction is irreversible and is followed by surface desorption of SiO [55].

A large lattice mismatch remains between YSZ-buffered silicon and PLZT, however, which complicates further epitaxial growth. For this reason, CeO_2 is commonly combined with YSZ to provide a multilayer buffer structure that facilitates epitaxy of perovskite oxides [56–58]. The perovskite unit cell is a close match with the in-plane diagonal of the CeO_2 unit cell ($a = b = c = 5.410$ Å). Moreover, CeO_2 serves as a barrier to oxygen diffusion, thus preventing thermal oxidation of silicon at the YSZ/Si interface during subsequent oxide thin film growth [59]. It was previously reported that growth of (001)-oriented CeO_2 thin films is not possible on a bare Si(001) substrate [58]. This is due to formation of amorphous SiO_2 and the presence of Ce_2O_3 on the substrate surface [53], i.e., CeO_2 is not thermodynamically stable in direct contact with silicon.

$SrTiO_3$-buffered silicon substrates have been extensively investigate in recent years. Growth of $SrTiO_3$ on Si(001) using molecular beam epitaxy shows that commensurate heteroepitaxy between $SrTiO_3$ and silicon is established via a controlled layer-by-layer deposition [60]. This implies that the crystalline interface is stabilized by the sequencing of five monolayers. In order to develop such heteroepitaxy, energy minimization consistent with layer-by-layer thermodynamic stability is required, which may be accomplished by introducing an alkaline earth silicide layer between the alkaline earth oxide plane of the perovskite and the silicon substrate. Thus, the role of Sr in enabling oxide heteroepitaxy between $SrTiO_3$ and silicon has received much attention. Theoretical studies suggest that for epitaxial oxide growth the optimal coverage of Sr on the Si surface is 1/2 monolayer [61]. The stability of $SrTiO_3$ films on Sr-covered silicon has been calculated from first principles [62, 63]. Experimental studies have shown that a Sr coverage between $\frac{1}{4}$ and $\frac{1}{2}$ monolayer is sufficient for epitaxial growth of $SrTiO_3$ on Si(001) [64].

2.3 Electrode layers for device applications

The ferroelectric perovskite $SrRuO_3$ has metallic properties and is widely used as an electrode layer in multilayered devices [48, 65–68]. The chemical stability and perovskite structure of $SrRuO_3$ allows for epitaxial integration with various ferroelectric oxides [33, 69, 70]. In order to ensure adequate conduction properties, the thickness of the $SrRuO_3$ electrode layer should be at least $\sim$20–30 nm [71]. The unit cell of $SrRuO_3$ has an orthorhombic structure, with lattice parameters $a = 5.53$ Å, $b = 5.57$ Å, and $c = 7.85$ Å. However, the $SrRuO_3$ unit cell is commonly described as a slightly distorted pseudocubic structure with lattice parameters $a = b = c = 3.93$ Å [72].

2.4 Overview of structural and optical properties

The structural and optical parameters of the PLZT 8/40/60 materials system and the substrates, buffer layers, and electrode layers discussed in this chapter are summarized in Table 2.3.

Table 2.3: Crystal structure, lattice parameters, lattice mismatch, and refractive index for PLZT 8/40/60, substrates, buffer layers, and electrode layer. The values pertain to bulk material.

Material	Crystal structure	a, b Å	c Å	Lattice mismatch$^{i)}$	$n^{ii)}$
PLZT 8/40/60	Perovskite	4.029	4.074	-	~2.4
$SrRuO_3^{iii)}$	Perovskite	3.930	3.930	2.5 %	~3.2$^{iv)}$
CeO_2	Fluorite	5.410	5.410	5.1 %	2.31$^{v)}$
YSZ (12 % Y_2O_3)	Fluorite	5.125	5.125	27.2 %	2.11
$SrTiO_3$(001)	Perovskite	3.905	3.905	3.1 %	2.30
MgO(001)	Rocksalt	4.216	4.216	4.6 %	1.71
Si(001)	Diamond	5.430	5.430	4.7 %	3.48

$^{i)}$For the in-plane lattice parameter with respect to that of PLZT 8/40/60 (for Si and CeO_2 the in-plane diagonal of the unit cell is assumed), $^{ii)}$for $\lambda = 1.55$ µm, $^{iii)}$assuming a pseudocubic unit cell, $^{iv)}$metallic properties [73], $^{v)}$for $\lambda = \infty$ [74].

References

[1] Nashimoto, K., Moriyama, H., Nakamura, S., Watanabe, M., Morikawa, T., Osakabe, E., and Haga, K., "PLZT electro-optic waveguides and switches," *Optical Fiber Communication Conference and Exhibit 2001, OFC 2001*, vol. 4, pp. PD10–1, 2001.

[2] Nashimoto, K., "PLZT thin film optical waveguide devices," *Proceedings of the 13th IEEE International Symposium on Applications of Ferroelectrics, ISAF 2002*, pp. 123–128, 2002.

[3] Kumar, A. K. S., Dahl, Ø., Pettersen, S. V., Grepstad, J. K., and Tybell, T., "Characterization of crystalline $Pb_{0.92}La_{0.08}Zr_{0.4}Ti_{0.6}O_3$ thin films grown by off-axis radio frequency magnetron sputtering," *Thin Solid Films*, vol. 492, pp. 71–74, 2005.

[4] Landry, M. J., and McCarthy, A. E., "Transmission switching characteristics of PLZT shutters," *Appl. Opt.*, vol. 12, pp. 2312–2319, 1973.

[5] Mukherjee, A., Brueck, S. R. J., and Wu, A. Y., "Electro-optic effects in thin-film lanthanum-doped lead zirconate titanate," *Opt. Lett.*, vol. 15, pp. 151–153, 1990.

[6] Bao, C., and Diels, J. C., "Ultrafast nonlinear response in PLZT thin films with ultrashort pulses," *Opt. Lett.*, vol. 20, pp. 2186–2188, 1995.

[7] Haertling, G. H., and Land, C. E., "Hot pressed (Pb,La)(Zr,Ti)O_3 ferroelectric ceramics for electrooptic applications," *J. Am. Ceram. Soc.*, vol. 54, pp. 1–11, 1971.

[8] Haertling, G. H., "Improved hot pressed electrooptic ceramics in the (Pb,La)(Zr,Ti)O_3 system," *J. Am. Ceram. Soc.*, vol. 54, pp. 303–309, 1970.

[9] Adachi, H., Mitsuyu, T., Yamazaki, O., and Wasa, K., "Ferroelectric (Pb,La)(Zr,Ti)O_3 epitaxial thin films on sapphire grown by rf-planar magnetron sputtering," *J. Appl. Phys.*, vol. 60, pp. 736–741, 1986.

[10] Dimos, D., Warren, W. L., Sinclair, M. B., Tuttle, B. A., and Schwartz, R. W., "Photoinduced hysteresis changes and optical storage in (Pb,La)(Zr,Ti)O_3, thin films and ceramics," *J. Appl. Phys.*, vol. 76, pp. 4305–4315, 1994.

[11] Levstik, A., Bobnar, V., Kutnjak, Z., and Kosec, M., "Fatigue and piezoelectric properties of lead lanthanum zirconate titanate ceramics," *J. Phys. D: Appl. Phys.*, vol. 31, pp. 2894–2897, 1998.

[12] Shah, S., and Rao, M. S. R., "Preparation and dielectric study of high-quality PLZT $x/65/35$ ($x = 6$, 7, 8) ferroelectric ceramics," *Appl. Phys. A*, vol. 71, pp. 65–69, 2000.

[13] Thomas, R., Mochizuki, S., Mihara, T., and Ishida, T., "PZT(65/35) and PLZT(8/65/35) thin films by sol-gel process: a comparative study on the structural, microstructural and electrical properties," *Thin Solid Films*, vol. 443, pp. 14–22, 2003.

[14] Escoubas, L., Huguet-Chantome, P., Jelinek, M., Flory, F., Drouard, E., Lancok, J., Simon, J. J., and Mazingue, T., "Optical and electro-optical properties of pulse laser deposited PLZT thin films," *Opt. Eng.*, vol. 42, pp. 3579–3584, 2003.

[15] Nashimoto, K., Nakamura, S., Morikawa, T., Moriyama, H., Watanabe, M., and Osakabe, E., "Electrooptical properties of heterostructure (Pb,La)(Zr,Ti)O_3 waveguides on Nb-SrTiO_3," *Jpn. J. Appl. Phys.*, vol. 38, pp. 5641–5645, 1999.

[16] Haertling, G. H., "Dielectric and electrooptic properties of acetate derived PLZT $X/65/35$ thin films," *Integr. Ferroelectr.*, vol. 3, pp. 207–215, 1993.

[17] Ishii, M., Satoh, K., Kato, M., and Kurihara, K., "Optical properties of epitaxial PLZT thin films fabricated by a sol-gel method," *Proceedings of the 14th International Symposium on Applications of Ferroelectrics, ISAF 2004*, pp. 77–80, 2004.

[18] Oshima, K., and Tsuzuki, K., "Electrooptic properties of two-stage sintered $(Pb_{1-x}La_x)(Zr,Ti)O_3$ $X/65/35$ ceramics (X = 6–9)," *Jpn. J. Appl. Phys.*, vol. 33, pp. 5389–5392, 1994.

[19] Zgonik, M., Bernasconi, P., Duelli, M., Schlesser, R., Gunter, P., Garrett, M. H., Rytz, D., Zhu, Y., and Wu, X., "Dielectric, elastic, piezoelectric, electro-optic, and elasto-optic tensors of $BaTiO_3$ crystals," *Phys. Rev. B*, vol. 50, pp. 5941–5949, 1994.

[20] Zgonik, M., Schlesser, R., Biaggio, I., Voit, E., Tscherry, J., and Gunter, P., "Materials constants of

$KNbO_3$ relevant for electro- and acousto-optics," *J. Appl. Phys.*, vol. 74, pp. 1267–1297, 1993.

[21] Jazbinsek, M., and Zgonik, M., "Material tensor parameters of $LiNbO_3$ relevant for electro- and elasto-optics," *Appl. Phys. B*, vol. 74, pp. 407–414, 2002.

[22] Lenzo, P. V., Spencer, E. G., and Ballman, A. A., "Electro-optic coefficients of ferroelectric strontium barium niobate," *Appl. Phys. Lett.*, vol. 11, pp. 23–24, 1967.

[23] Lee, S.-H., Noh, T. W., and Lee, J.-H., "Control of epitaxial growth of pulsed laser deposited $LiNbO_3$ films and their electro-optic effects," *Appl. Phys. Lett.*, vol. 68, pp. 472–474, 1996.

[24] Petersen, G. A., and McNeil, J. R., "Effects of oxygen partial pressure on lead content of PLZT thin films produced by excimer laser deposition," *Thin Solid Films*, vol. 220, pp. 87–91, 1992.

[25] Ramakrishnan, E. S., and Howng, W. Y., "Ferroelectric lead zirconate titanate thin films by radio frequency magnetron sputtering," *J. Vac. Sci. Technol. A*, vol. 10, pp. 69–74, 1992.

[26] Leng, W., Yang, C., Ji, H., Zhang, J., Tang, J., Chen, H., and Gao, L., "Linear and nonlinear optical properties of $(Pb,La)(Zr,Ti)O_3$ ferroelectric thin films grown by radio-frequency magnetron sputtering," *J. Phys. D: Appl. Phys.*, vol. 40, pp. 1206–1210, 2007.

[27] Jin, G. H., Zou, Y. K., Fuflyigin, V., Liu, S. W., Lu, Y. L., Zhao, J., and Cronin-Golomb, M., "PLZT film waveguide Mach-Zehnder electrooptic modulator," *J. Lightwave Technol.*, vol. 18, pp. 807–812, 2000.

[28] Preston, K. D., and Haertling, G. H., "Comparison of electro-optic lead-lanthanum zirconate titanate films on crystalline glass substrates," *Appl. Phys. Lett.*, vol. 60, pp. 2831–2833, 1992.

[29] Teowee, G., Boulton, J. M., and Uhlmann, D. R., "Optical and electro-optical properties of sol-gel derived ferroelectric thin films," *Integr. Ferroelectr.*, vol. 20, pp. 39–54, 1998.

[30] Nakada, M., Ohashi, K., and Akedo, J., "Optical and electro-optical properties of Pb(Zr,Ti)O_3 and (Pb,La)(Zr,Ti)O_3 films prepared by aerosol deposition method," *J. Cryst. Growth*, vol. 275, pp. 1275–1280, 2005.

[31] Yoon, D. S., Kim, C. J., Lee, J. S., Lee, W. J., and No, K., "Epitaxial growth of sol-gel PLZT thin films," *J. Mater. Res.*, vol. 9, pp. 420–425, 1994.

[32] Young, D., Li, H., Choopun, S., Wang, L., Salamanca-Riba, L., Ramesh, R., and Christou, A., "Optical phase and amplitude modulation in (9/65/35) Pb-La-Zr-Ti-O thin films," *Mater. Res. Soc. Symp. Proc.*, vol. 541, pp. 753–758, 1999.

[33] Kondo, M., Maruyama, K., and Kurihara, K., "Epitaxial ferroelectric thin films on silicon substrates for future electronic devices," *Fujitsu Sci. Tech. J.*, vol. 38, pp. 46–53, 2002.

[34] Higuma, Y., Tanaka, K., Nakagawa, T., Kariya, T., and Hamakawa, Y., "Epitaxial growth of PLZT single crystal film on $SrTiO_3$ by RF sputtering," *Jpn. J. Appl. Phys.*, vol. 16, pp. 1707–1708, 1977.

[35] Thapliya, R., Okano, Y., and Nakamura, S., "Electrooptic characteristics of thin-film PLZT waveguide using ridge-type Mach-Zehnder modulator," *J. Lightwave Technol.*, vol. 21, pp. 1820–1827, 2003.

[36] Kamehara, N., Ishii, M., Sato, K., Kurihara, K., and Kondo, M., "Optical properties of epitaxial PLZT thin films," *J. Electroceram.*, vol. 21, pp. 99–102, 2008.

[37] Hwang, Y. S., Paek, S. H., Lee, J. H., Park, C. S., Choi, J. S., Jung, J. K., and Kim, Y. N., "Formation and characteristics of lead lanthanum zirconium titanate thin films formed

by using the r.f. sputtering method," *J. Mater. Sci.*, vol. 7, pp. 309–313, 1996.

[38] Singh, R., Goel, T. C., and Chandra, S., "Effect of post-deposition annealing on phase formation and properties of RF magnetron sputtered PLZT thin films," *Mater. Res. Bull.*, vol. 43, pp. 384–393, 2008.

[39] Ramesh, R., Gilchrist, H., Sands, T., Keramidas, V. G., Haakenaasen, R., and Fork, D. K., "Ferroelectric La-Sr-Co-O/Pb-Zr-Ti-O/La-Sr-Co-O heterostructures on silicon via template growth," *Appl. Phys. Lett.*, vol. 63, pp. 3592–3594, 1993.

[40] Ghonge, S. G., Goo, E., Ramesh, R., Haakenaasen, R., and Fork, D. K., "Microstructure of epitaxial oxide thin film heterostructures on silicon by pulsed laser deposition," *Appl. Phys. Lett.*, vol. 64, pp. 3407–3409, 1994.

[41] Kondo, M., Sato, K., Ishii, M., Wakiya, N., Shinozaki, K., and Kurihara, K., "Electrooptic properties of lead zirconate titanate films prepared on silicon substrate," *Jpn. J. Appl. Phys.*, vol. 45, pp. 7516–7519, 2006.

[42] Schlom, D. G., Guha, S., and Datta, S., "Gate oxides beyond SiO_2," *Mater. Res. Bull.*, vol. 33, pp. 1017–1025, 2008.

[43] Samsonov, G. V., *The Oxide Handbook*. New York, USA: IFI/Plenum Data Company, 2nd ed., 1982.

[44] Fork, D. K., Fenner, D. B., Connell, G. A. N., Philips, J. M., and Geballe, T. H., "Epitaxial yttria-stabilized zirconia on hydrogen-terminated Si by pulsed laser deposition," *Appl. Phys. Lett.*, vol. 57, pp. 1137–1139, 1990.

[45] Fukumoto, H., Imura, T., and Osaka, Y., "Heteroepitaxial growth of yttria-stabilized zirconia (YSZ) on silicon," *Jpn. J. Appl. Phys.*, vol. 27, pp. L1404–L1405, 1988.

[46] Horita, S., Kawada, T., and Abe, Y., "Characterization of $Pb(Zr_xTi_{1-x})O_3$ thin film on silicon substrate with heteroepitaxial yttria-stabilized zirconia (YSZ) buffer layer," *Jpn. J. Appl. Phys.*, vol. 35, pp. L1357–L1359, 1996.

[47] Wang, S. J., Xu, S. Y., You, L. P., Lim, S. L., and Ong, C. K., "Microstructural studies on a high quality $YBa_2Cu_3O_{7-\delta}$/YSZ/Si multilayer prepared by pulsed-laser deposition," *Semicond. Sci. Technol.*, vol. 13, pp. 362–367, 2000.

[48] Hung, V. H., Minh, L. V., Huyen, B. T., and Minh, N. D., "Improvement of electrical property for $Pb(Zr_{0.53}Ti_{0.47})O_3$ ferroelectric thin film deposited by sol-gel method on SRO electrode," *Journal of Physics: Conference Series*, vol. 187, p. 012063, 2009.

[49] Stubican, V. S., Hink, R. C., and Ray, S. P., "Phase equilibria and ordering in the system ZrO_2-Y_2O_3," *J. Am. Ceram. Soc.*, vol. 61, pp. 17–21, 1978.

[50] Piascik, J. R., Thompson, J. Y., Bower, C. A., and Stoner, B. R., "Evaluation of crystallinity and film stress in yttria-stabilized zirconia thin films," *J. Vac. Sci. Technol. A*, vol. 23, pp. 1419–1424, 2005.

[51] Sánchez, F., Aguiar, R., Trtik, V., Guerrero, C., Ferrater, C., and Varela, M., "Epitaxial growth of $SrTiO_3$ (00h), (0hh), and (hhh) thin films on buffered Si(001)," *J. Mater. Res.*, vol. 13, pp. 1422–1425, 1998.

[52] Bardal, A., Matthee, T., Wecker, J., and Samwer, K., "Initial stages of epitaxial growth of Y-stabilized ZrO_2 thin films on a-SiO_x/Si(001) substrates," *J. Appl. Phys.*, vol. 75, pp. 2902–2910, 1994.

[53] Hirai, T., Teramoto, K., Koike, H., Nagashima, K., and Tarui, Y., "Initial stage and growth process of ceria, yttria-stabilized-zirconia and ceria-zirconia mixture thin films on Si(100) surfaces," *Jpn. J. Appl. Phys.*, vol. 36, pp. 5253–5258, 1997.

[54] Lubig, A., Buchal, C., Guggi, D., Jia, C. L., and Stritzker, B., "Epitaxial growth of monoclinic and cubic ZrO_2 on Si(100) without prior removal of the native SiO_2," *Thin Solid Films*, vol. 217, pp. 125–128, 1992.

[55] Wang, S. J., and Ong, C. K., "Epitaxial Y-stabilized ZrO_2 films on silicon: Dynamic growth process and interface structure," *Appl. Phys. Lett.*, vol. 80, pp. 2541–2543, 2002.

[56] Copetti, C. A., Soltner, H., Schubert, J., Zander, W., Hollricher, O., Buchal, C., Schulz, H., Tellmann, N., and Klein, N., "High quality epitaxy of $YBa_2Cu_3O_{7-x}$ on silicon-on-sapphire with the multiple buffer layer YSZ/CeO_2," *Appl. Phys. Lett.*, vol. 63, pp. 1429–1431, 1993.

[57] Yamada, T., Wakiya, N., Shinozaki, K., and Mizutani, N., "Epitaxial growth of $SrTiO_3$ films on CeO_2/yttria-stabilized zirconia/Si(001) with TiO_2 atomic layer by pulsed-laser deposition," *Appl. Phys. Lett.*, vol. 83, pp. 4815–4817, 2003.

[58] Wakiya, N., Yamada, T., Shinozaki, K., and Mizutani, N., "Heteroepitaxial growth of CeO_2 thin film on Si(001) with an ultra thin YSZ buffer layer," *Thin Solid Films*, vol. 371, pp. 211–217, 2000.

[59] Hirai, T., Nagashima, K., Koike, H., Matsuno, S., and Tarui, Y., "Crystal and electrical characterizations of epitaxial $Ce_xZr_{1-x}O_2$ buffer layer for the metal/ferroelectric/insulator/semiconductor field effect transistor," *Jpn. J. Appl. Phys.*, vol. 35, pp. 5150–5153, 1996.

[60] McKee, R. A., Walker, F. J., and Chisholm, M. F., "Crystalline oxides on silicon: The first five monolayers," *Phys. Rev. Lett.*, vol. 81, pp. 3014–3017, 1998.

[61] Ashman, C. R., Förster, C. J., Schwarz, K., and Blöchl, P. E., "First-principles calculations of strontium on Si(001)," *Phys. Rev. B*, vol. 69, p. 075309, 2004.

[62] Zhang, X., Demkov, A. A., Li, H., Hu, X., Wei, Y., and Kulik, J., "The atomic and electronic structure of the Si/SrTiO$_3$ interface," *Phys. Rev. B*, vol. 68, p. 125323, 2003.

[63] Först, C. J., Ashman, C. R., Schwarz, K., and Blöchl, P. E., "The interface between silicon and a high-K oxide," *Nature*, vol. 427, pp. 53–56, 2004.

[64] Lettieri, J., Haeni, J. H., and Schlom, D. G., "Critical issues in the heteroepitaxial growth of alkaline-earth oxides on silicon," *J. Vac. Sci. Technol. A*, vol. 20, pp. 1332–1340, 2002.

[65] Allen, P. B., Berger, H., Chauvet, O., Forro, L., Jarlborg, T., Junod, A., Revaz, B., and Santi, G., "Transport properties, thermodynamic properties, and electronic structure of SrRuO$_3$," *Phys. Rev. B*, vol. 53, pp. 4393–4398, 1996.

[66] Hartmann, A. J., Nielson, M., Lamb, R. N., Watanabe, K., and Scott, J. F., "Ruthenium oxide and strontium ruthenate electrodes for ferroelectric thin-film capacitors," *Appl. Phys. A*, vol. 70, pp. 239–242, 2000.

[67] Cheng, H. F., Ling, Y. C., and Lin, I. N., "Ferroelectric properties of $(Pb_xLa_{1-x})(Zr_yTi_{1-y})O_3$ thin films prepared by modified pulsed laser deposition process," *Jpn. J. Appl. Phys.*, vol. 40, pp. 231–238, 2001.

[68] Sai, N., Kolpak, A. M., and Rappe, A. M., "Ferroelectricity in ultrathin perovskite films," *Phys. Rev. B*, vol. 72, p. 020101, 2005.

[69] Yoshida, C., Yoshida, A., and Tamura, H., "Nanoscale conduction modulation in Au/Pb(Zr,Ti)O$_3$/SrRuO$_3$ heterostructure," *Appl. Phys. Lett.*, vol. 75, pp. 1449–1451, 1999.

[70] Izuha, M., Abe, K., Koike, M., Takeno, S., and Fukushima, N., "Electrical properties and microstructures of Pt/Ba$_{0.5}$Sr$_{0.5}$TiO$_3$/SrRuO$_3$ capacitors," *Appl. Phys. Lett.*, vol. 70, pp. 1405–1407, 1997.

[71] Lee, W. S., Ahn, K. C., Yoon, S. G., and Kim, C. S., "Effect of film thickness on the ferroelectric properties of $Pb(Zr_{0.2}Ti_{0.8})O_3$ thin films for nano-data storage applications," *J. Vac. Sci. Technol. B*, vol. 23, pp. 1901–1904, 2005.

[72] Bouchard, R. J., and Gillson, J. L., "Electrical properties of $CaRuO_3$ and $SrRuO_3$ single crystals," *Mater. Res. Bull.*, vol. 7, pp. 873–878, 1972.

[73] Kostic, P., Okada, Y., Collins, N. C., Schlesinger, Z., Reiner, J. W., Klein, L., Kapitulnik, A., Geballe, T. H., and Beasley, M. R., "Non-fermi-liquid behavior of $SrRuO_3$: Evidence from infrared conductivity," *Phys. Rev. Lett.*, vol. 81, pp. 2498–2501, 1998.

[74] Shannon, R. D., Shannon, R. C., Medenbach, O., and Fischer, R. X., "Refractive index and dispersion of fluorides and oxides," *J. Phys. Chem. Ref. Data*, vol. 31, pp. 931–970, 2002.

Chapter 3

Experimental techniques

3.1 Thin film growth

The preparation of optically transparent, perovskite PLZT epilayers requires careful fabrication procedures. A pyrochlore phase is preferentially formed at insufficient substrate temperatures, whereas a Pb deficient secondary phase appears for excessive substrate temperatures. Moreover, an insufficient O_2 partial pressure in the growth chamber during deposition may result in oxygen deficiency in the thin film. This implies that the range of substrate temperatures and O_2 partial pressures for which the perovskite phase of PLZT can be obtained is limited, placing strict demands on control of the process parameters during growth. A number of deposition techniques have been adopted for synthesis of PLZT thin films, including growth from chemical solution [1], pulsed laser ablation [2], metal-organic chemical vapor deposition [3], sputter deposition [4, 5], spin-coating pyrolysis [6], and sol-gel processing [7]. In this work, PLZT thin film epilayers were grown using radio frequency (RF) magnetron sputtering.

3.1.1 Radio frequency magnetron sputtering

Sputter deposition is a physical process, in which atoms are dislodged from a target material by bombardment with high-energy argon (Ar^+) ions and subsequently migrate through a plasma to settle on the substrate. Argon is used for sputtering due to the large momentum of the Ar^+ ions and their inert character. A schematic of the RF magnetron sputter apparatus used in this work is shown in Figure 3.1. The growth chamber is filled with argon gas, and sputtering

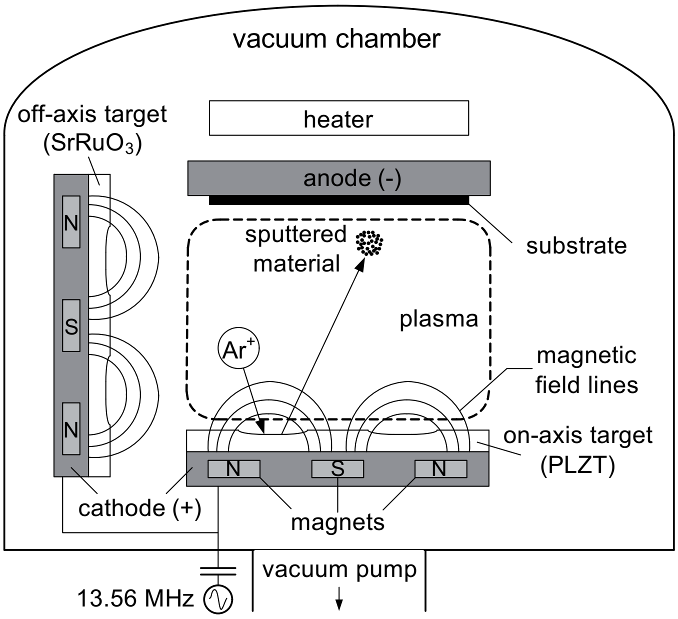

Figure 3.1: Schematic of the RF magnetron sputtering system used for deposition of PLZT and SRO thin films.

is initiated by applying an electric field between the electrodes (cathode and anode). This causes high-energy electrons to collide with argon atoms, detaching their outermost electrons to form a plasma (ionized gas). A self-biased electric field established by the potential difference between plasma and cathode accelerates the Ar^+ ions towards the target.

Thin film sputter deposition is carried out both with DC and AC voltage applied between the electrodes. DC sputtering allows for deposition of conducting materials only, since the electrodes become insulating and charge when coated with a dielectric, which implies that the plasma cannot be sustained. To overcome this problem for deposition of insulating thin films, RF sputtering is adopted. A capacitively coupled RF field is applied to the cathode. This assures that the glow discharge is sustained, since only the highly mobile electrons respond to the AC field. Ar^+ ions are attracted by the self-biased negative potential developed at the cathode. Thus, the Ar^+ ions are accelerated towards the target during one half-cycle, whereas charge neutrality is obtained from continuous ionization by the electrons emitted upon ionic impact in the other half-cycle. In order to enhance the efficiency of this ionization process, a magnetic field is commonly used to confine the electrons to regions near the target. This technique is referred to as magnetron sputtering. Magnets placed inside the cathode (cf. Figure 3.1) increase the ionization rate in the plasma near the target, allowing more ions to take part in the sputtering process. This results in increased deposition rates.

A customized magnetron sputtering system from Kurt J. Lesker Co., equipped with Torus magnetron cathodes, was used for deposition of PLZT and $SrRuO_3$ thin films. The substrates were radiatively heated *in situ*, and their surface temperature was measured with an optical pyrometer. The vacuum chamber base pressure was 5×10^{-8} Torr, and the overall gas pressure was controlled with a manually operated gate valve. The flow of Ar and O_2 (both of 99.9999 % purity) was regulated by mass-flow controllers. The $SrRuO_3$ and PLZT targets were both 3 inch diameter Praxair (99.9 % purity), solder bonded to a copper alloy disc. The RF (13.56 MHz) power was tuned to 90 W for deposition of PLZT and 100 W for $SrRuO_3$. The $SrRuO_3$ epilayers were deposited in a 90° off-axis sputter geometry, which has been proven advantageous to complex oxide thin film growth [8], with a target center to substrate separation of $\sim$100 mm. In order to achieve sufficient growth rates of films suitable for optical waveguide applications, i.e., with a typical thickness of $\sim$0.5 µm or more, the PLZT epilayers were deposited in a planar (on-axis) sputter geometry. The magnetron holding the PLZT target was mounted on a linear translation stage in order to allow for multilayer deposition.

3.1.2 Electron beam evaporation

Electron beam (e-beam) evaporation involves heating the source material to be deposited with a high-energy beam of electrons in a vacuum chamber. The modest process hazard and cost of e-beam evaporation render this technique convenient for contact metallization and coating, e.g., of anti-reflection and protective dielectric layers [9, 10]. A schematic of the e-beam evaporation system used in the present work is shown in Figure 3.2. Electrons are thermionically emitted from a tungsten filament. The emitted electrons are accelerated by an electrostatic potential, i.e., several kilovolts are applied between target and filament, and magnets are used to deflect the beam of electrons onto the crucible holding the source material. The focused e-beam evaporates material from the target, which in turn deposits on the substrate surface. The source material is normally in the form of sintered pellets, single crystals, or a melted ingot placed in a chemically inert crucible. Maintaining a high vacuum during the process is imperative in order to secure a sufficient

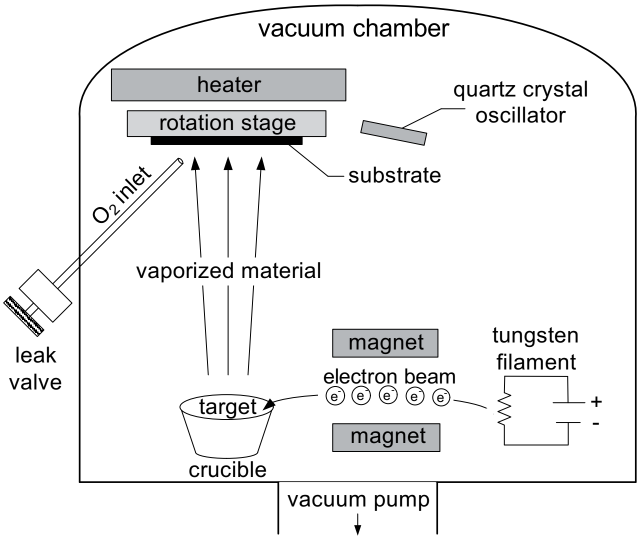

Figure 3.2: Schematic of the e-beam evaporation system used for deposition of CeO_2/YSZ buffer layers and for contact metallization.

mean free path for the evaporated material to reach the substrate. A high power density makes it possible to evaporate materials with a high melting point and with good control of the evaporation rate. Moreover, films can be grown with low risk of source contamination. Dissociation of compounds during e-beam evaporation is a common challenge, which may lead to non-stoichiometric transfer of material from source to substrate. Introducing oxygen to the vacuum chamber during growth of oxide layers may suppress this complication.

A customized e-beam evaporation system, Pfeiffer Vacuum Classic 500, equipped with an EV M-8 multitarget electron gun from Ferrofluidics, was used for deposition of CeO_2 and YSZ buffer layers, as well as for contact metallization. The chamber base pressure was maintained at $\sim 5 \times 10^{-8}$ mbar. The target materials were placed in 20 cm^3 graphite liners (Ferrotec), with a target-to-substrate separation of ∼30 cm. An acceleration voltage of 8 kV was applied to the crucible, using a HVP5-2 high-voltage source (Ferrofluidics). For epitaxial growth of CeO_2 and YSZ thin films[1], the substrate was radiatively heated using a ceramic heater. The flow of O_2 (99.999 % purity) was controlled using a manually operated leak valve. Continuous rotation of the substrate was adopted during growth. Film thickness and deposition rate were measured *in situ* by means of a quartz crystal oscillator (6 MHz), cf. Figure 3.2.

3.2 Materials characterization

The physical properties of thin films are investigated using a wide range of techniques, which provide valuable feedback to the process of high-quality thin film growth. Important attributes for application of PLZT epilayers in photonic waveguide devices include crystalline orientation, phase purity, composition uniformity, surface roughness, film thickness, ferroelectric behavior, and electro-optic response.

---

[1] The experimental details are given in Chapter 5.2

3.2.1 X-ray diffraction

X-ray diffraction (XRD) is used to address most issues related to the crystalline structure of bulk solids and thin films, including crystalline orientation, phases, size effects, defects, and strain. Figure 3.3 shows a schematic of the interaction between an incident beam of x-rays scattered from a crystalline solid. For a set of atomic lattice planes with separation d, the scattered x-rays will interfere constructively in such directions which satisfy the equation,

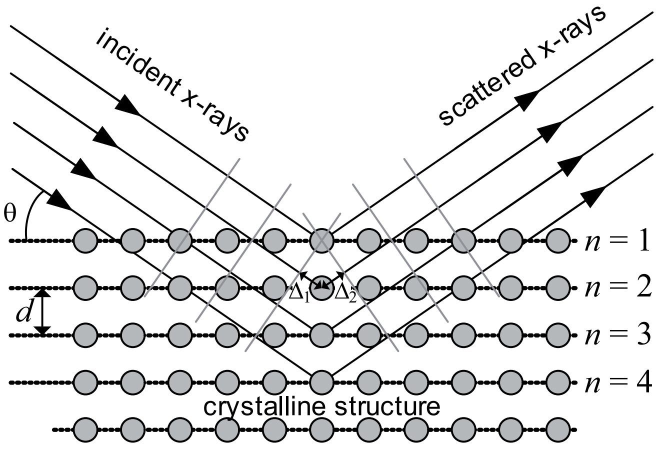

Figure 3.3: Scattering of incident x-rays off atomic lattice planes. Constructive interference occurs when the total phase shift ($\Delta_1 + \Delta_2$) *equals an integer multiple of the x-ray wavelength,* λ.

$$2d \sin\theta = n\lambda, \tag{3.1}$$

known as the diffraction condition or Braggs equation. Here, θ is the angle of incidence, n is an integer which represents the order of diffraction, and λ is the x-ray wavelength.

Figure 3.4 shows a schematic of the x-ray goniometer along with the different angles relevant to the XRD analysis of thin film samples. 2θ corresponds to the angle between the detector and the incident beam, whereas ω corresponds to the angle between the plane of the thin film sample and the incident beam. Information about the

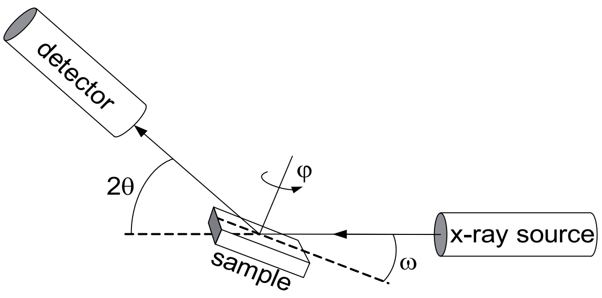

Figure 3.4: The 2θ, ω, and φ angles of the x-ray goniometer.

crystalline structure can be obtained by performing different types of angular scans, such as the *θ-2θ-scan*, during which the detector moves an angle 2θ while the sample is rotated through an angle θ, the *ω-scan*, which is performed by scanning the angle ω while keeping 2θ fixed, commonly referred to as *rocking curve*, the *φ-scan*, which is performed by in-plane rotation of the sample while keeping the angles ω and 2θ fixed, and *reciprocal space mapping*, which involves assembling θ-2θ-scans with different ω offsets.

The thickness of crystalline thin films can be determined from x-ray reflectivity (XRR) measurements, provided that the film thickness is less than ~50 nm. This involves performing θ-2θ-scans at a grazing angle, e.g., ~0–3°. Figure 3.5 shows the XRR scan for a ~25 nm thick PLZT epilayer grown on STO(001). The overall decline in intensity with increasing 2θ and the amplitude of the intensity oscillations are correlated with the roughness of the film surface and the substrate interface, e.g., increased surface roughness results in a reduced oscillation amplitude and a steeper slope for the reflected intensity. The layer thickness is estimated from a numerical fit to the recorded XRR curve [11].

3.2.2 Atomic force microscopy

Atomic force microscopy (AFM) provides high resolution topography data for thin solid films [12]. The basic principle of the microscope is depicted in Figure 3.6. A probe tip is brought in close proximity to

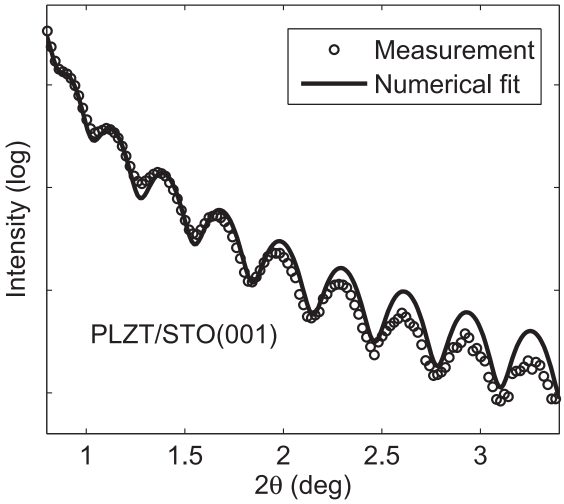

Figure 3.5: X-ray reflectivity scan for a PLZT thin film grown on $SrTiO_3$*. The film thickness is estimated by running a numerical fit (solid line) to the recorded reflectivity data [11].*

the sample surface, inducing atomic force interactions which deflect the probe. While raster scanning the sample with a piezoelectric actuator, a HeNe laser beam reflected off the probe cantilever is monitored with a split photodiode detector and used to measure the probe deflection. From these measurements, three-dimensional topographic images of the sample surface are constructed, with typical resolution on the nanometer scale. Precise control of the tip-sample separation is achieved using a feedback loop, which is required in order to prevent the tip from crashing into the surface during raster scanning. Specific sample preparation is generally not required, and the measurements can be performed in vacuum, air, or a liquid ambient.

In the present work, the film surface topography was examined with tapping mode AFM. This implies that the probe oscillates near its resonance frequency during scanning, lightly tapping the sample surface on each oscillation. This technique reduces the risk of damage to soft samples. Moreover, common problems associated with conventional contact mode AFM, such as friction, adhesion, and electrostatic forces, are more easily overcome.

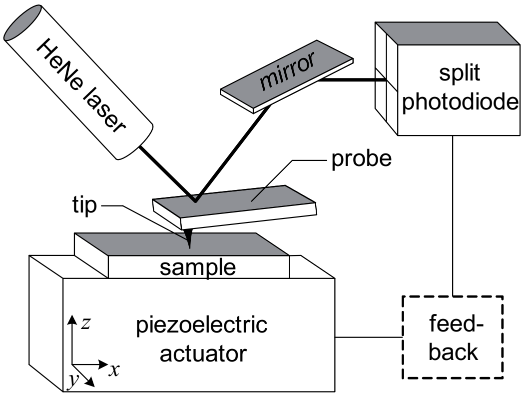

Figure 3.6: Schematic of the atomic force microscope.

3.2.3 Auger electron spectroscopy

Auger electron spectroscopy (AES) utilizes the emission of electrons emanating from Auger processes to determine the elemental composition of solid surfaces. The sample is scanned with an energetic beam of electrons with a spot size of ~10 nm. Hence, AES provides excellent lateral resolution for detection of surface elemental concentrations less than 1 %. The inelastic mean free path of electrons in a solid is typically 5–50 Å [13]. Thus, elastic Auger electrons can only escape from the first 5–10 subsurface monolayers, which makes AES a highly surface sensitive technique [14].

The Auger process

The Auger process refers to the relaxation of an ionized atom by emission of a second electron. This process is depicted in Figure 3.7 and involves the following steps:

1. Excitation of an inner shell electron, e.g., from the K-shell, to form a vacancy.

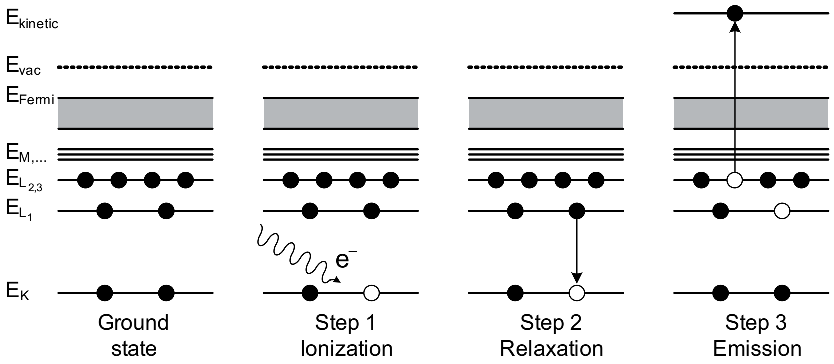

Figure 3.7: Schematic of the basic steps in Auger emission.

2. Recombination with the excited core hole by an electron from a higher shell, e.g., an L_1 electron, with the energy released in this process excitation of a third electron from an outer shell, e.g., the $L_{2,3}$-level.

3. With sufficient kinetic energy, this third electron, referred to as an Auger electron, is emitted from the atom. The kinetic energy of the Auger electron is independent of the energy of the incident electron beam.

For the Auger process specified above, the emitted electron is referred to as a KLL Auger electron, from the three electron energy levels involved in this process. An Auger process involves a minimum of three electrons, which implies that hydrogen and helium cannot be detected by AES.

The Auger spectrum

The kinetic energy of the Auger electron is unique to the atom from which it originates. Figure 3.8(a) shows a typical Auger spectrum recorded on a PLZT thin film surface. The surface elemental composition is thus determined from the energy positions of the Auger peaks. Figure 3.8(b) shows the corresponding differentiated spectrum. The differential peak minima are used for accurate determination of the Auger kinetic energies, as they provide a more precise

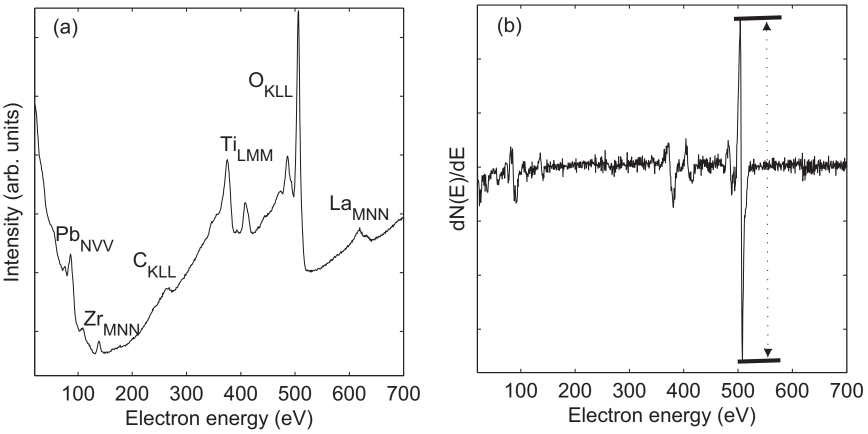

Figure 3.8: (a) Auger spectrum from the surface of a PLZT thin film and (b) the corresponding differentiated spectrum.

reference point than can be readily determined from the integrated spectra.

Auger depth profiling

The variation of elemental concentration with depth below the surface of a sample can be assessed by Auger depth profiling. Depth profiles are obtained using a beam of inert ions (usually Ar^+) to gradually remove (sputter) material from the analyzed surface region. Alternate sputtering and AES analysis are adopted to construct a depth profile of the elemental composition, with a typical depth resolution of a few nanometers. Auger depth profiling is well suited to examine the interfaces of multilayer thin films [15].

3.2.4 X-ray photoelectron spectroscopy

X-ray photoelectron spectroscopy (XPS), also known as electron spectroscopy for chemical analysis (ESCA), is a surface analytical technique based on the photoelectric effect. XPS involves irradiation of a sample with x-rays, resulting in the emission of photoelectrons from the topmost surface region [14]. The photoemission process is shown schematically in Figure 3.9. The kinetic energy of an elastically emitted photoelectron, measured with respect to the vacuum energy level (E_{vac}), is given by

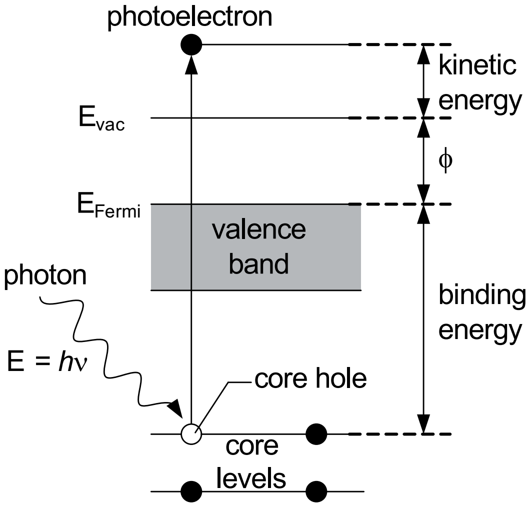

Figure 3.9: Schematic of the photoemission process. An energetic photon (x-ray) is absorbed by a core level electron. The excited electron is transported to the surface and may escape from the material in the form of a photoelectron.

$$\mathrm{KE} = h\nu - \phi + \mathrm{BE}, \tag{3.2}$$

where $h\nu$ is the photon energy, ϕ is the work function of the analyzer, and BE is the binding energy of the electron. The emitted photoelectrons are collected with an electrostatic lens and passed through an energy analyzer, which allows for precise determination of their kinetic energies.

Figure 3.10 shows a typical XPS survey scan of a PLZT thin film surface. Elements are identified by the binding energy at which the XPS peaks appear. The peaks represent photoexcited core level electrons having escaped from the surface of the sample without energy losses from inelastic scattering. The characteristic background of the

XPS spectrum, i.e., the reduced background count rate with decreasing binding energy, originates from emission of secondary electrons which suffered inelastic scattering before leaving the sample.

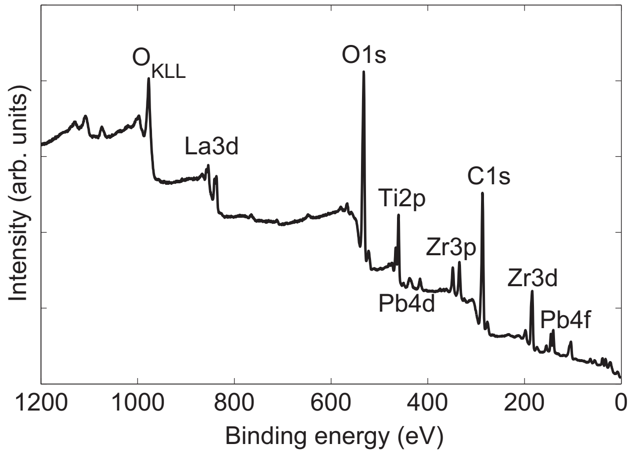

Figure 3.10: XPS survey scan of a PLZT thin film surface.

3.2.5 Prism coupling measurements

The prism coupling technique provides easy access to the optical properties of thin films [16]. A schematic of the prism-film coupler used in the present work is shown in Figure 3.11. The thin film sample is pressed firmly against the base of a prism in order to reach a prism-film separation d_0 of less than $\lambda_0/4$ [17]. Light directed into the prism undergoes total reflection at the prism base. Reflected light emerging from the right face of the prism is projected onto a detector screen. Propagating optical modes are excited in the optical thin film at certain angles of incidence θ_{in}, via overlapping evanescent fields [18]. The energy losses associated with this excitation can be visually observed as a pattern of streaks, referred to as m-lines, on the detector screen, revealing the mode spectrum of the optical thin film. The fundamental equations of the prism-film coupling are given in Appendix B.

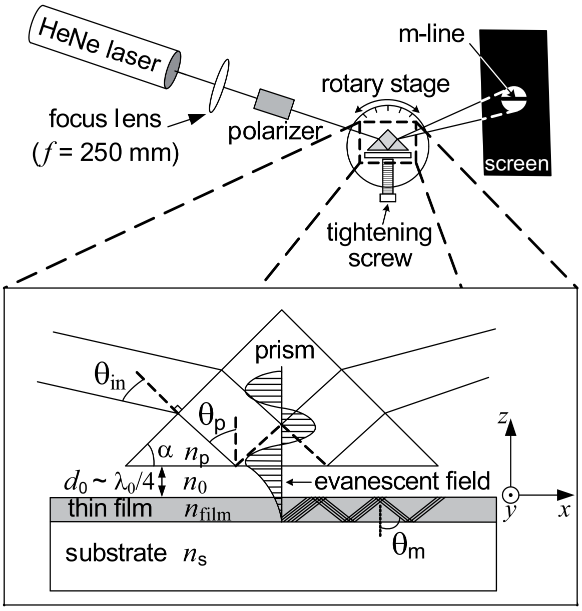

Figure 3.11: Schematic of the prism-film coupler. The incident focused laser beam is totally reflected at the base of the prism. At certain angles of incidence θ_{in}, guided optical modes are selectively excited, and energy is coupled into the film by optical tunneling. This prism-film coupling is observed as m-lines on the detector screen. The m-lines are used to estimate numerically the thickness d and refractive index n of the optical thin film.

The prism coupling technique places certain requirements on the components of this setup. The prism material must be hard and optically transparent, with a refractive index which is higher than that of the film. Thus, for characterization of high-index films there is a limited selection of prism materials available. The most commonly used materials are $SrTiO_3$, TiO_2 (rutile), Si, Ge, and high-index glasses. The surface roughness of the prism base should be less than $\lambda_0/2$. For accurate determination of the film parameters, the film must be sufficiently thick in order for two or more optical modes to be supported. Furthermore, it is imperative to keep the coupling spot stationary during rotation of the prism. The prism-film coupler arrangement used in this work, cf. Figure 3.11, consists of a HeNe laser, a focal lens ($f = 250$ mm), a polarizer, a rotary stage, and a rutile prism. The specifications of the rutile prism and the laser are provided in Table 3.1.

Table 3.1: Specifications of the rutile prism and laser used in the prism-film coupler set-up

	Specifications
Prism	ADT-6 rutile prism, 45°–45°–90°, 6×6 mm^2 base, refractive index: $n_\mathrm{o} = 2.58$, $n_\mathrm{e} = 2.87$ ($\lambda = 632.8$ nm)
Laser	Melles Griot LP-230, HeNe, $P = 5$ mW (CW), $\lambda = 632.8$ nm

3.2.6 Spectroscopic ellipsometry

Spectroscopic ellipsometry is commonly used to determine the complex refractive index, the extinction coefficient, and the thickness of optical thin films [19, 20]. The technique is based on observing the relative phase change of polarized light reflected from the film surface, and is a non-destructive technique, suitable for *in situ* studies. A schematic of a spectroscopic ellipsometer is shown in Figure 3.12(a). The set-up consists of a broadband light source, a monochromator for single wavelength selection, a polarizer, an analyzer, and a photodetector. In general, the phase shift caused by reflection of linearly polarized light from a surface is different for p- and s-polarization. This results in elliptical polarization of the reflected wave. Thus, for a known polarization of the incident light, the optical properties of the thin film can be obtained by measuring the state of polarization of the reflected light. This implies that relative changes in the polarization are measured rather than absolute intensities.

The fundamental equation of ellipsometry is given by [21]

$$\rho = \frac{r^p}{r^s} = \tan \Psi e^{i\Delta}, \tag{3.3}$$

where r^p and r^s represent the Fresnel reflection coefficients for the p (parallel) and s (perpendicular) polarization, respectively (cf. Fig-

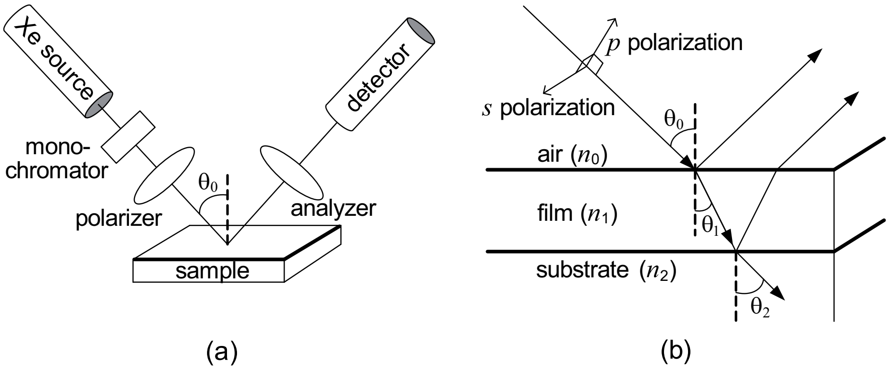

Figure 3.12: (a) Schematic of a spectroscopic ellipsometer. (b) The refraction of polarized light from a thin film structure. The p- and s-polarization correspond to an electric field vector parallel and perpendicular to the plane of incidence, respectively.

ure 3.12(b)), and Ψ and Δ represent the ellipsometric parameters extracted from experimental measurements. More specifically, $\tan\Psi$ corresponds to the ratio of the amplitudes for parallel and perpendicular polarization,

$$\tan\Psi = \frac{|r^p|}{|r^s|}, \tag{3.4}$$

whereas Δ corresponds to the difference in phase (δ) between the parallel and perpendicular polarization,

$$\Delta = \delta_{r^p} - \delta_{r^s}. \tag{3.5}$$

For reflection of light from a single interface between air (medium 0) and a solid (medium 1), with complex refractive indices $\hat{n}_0 = n_0 + ik_0$ and $\hat{n}_1 = n_1 + ik_1$, respectively, the Fresnel reflection coefficients can be expressed on the form,

$$r^p_{01} = |r^p|e^{i\delta_{r^p}} = \frac{\hat{n}_0\cos\theta_1 - \hat{n}_1\cos\theta_0}{\hat{n}_0\cos\theta_1 + \hat{n}_1\cos\theta_0} \tag{3.6}$$

and

$$r^s_{01} = |r^s|e^{i\delta_{r^s}} = \frac{\hat{n}_0\cos\theta_0 - \hat{n}_1\cos\theta_1}{\hat{n}_0\cos\theta_0 + \hat{n}_1\cos\theta_1}. \tag{3.7}$$

For reflection of light from a thin film on a substrate (medium 2), cf. Figure 3.12(b), the total reflection coefficient (reflectance) for the p and s polarization become,

$$R^p = |r^p|^2 = \frac{r^p_{01} + r^p_{12} e^{-i2\beta}}{1 + r^p_{01} r^p_{12} e^{-i2\beta}} \tag{3.8}$$

and

$$R^s = |r^s|^2 = \frac{r^s_{01} + r^s_{12} e^{-i2\beta}}{1 + r^s_{01} r^s_{12} e^{-i2\beta}} \ , \tag{3.9}$$

respectively, where $\beta = 2\pi\,(d_1/\lambda_0)\,\hat{n}_1 \cos\theta_0$ is the phase change for a wave propagating from the top surface to the bottom interface of the thin film. Here, d_1 denotes the film thickness (medium 1) and λ_0 the wavelength in medium 0. Eqs. 3.4–3.9 are coupled, which implies that by measuring the ellipsometric parameters (Δ, Ψ), d_1 and $\hat{n}_1$ can be obtained numerically, as long as the complex refractive indices of the surrounding media are known.

3.3 Device fabrication

The introduction of PLZT thin films in optical waveguide devices requires a thorough understanding of their electro-optic response, which calls for fabrication of a functional device. This section describes the fabrication of a thin film Mach-Zehnder interferometer, as well as the processing of photonic crystal slabs using focused ion beam etching.

3.3.1 Photolithography and chemical wet etching

Ridge-type waveguides, including the Mach-Zehnder interferometer, were defined in PLZT thin films using UV photolithography and chemical wet etching, according to a recipe proposed by Zheng *et al.* [22]. The different processing steps and the processing parameters are summarized in Table 3.2. A Karl Suss MA56 mask aligner (i-line, $\lambda = 365$ nm) was used to expose the photoresist through a chromium mask from Compugraphics Photomask Solutions in contact mode.

Table 3.2: Processing steps and corresponding parameters used for fabrication of the ridge-type Mach-Zehnder interferometer.

Process step	Parameters
Rinse	Acetone with ultrasonic agitation, rinse with IPA
Dehydration	100°C for 10 minutes on hot plate
Primer	Hexamethyl disulizid (HMDS), 4000 rpm for 20 s
Resist (pos.)	Microposit S1818 G2 (Shipley), 4000 rpm for 20 s
Resist (neg.)	ma-N 1420 (Micro Resist Technology), 4000 rpm, 20 s
Soft bake	100°C for 60 s on hot plate
Exposure	22 s (neg.) and 6.2 s (pos.) at 10 mW/cm^2
Develop (pos.)	Microposit MF-86 MX for 45 s, rinse in deionized water
Develop (neg.)	ma-D 533 for 85 s, rinse in deionized water
Hard bake	130°C for 120 s on hot plate
Etchant [22]	$(1BHF:2HCl:4NH_4Cl:4H_2O):H_2O = 1:19$, rate = 6 nm/s
Residue removal	$NHO_3:H_2O = 2:1$ for 30 s
Resist stripping	Acetone with ultrasonic agitation, rinse with IPA

IPA = isopropyl alcohol, BHF = buffered HF

Metallization and lift-off

In order to define the co-planar electrodes of the Mach-Zehnder interferometer, metal layers of Pt (10 nm) and Au (200 nm) were deposited by e-beam evaporation. Negative resist was used for the subsequent patterning, which was carried out with the parameters listed in Table 3.2. The Pt layer was introduced in order to improve adhesion. Lift-off was carried out by ultrasonic agitation in acetone for 10 minutes, with a subsequent rinse in isopropyl alcohol. A microscope image of the Mach-Zehnder interferometer processed in PLZT on an MgO substrate is shown in Figure 3.13.

Mechanical polishing of waveguide facets

The waveguide end facets were mechanically polished using a Multi-Prep System from Allied High Tech Products. In order to prevent delamination of film and substrate upon polishing, a 28 µm thick glass plate was attached to the sample surface using hot mounting

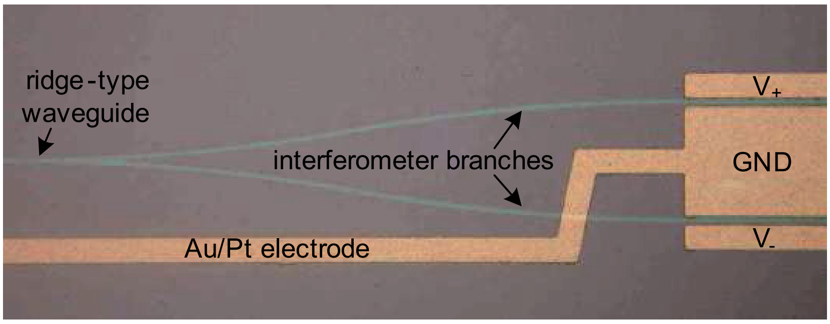

Figure 3.13: Microscope image of ridge-type Mach-Zehnder interferometer with co-planar electrodes.

wax. Diamond lapping (Allied High Tech Products) with particles ranging from 0.5 to 30 µm in diameter was used for this polishing, which was performed in a unidirectional fashion, perpendicular to the sample surface from the substrate towards the glass plate. The mounting wax was subsequently removed from the sample surface using acetone.

3.3.2 Focused ion beam etching

Focused ion beam (FIB) etching has become an increasingly important tool for high-resolution imaging and device processing [23–25]. The capability to image, mill, and deposit material with lateral resolution down to ∼5 nm has lead to widespread use of FIB in technological applications, such as micro- and nanomachining, circuit editing, sample preparation for tunneling electron microscopy, and materials analysis. The main merit of FIB for fabrication of nanoscale structures is maskless etching, i.e., removal of material from a selected localized area without using a patterned mask [26]. This enables rapid device prototyping without the need for a resist, an etching mask, or the development of a complicated etching recipe. The FIB technique also allows for direct processing of non-planar and prepatterned samples.

FIB etching is commonly used to define structures of high aspect ratios, e.g., deep narrow trenches or holes. However, the sputtered atoms tend to adsorb upon collision with nearby surfaces. Hence, some of the ejected material is redeposited on the processed surface. As the trenches are made deeper, this effect becomes increasingly severe until the rate of redeposition equals the rate of sputtering. Redeposition depends on a number of physically and chemically controlled variables, such as the scanning pattern, the geometry of the processed feature, the sticking coefficient and sputtering yield of the target material, and the dynamics of the ejected molecules [27]. Aspect ratios (i.e., depth to width) in the range 5:1–10:1 have been reported for photonic crystal structures defined by FIB etching [28–30].

In the present study, thin film photonic crystals were prepared using a FEI Strata 235DB FIB/SEM system, containing both an ion beam column and a high resolution field emission scanning electron microscope (SEM) column. Figure 3.14 shows a schematic of the dual-beam FIB/SEM system, which allows for fast and accurate alignment of the photonic crystal structures to a pre-patterned optical waveguide, as well as for real-time inspection of the FIB-etched patterns. The residual pressure in the vacuum chamber was maintained below 5×10^{-5} mbar. Gallium ions from a liquid metal ion source (LMIS) were accelerated to 30 kV and focused to a spot size of ∼5–10 nm diameter by electrostatic lenses. A set of blanking apertures of different diameter defined the spot size to yield ion beam currents in the range ∼10–2000 pA. In general, the resolution is increased by reducing the beam current, at the expense of prolonged processing times. The energy transfer resulting from bombardment of the surface by Ga^+ ions results in sputter etching of the sample as well as generation of secondary ions and electrons. This ion-beam induced secondary emission is collected in the detector for *in-situ* monitoring of the processed surface. The purpose of the electron column is to enable non-destructive, high-resolution imaging, e.g., for alignment and inspection of the sample surface. The erosion of a given target material depends on a number of factors, including beam current and energy, incidence angle, and the geometry of the ion-etched structures. Moreover, the manner in which the ion-beam is scanned across the sample matters, dependent on parameters such as the beam dwell time, magnification, spot overlap, and milling sequence.

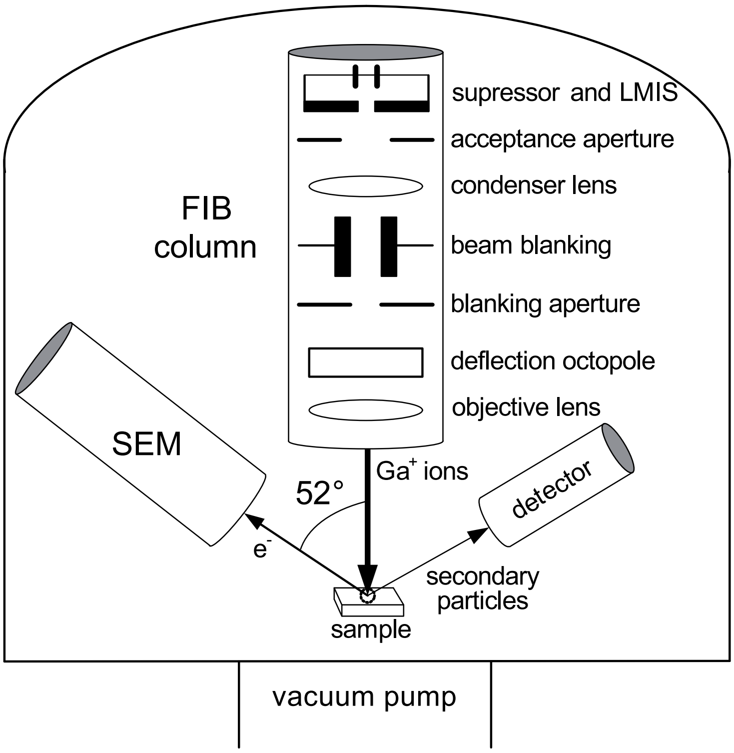

Figure 3.14: Schematic of a dual-beam FIB/SEM system along with the components of the ion beam column.

3.4 Electro-optic measurement set-up

The experimental set-up for end-fire coupling of infrared (IR) light ($\lambda_0 = 1550$ nm) into the thin film waveguide device is depicted in Figure 3.15. The device and the polarization conserving, single-mode tapered lensed fibers are mounted to a flexure stage, allowing for individual alignment of device and fibers along the x, y, and z axes. The polarization of the input light is controlled with an in-fiber polarizer, i.e., the light is linearly polarized, the direction of which can be rotated in the y–z plane. The transmitted intensity at the waveguide output is measured with an IR photodetector connected to a digital oscilloscope. Contact needles attached to probe-head manipulators are used to apply a modulation voltage to the electrodes of the Mach-Zehnder interferometer.

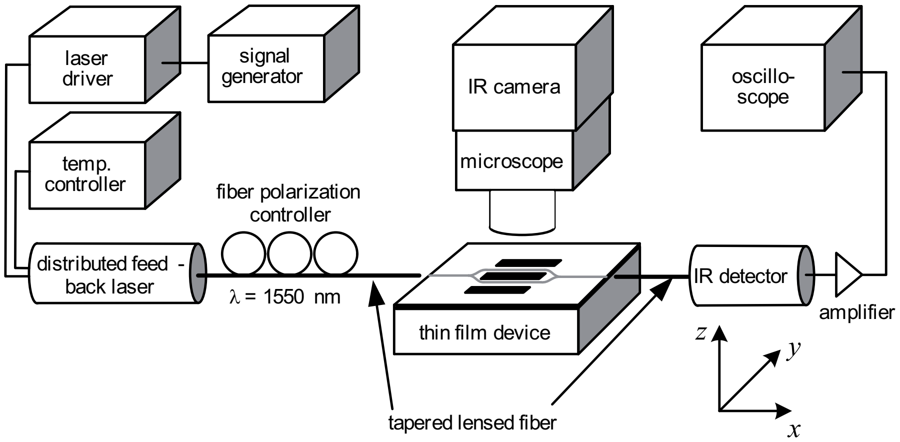

Figure 3.15: Schematic of the optical measurements set-up for coupling of IR light into the thin film waveguide device.

A microscope objective coupled to an IR video camera is mounted above the device in order to monitor light propagation along the waveguide. Figure 3.16 shows an IR image of out-of-plane scattered intensity from light propagating through the Y-junction of a ridge-type Mach-Zehnder interferometer, defined in PLZT on MgO. The equipment used in the optical measurements set-up is listed in Table 3.3.

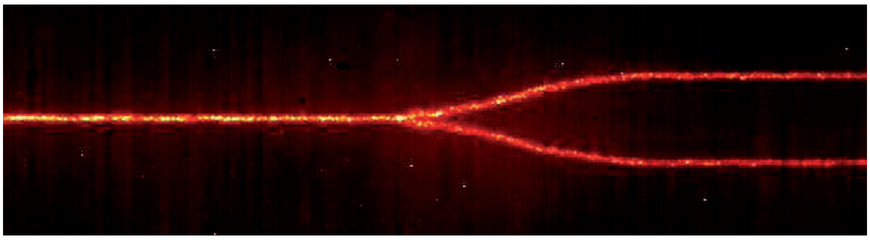

Figure 3.16: IR image of out-of-plane scattered intensity from light (λ_0 = 1550 nm) propagating (from left to right) through the Y-junction of a ridge-type Mach-Zehnder interferometer.

Table 3.3: Equipment used in the optical measurements set-up.

Component	**Manufacturer & model**
CW distributed feedback laser	Anritsu GB-5A-016
Laser driver	Newport Model 505
Laser temperature controller	Newport Model 325
Signal generator	Hewlett Packard 33120A
Single-mode tapered lensed fibers	Nanonics Imaging
XYZ flexure stage	Elliot Scientific Ltd. MDE881
In-fiber polarizer	Chiral Photonics IFP-155D-SM
IR video camera	Xenics XEVA-FPA-1.7-640
IR photodetector	InGaAs-PIN
Digital oscilloscope	Tektronix TDS2004B
Probe-head manipulators	Süss MicroTec PH100

References

[1] Moon, S., Kwak, M., Kim, Y. T., Ryu, H. C., Lee, S. J., and Kang, K. Y., "Microwave dielectric properties for (Pb,La)(Zr,Ti)O_3 thin films on MgO(001) substrate grown by chemical solution deposition," *Int. Ferroelectr.*, vol. 77, pp. 37–44, 2005.

[2] Cheng, H. F., "Spectroscopic characteristics of $Pb_{0.95}La_{0.05}(Zr_{1-y}Ti_y)_{0.9875}O_3$ plasma and growth behavior of thin films by pulsed laser deposition," *J. Appl. Phys.*, vol. 78, pp. 4633–4639, 2005.

[3] Okada, M., and Tominaga, K., "Preparation and properties of (Pb,La)(Zr,Ti)O_3 thin films by metalorganic chemical vapor deposition," *J. Appl. Phys.*, vol. 71, pp. 1955–1959, 1992.

[4] Boyer, L. L., Wu, A. Y., Metzger, G. W., and Mcneil, J. R., "Properties of ion beam deposited $Pb_{1-x}La_x(Zr_yTi_z)_{1-x/4}O_3$," *J. Vac. Sci. Technol. A*, vol. 7, pp. 1199–1201, 1989.

[5] Ramakrishnan, E. S., and Howng, W. Y., "Ferroelectric lead zirconate titanate thin films by radio frequency magnetron sputtering," *J. Vac. Sci. Technol. A*, vol. 10, pp. 69–74, 1992.

[6] Cross, J. S., Tomotani, M., and Kotaka, Y., "(Pb,La)(Zr,Ti)O_3 film grain-boundary conduction with $SrRuO_3$ top electrodes," *Jpn. J. Appl. Phys.*, vol. 40, pp. L346–L348, 2001.

[7] Yoon, D. S., Kim, C. J., Lee, J. S., Lee, W. J., and No, K., "Epitaxial growth of sol-gel PLZT thin films," *J. Mater. Res.*, vol. 9, pp. 420–425, 1994.

[8] Triscone, J.-M., Frauchiger, L., Decroux, M., Mieville, L., Fischer, Ø., Beeli, C., Stadelmann, P., and Racine, G.-A., "Growth and structural properties of epitaxial $Pb(Zr_xTi_{1-x})O_3$ films and $Pb(Zr_xTi_{1-x})O_3$-cuprate heterostructures," *J. Appl. Phys.*, vol. 79, pp. 4298–4305, 1996.

[9] Ohring, M., *The Materials Science of Thin Films.* London, UK: Academic Press, 1992.

[10] Schiller, S., "High-rate electron beam evaporation," *Thin Solid Films*, vol. 110, pp. 149–164, 1983.

[11] Parratt, L. G., "Surface studies of solids by total reflection of x-rays," *Phys. Rev.*, vol. 95, pp. 359–369, 1954.

[12] Binnig, G., Quate, C. F., and Gerber, C., "Atomic force microscope," *Phys. Rev. Lett.*, vol. 56, pp. 930–933, 1986.

[13] Werner, W. S. M., Tomastik, C., Cabela, T., Richter, G., and Stori, H., "Electron inelastic mean free path measured by elastic peak electron spectroscopy for 24 solids between 50 and 3400 eV," *Surf. Sci. Lett.*, vol. 470, pp. L123–L128, 2000.

[14] Lindau, I., and Spicer, W. E., "The probing depth in photoemission and auger-electron spectroscopy," *J. Electron Spectrosc.*, vol. 3, pp. 409–413, 1974.

[15] Menyhard, M., Konkol, A., Gergely, G., and Barna, A., "Development in Auger depth profiling technique," *Journal of Electron Spectroscopy and Related Phenomena*, vol. 68, pp. 653–657, 1994.

[16] Tien, P. K., Ulrich, R., and Martin, R. J., "Modes of propagating light waves in thin deposited semiconductor films," *Appl. Phys. Lett.*, vol. 14, pp. 291–294, 1969.

[17] Tien, P. K., "Light waves in thin film and integrated optics," *Appl. Opt.*, vol. 10, pp. 2395–2413, 1971.

[18] Tien, P. K., and Ulrich, R., "Theory of prism-film coupler and thin-film light guides," *J. Opt. Soc. Am.*, vol. 60, pp. 1325–1337, 1970.

[19] Theeten, J. B., and Aspnes, D. E., "Ellipsometry in thin film analysis," *Ann. Rev. Mater. Sci.*, vol. 11, pp. 97–122, 1981.

[20] Fujiwara, H., *Spectroscopic Ellipsometry: Principles and Applications.* John Wiley and Sons, 2007.

[21] Drude, J. *Ann. Phys.*, vol. 32, p. 584, 1887.

[22] Zheng, K., Lu, J., and Chu, J., "A novel wet etching process of Pb(Zr,Ti)O_3 thin films for applications in microelectromechanical system," *Jpn. J. Appl. Phys.*, vol. 43, pp. 3934–3937, 2004.

[23] Seliger, R. L., and Fleming, W. P., "Focused ion beams in microfabrication," *J. Appl. Phys.*, vol. 45, pp. 1416–1422, 1974.

[24] Melngailis, J., "Focused ion beam technology and applications," *J. Vac. Sci. Technol. B*, vol. 5, pp. 469–495, 1987.

[25] Reyntjens, S., and Puers, R., "A review of focused ion beam applications in microsystem technology," *J. Micromech. Microeng.*, vol. 11, pp. 287–300, 2001.

[26] Orloff, J., Utlaut, M., and Swanson, L., *High Resolution Focused Ion Beams: FIB and Its Applications.* New York, USA: Kluwer Academic, 2003.

[27] Tseng, A. A., “Recent developments in nanofabrication using focused ion beams,” *Small*, vol. 1, pp. 924–939, 2005.

[28] Freeman, D., Madden, S., and Luther-Davies, B., “Fabrication of planar photonic crystals in a chalcogenide glass using focused ion beam,” *Opt. Express*, vol. 13, pp. 3079–3086, 2005.

[29] Dale, G., Langford, R. M., Ewen, P. J. S., and Reeves, C. M., “Fabrication of photonic band gap structures in $As_{40}S_{60}$ by focused ion beam milling,” *J. Non-Cryst. Solids*, vol. 266, pp. 913–918, 2000.

[30] Cabrini, S., Businaro, L., Prasciolu, M., Carpentiero, A., Gerace, D., Galli, M., Andreani, L. C., Riboli, F., Pavesi, L., and Fabrizio, E. D., “Focused ion beam fabrication of one-dimensional photonic crystals on Si_3N_4/SiO_2 channel waveguides,” *J. Opt. A: Pure Appl. Opt.*, vol. 8, pp. S550–S553, 2006.

Chapter 4

Guided optical modes in thin film waveguides and photonic crystal slabs

Planar optical components and integrated optics rely on the confinement of light in thin film waveguides. Conventional optical waveguides are based on index confinement, i.e., light is guided by total internal reflection. For line-defect waveguides in photonic crystal slabs (cf. Figure 1.4), in-plane localization of the light is ensured by the surrounding periodic dielectric structure, which prohibits propagation of light for wavelengths within a photonic band gap.

4.1 Ridge-type waveguides

Figure 4.1 shows a schematic of a ridge-type waveguide in an optical thin film on a substrate. The most common processing technique for definition of such waveguides is UV lithography followed by selective etching of the thin film surface. The film thickness h is typically on the order of the optical wavelength ($\sim$1 µm). For an optically transparent thin film to support propagating modes, the refractive index of the film, n_{film}, must be larger than that of the substrate, n_{sub}, i.e., light coupled into the thin film is confined by total internal reflection when

$$\theta \leq \sin^{-1}\sqrt{n_{\text{film}}^2 - n_{\text{sub}}^2}, \tag{4.1}$$

where θ is the angle of incidence relative to the film plane.

The capability of the ridge to confine propagating modes laterally is determined by the height d and width W of the ridge. The waveguide is referred to as single-mode when only the fundamental mode is supported and multi-mode when a finite number of modes are supported [1]. The cutoff frequency is defined as the lowest frequency for which a specific mode will propagate in the waveguide, i.e., below the cutoff frequency the mode is not confined to the waveguide and becomes radiative. The cutoff frequency is determined by the geometry of the ridge (W, d, and h) as well as the optical properties of the thin film and substrate. Rigorous three-dimensional analysis of mode propagation in such waveguides requires numerical calculations, i.e., the wave equations cannot be solved analytically.[1]

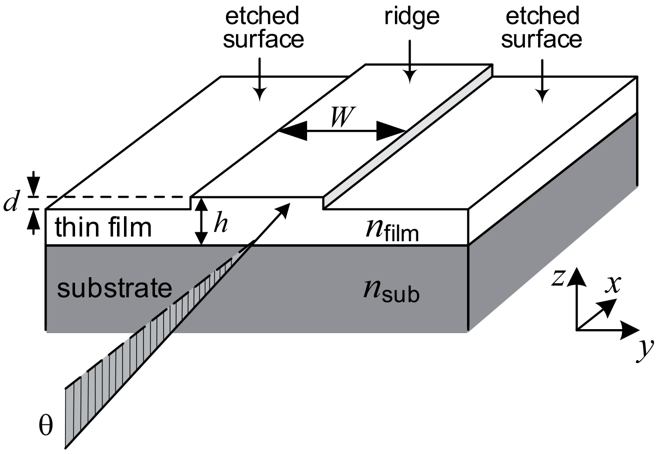

Figure 4.1: Schematic of the ridge-type waveguide. W, d, and h denote the ridge width, ridge height (i.e., etch depth), and film thickness, respectively.

---

[1] The design of ridge-type waveguides and a Mach-Zehnder interferometer in PLZT thin films on MgO substrate is presented in Appendix C

Electro-optic waveguide modulators utilizing phase retardation of propagating modes are key components in integrated optics. The electro-optic properties of perovskite oxide thin films are highly anisotropic [2], which implies that the characteristics of an electro-optic device processed in such films will depend on a number of factors, including waveguide orientation, polarization of the propagating modes, crystalline orientation of the thin film, and direction of the applied electric field. A sketch of the electric field distribution for a ridge-type waveguide with planar and co-planar electrode geometry is shown in Figures 4.2(a) and (b), respectively. The planar electrode geometry provide for a high electric field in the active layer, compatible with low-voltage operation. However, cladding layers (hatched in Figure 4.2(a)) are normally required to reduce optical absorption in the metallic electrodes. The incorporation of such layers complicates fabrication of the device. Hence, the co-planar electrode geometry, which can be readily processed using established UV lithography techniques, is commonly adopted to ensure low optical absorption. The drawback is the larger separation between the electrodes for this geometry, which implies a reduced electric field for a fixed applied voltage compared to that for the planar electrode geometry.

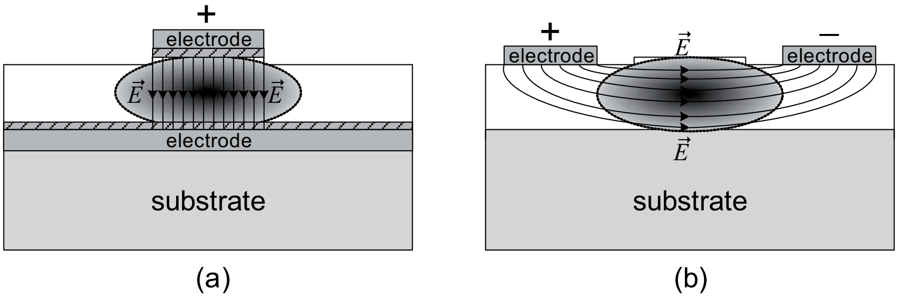

Figure 4.2: Electric field distribution for (a) planar and (b) co-planar electrode geometry. Also shown is the intensity distribution of the fundamental mode propagating in the ridge-type waveguide.

4.2 Photonic crystal slabs

Thin film photonic crystals, also referred to as photonic crystal slabs (PCSs), provide new and unique ways to control and manipulate light. PCSs are 2D periodic dielectric structures of finite thickness, i.e., they do not provide for an omnidirectional photonic band gap, cf. Chapter 1.2. However, from a device application perspective such quasi-2D photonic crystals are attractive, since they may be manufactured using established thin film processing techniques. There are two distinct types of PCSs, i.e., the *rod-type* for which regions of high refractive index are surrounded by regions of low refractive index, and the *hole-type* for which regions of low refractive index are surrounded by regions of high refractive index. Schematics of the rod- and hole-type PCS are shown in Figures 4.3(a) and (b), respectively. The present work addresses the hole-type PCS only.

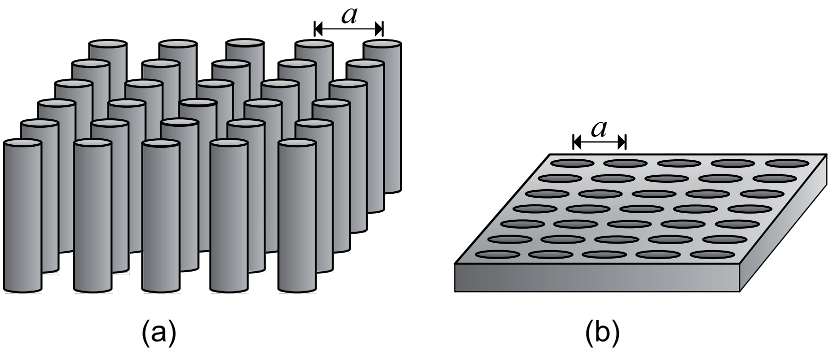

Figure 4.3: Schematic of a (a) rod-type and (b) hole-type photonic crystal slab. The center-to-center separation of nearest-neighbor rods or holes is referred to as the lattice constant, a.

The optical properties of the hole-type PCS are mainly governed by the slab thickness, the dielectric constants of slab and background (i.e., the media surrounding the slab), and the size, shape, and periodic arrangement of the (air) holes. For optical modes to be guided in the PCS, the slab refractive index n must exceed that of the background.

Classification of guided modes

2D photonic crystals are invariant under reflections through the mirror plane bisecting the crystal lattice. This results in formation of linearly polarized optical modes propagating in the mirror plane. Modes with the electric field parallel and the magnetic field perpendicular to the mirror plane are classified as transverse electric (TE), whereas modes with the magnetic field parallel and the electric field perpendicular to the mirror plane are classified as transverse magnetic (TM). PCSs lack translational symmetry in the direction perpendicular to their mirror plane. Hence, the modes are not purely TE or TM polarized. For such quasi-2D photonic crystals, the modes are rather classified as even or odd [3] according to the direction of the electric field vector $\vec{E}$ upon reflection through $z = 0$, as depicted in Figure 4.4. Due to the close resemblance of these modes with the TE and TM modes for genuinely 2D photonic crystals, the lowest order even and odd modes are commonly referred to as TE- and TM-like modes, respectively [4].

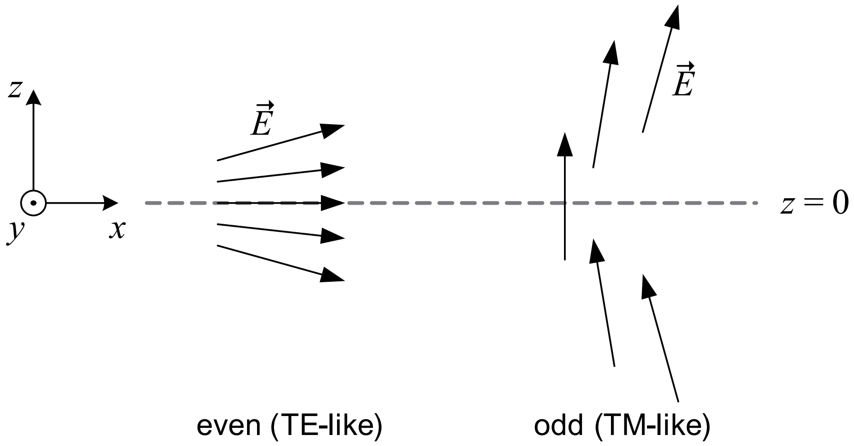

Figure 4.4: For a dielectric slab with a mirror plane at $z = 0$, modes with electric field vectors that are virtually parallel to the mirror plane are labeled even, whereas modes with electric field vectors that are virtually perpendicular to the mirror plane are labeled odd.

The band diagram

The photonic band diagram for a PCS is a two-dimensional plot of eigenfrequencies ω versus wave vector $\vec{k}$. In general, it is not necessary to solve the wave equation (cf. Appendix A) for every $\vec{k}$ in the Brillouin zone, since this equation is invariant under all symmetry operations for the actual 2D periodic lattice (i.e., rotation, inversion, mirror reflection). Thus, the symmetry properties of the photonic crystal is exploited to compute the eigenfrequencies for a limited set of wave vectors $\vec{k}$, i.e., those which are not related by a symmetry operation of the 2D lattice. This region of $\vec{k}$-space is commonly referred to as the *irreducible Brillouin zone*. Figures 4.5(a) and (b) show the first Brillouin zone of a square and hexagonal 2D crystal lattice, respectively. Also shown are the corresponding irreducible Brillouin zones (shaded) with their high-symmetry points, Γ, X, M, and K.

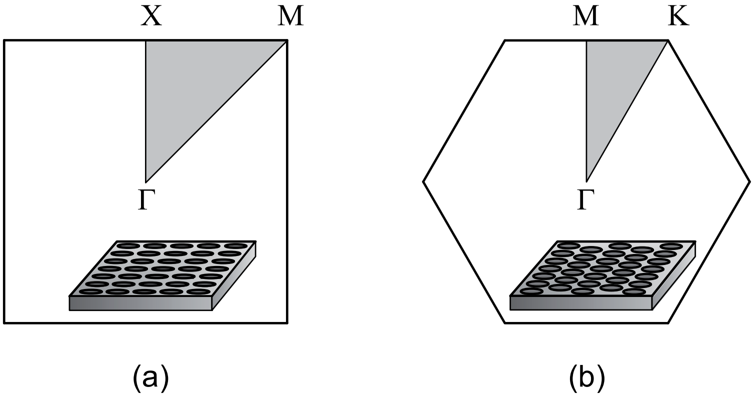

Figure 4.5: The first Brillouin zone of a (a) square and (b) hexagonal 2D crystal lattice, along with the high-symmetry points (Γ, X, M, and K) of the irreducible Brillouin zone (shaded).

A typical band diagram for a hole-type PCS with a hexagonal 2D lattice is shown in Figure 4.6 for normalized frequency units c_0/a, where c_0 is the speed of light in vacuum and a is the lattice constant. The solid line in this diagram depicts the light line, $\omega = c_0\vec{k}$. The continuous region above this line contains all possible frequencies for the slab background. Modes that lie below the light line are guided in the PCS, i.e., they do not couple to the background modes. Hence, the discrete bands are the frequency dispersions of guided modes, which extend infinitely in the plane of the slab and decay exponentially into the background.

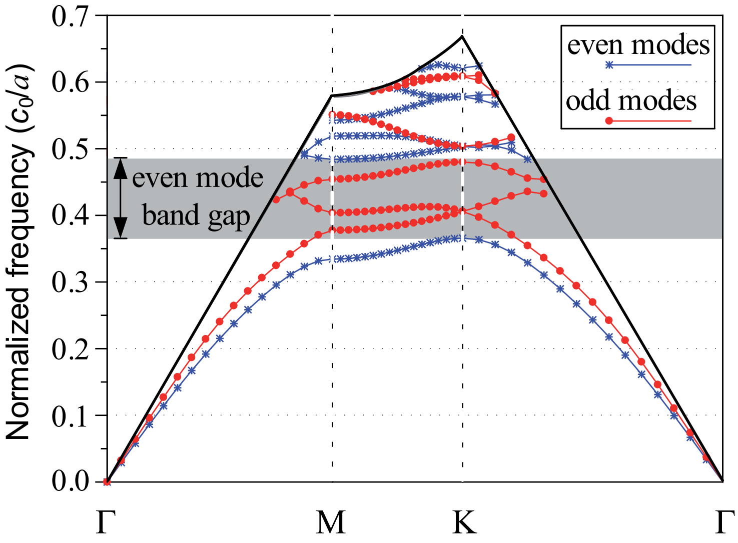

Figure 4.6: Band diagram for a hole-type PCS with a hexagonal 2D lattice of air holes and air background. A slab thickness 0.8a, hole radius 0.38a, and dielectric constant $\varepsilon = 6$ *were used in the calculations for this slab.*

Since radiation modes exist at all frequencies, the band gap of the photonic crystal slab refers to a frequency range in which no *guided modes* exist [4], i.e., the band gap is incomplete and does not include modes above the light line [3]. The diagram in Figure 4.6 shows that the PCS exhibits a band gap for guided even modes (shaded) in the range from 0.37 to $0.48 c_0/a$. There are additional (minor) gaps in this photonic band diagram for both even and odd modes.

4.2.1 Line-defect waveguides

In-plane localization of light in a PCS can be achieved by modifying the 2D lattice to form line-defect waveguides [5], with the potential to guide light around sharp bends with high transmission efficiency [6–12]. Figure 4.7 shows a schematic of line-defect waveguides in a hole-type PCS, formed by removing rows of nearest-neighbor holes from the square and hexagonal 2D lattice. For applications in integrated optics and photonic devices, such line-defect waveguides should ideally meet the following criteria [13]:

- True guided modes are supported by the waveguide.
- The waveguide is single-mode in the relevant frequency range.
- The guided mode lies within the band gap of the PCS.

Conventional waveguides based on total internal reflection can be designed so as to comply with the first two criteria, whereas the third criterium is unique for the line-defect waveguide. Hence, the waveguide modes are localized to the line-defect by the surrounding 2D crystal lattice and do not couple to the guided modes of the PCS, i.e., the waveguide modes are evanescent in the 2D crystal lattice.

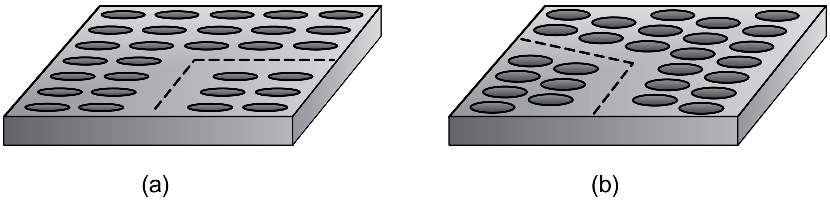

Figure 4.7: Schematic of a hole-type PCS, in which line-defect waveguides (dashed lines) are formed by removing rows of nearest-neighbor holes from the (a) square and (b) hexagonal 2D lattice.

Calculations of the dispersion relation for line-defect waveguides involve projecting the guided modes of the PCS onto the direction of the line-defect [13]. Figure 4.8(a) depicts a line-defect waveguide defined in a hole-type PCS and Figure 4.8(b) shows the hexagonal reciprocal lattice of the PCS. The points denoted m' are the projections of the reciprocal lattice points m onto the Γ−K axis of the photonic crystal reciprocal lattice. The projection of M onto Γ−K is labeled K'. The periodicity a of the line-defect waveguide implies that $|\Gamma$−K'$|= |\Gamma$−M$|\cos 30° = \pi/a$, since by definition $|\Gamma$−M$|= 2\pi/a\sqrt{3}$.

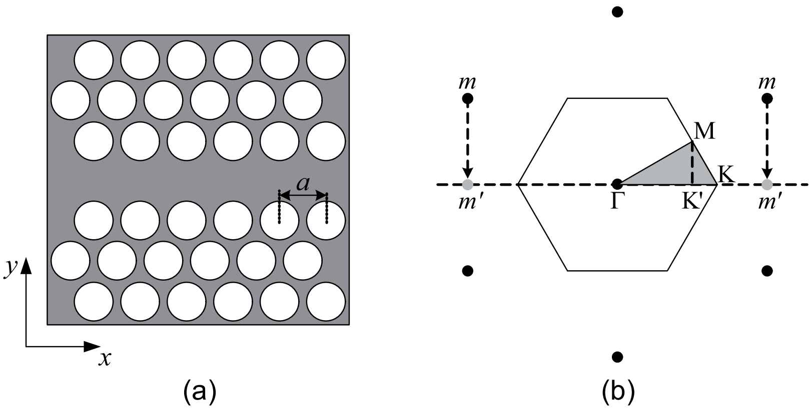

Figure 4.8: (a) Line-defect waveguide in a hole-type PCS. (b) The hexagonal reciprocal lattice of the PCS (black dots) is projected onto the $\Gamma-K$ *axis [13].*

References

[1] Reed, G. T., and Knights, A. P., *Silicon Photonics: An Introduction.* West Sussex, England: Wiley, 2004. pp. 64–71.

[2] Lee, S.-H., Noh, T. W., and Lee, J.-H., “Control of epitaxial growth of pulsed laser deposited $LiNbO_3$ films and their electro-optic effects,” *Appl. Phys. Lett.*, vol. 68, pp. 472–474, 1996.

[3] Joannopoulos, J. D., Johnson, S. G., Winn, J. N., and Meade, R. D., *Photonic Crystals - Molding the Flow of Light.* New Jersey, USA: Princeton University Press, 2nd ed., 2008.

[4] Johnson, S. G., Fan, S., Villeneuve, P. R., Joannopoulos, J. D., and Kolodziejski, L. A., “Guided modes in photonic crystal slabs,” *Phys. Rev. B*, vol. 60, pp. 5751–5758, 1999.

[5] Joannopoulos, J. D., Villeneuve, P. R., and Fan, S., “Photonic crystals: putting a new twist on light,” *Nature*, vol. 386, pp. 143–149, 1997.

[6] Meade, R. D., Devenyi, A., Joannopoulos, J. D., Alerhand, O. L., Smith, D. A., and Kash, K., “Novel applications of photonic band gap materials: Low-loss bends and high Q cavities,” *J. Appl. Phys.*, vol. 75, pp. 4753–4755, 1994.

[7] Mekis, A., Chen, J. C., Kurland, I., Fan, S., Villeneuve, P. R., and Joannopoulos, J. D., “High transmission through sharp bends in photonic crystal waveguides,” *Phys. Rev. Lett.*, vol. 77, pp. 3787–3790, 1996.

[8] Chow, E., Lin, S. Y., Wendt, J. R., Johnson, S. G., and Joannopoulos, J. D., “Quantitative analysis of bending efficiency in photonic-crystal waveguide bends at $\lambda = 1.55$ µm wavelengths,” *Opt. Lett.*, vol. 26, pp. 286–288, 2001.

[9] Benisty, H., Olivier, S., Weisbuch, C., Agio, M., Kafesaki, M., Soukoulis, C. M., Qiu, M., Swillo, M., Karlsson, A., Jaskorzynska, B., Talneau, A., Moosburger, J., Kamp, M., Forchel, A., Ferrini, R., Houdre, R., and Oesterle, U., “Models and measurements for the transmission of submicron-width waveguide bends defined in two-dimensional photonic crystals,” *IEEE J. Quant. Electron.*, vol. 38, pp. 770–785, 2002.

[10] Lin, S. Y., Chow, E., Hietala, V., Villeneuve, P. R., and Joannopoulos, J. D., “Experimental demonstration of guiding and bending of electromagnetic waves in a photonic crystal,” *Science*, vol. 282, pp. 274–276, 1998.

[11] Chutinan, A., and Noda, S., “Waveguides and waveguide bends in two-dimensional photonic crystal slabs,” *Phys. Rev. B*, vol. 62, pp. 4488–4492, 2000.

[12] Li, Z. Y., and Ho, K. M., “Light propagation through photonic crystal waveguide bends by eigenmode examinations,” *Phys. Rev. B*, vol. 68, pp. 045201–1–12, 2003.

[13] Johnson, S. G., Fan, S., Villeneuve, P. R., and Joannopoulos, J. D., “Linear waveguides in photonic-crystal slabs,” *Phys. Rev. B*, vol. 62, pp. 8212–8222, 2000.

Chapter 5

Epitaxial $(Pb,La)(Zr,Ti)O_3$ thin films on buffered Si(001) by on-axis radio frequency magnetron sputtering

NORDSETH, Ø., TYBELL, T., AND GREPSTAD, J. K., *Thin Solid Films*, vol. 517, pp. 2623–2626, 2009.

Abstract: In this study, we discuss the case for integration of epitaxial $(Pb,La)(Zr,Ti)O_3$ (PLZT) thin films with silicon for electro-optic device applications. PLZT films, approximately 500 nm thick, were grown by on-axis radio frequency magnetron sputtering on CeO_2/YSZ-buffered Si(001) substrate with a $SrRuO_3$ electrode layer embedded between CeO_2 and PLZT. The structural properties and surface topography of the different oxide layers were examined with x-ray diffraction analysis and atomic force microscopy. The perovskite thin films were predominantly (001)-oriented, with a (002) rocking curve halfwidth of approximately 0.3° and a surface roughness compatible with requirements for application in optical devices. The PLZT cation stoichiometry was assessed from quantitative x-ray photoelectron spectroscopy. These measurements uncovered a

substantial depletion of lead in the film surface for layers deposited at substrate temperatures above ~600°C, whereas the surface concentration of La, Zr, and Ti remained virtually unaffected over a wide range of growth temperatures.

5.1 Introduction

In order to meet the increasing demand for high performance, low-cost integrated circuits in optical communication systems, introduction of novel materials with versatile functional properties is being explored [1–6]. The perovskite oxide (Pb,La)(Zr,Ti)O_3 (PLZT) offers several functional properties attractive to optical device applications, such as a large electro-optic coefficient and high transparency at optical frequencies [7]. The electro-optic properties of PLZT are mainly governed by the chemical composition. The PLZT target used in the present study was $(\mathrm{Pb}_{1-x},\mathrm{La}_x)(\mathrm{Zr}_y,\mathrm{Ti}_{1-y})\mathrm{O}_3$, with $x = 0.08$ and $y = 0.4$, which exhibits tetragonal ferroelectric phase at room temperature and linear (Pockels) electro-optic characteristics [8]. This composition renders hysteresis loops of high coercivity and linear electro-optic response for applied fields below the coercive field. Such characteristics near zero applied field are considered attractive for optical devices operating without a biasing field, such as light modulators.

The properties of ferroelectric perovskite thin films are strongly dependent on the crystalline structure. In order to facilitate epitaxial growth of PLZT on Si(001), a buffer layer structure of CeO_2 and yttria-stabilized zirconia (YSZ) is commonly adopted [9–11]. Moreover, to add functionality to this thin film stack, a layer of $SrRuO_3$ is interposed between CeO_2 and PLZT [12]. The metallic properties of $SrRuO_3$ provide an electrode for subsequent polarization of the PLZT film. The perovskite structure of $SrRuO_3$ ensures an epitaxial relationship between this layer and PLZT.

For applications of PLZT in optical devices, it is essential that highly crystalline and uniform films can be prepared with sufficient thickness to support propagation of optical modes. A number of deposition techniques were adopted to this end, such as chemical solution processing [13], pulsed laser ablation [14], metal-organic chemical vapor deposition [15], ion beam sputtering [16], magnetron sputtering [17], spin-coating pyrolysis [18], and sol-gel processing [19]. In the present communication, we report on deposition of epitaxial (Pb,La)(Zr,Ti)O_3 thin films on buffered Si(001) using radio frequency (RF) magnetron sputtering. An on-axis target geometry was adopted in order to attain high deposition rates, compared to that for films deposited by off-axis sputtering in a preceding growth effort [20]. Deposition of homogeneous films with several hundred nanometer thickness, required for application in integrated optics, is demonstrated. Moreover, it is shown that the cation stoichiometry of such films, notably their lead content, depends critically on the substrate temperature during growth.

5.2 Experimental

Buffer layers of YSZ (13 mol% Y_2O_3) and CeO_2 were initially deposited on n-type Si(001) wafers (Siltronix) by electron beam evaporation. The silicon wafers were single-side polished, with a thickness of 350 µm and resistivity 2–20 Ω·cm. A 200 nm thick titanium layer was predeposited on the reverse of the polished silicon wafers to allow for radiative heating of the substrate during oxide film growth. The wafers were cut in 20×20 mm^2 dies, which were cleaned ultrasonically in acetone and subsequently rinsed with isopropanol. The substrates were heated in high vacuum at 800°C in a multi-target e-beam evaporation chamber. YSZ and CeO_2 buffer layers were grown on the polished Si(001) surface at a partial oxygen pressure of 1×10^{-4} mbar, without removing the native oxide and without breaking the vacuum between deposition of the two oxide layers. The introduction of oxygen in the evaporation chamber at the initial stage of YSZ deposition was delayed by $\sim$30 s, in order to allow for dissociated Zr ions to reduce the native surface SiO_x layer [21, 22]. The growth rate was approximately 0.3 nm/s for both layers, with typical thicknesses of 40 and 10 nm for CeO_2 and YSZ, respectively. These CeO_2/YSZ-buffered Si(001) substrates were then subdivided into 5×5 mm^2 dies and rinsed in acetone and isopropanol.

PLZT and $SrRuO_3$ thin films were deposited on the buffered Si(001) substrates by on-axis and off-axis RF magnetron sputtering, respectively. For epitaxial growth of PLZT the buffered substrates were radiatively heated to temperatures in the range 500–750°C, as measured with an optical pyrometer. The films were grown in a mixed atmosphere of oxygen and argon (O_2/Ar = 4:10) at a total pressure of 100 mTorr. The separation between the 3-inch $Pb_{1.104}La_{0.08}Zr_{0.4}Ti_{0.6}O_3$ target (Praxair Surface Technologies) and the substrate was 48 mm, with a corresponding deposition rate of approximately 2.5 nm/min. The PLZT target contained 20 mol% excess lead, to compensate for non-stoichiometric transfer of lead in the sputter deposition process. The $SrRuO_3$ layer was deposited at a substrate temperature of approximately 810°C, a total pressure of 175 mTorr, and an O_2/Ar ratio of 4:9. The PLZT films were grown both directly on CeO_2/YSZ-buffered Si(001) and with $SrRuO_3$ embedded in the multilayer stack. The growth conditions for PLZT were the same in both cases.

X-ray diffraction (XRD) measurements were performed in order to establish the phase and crystalline orientation of the different layers, using a Bruker D8 Discover x-ray diffractometer. The topography of the film surface was examined by tapping mode atomic force microscopy (AFM), using a Veeco MultiMode V scanning probe microscope. In order to determine the elemental composition of the PLZT films, quantitative x-ray photoelectron spectroscopy (XPS) analysis was carried out using a VG Escalab MkII system equipped with an Al/Mg twin anode and a hemispherical electron energy analyzer. The electron scattering length in these measurements renders a sampling depth of 2.0±0.5 nm for this material [23]. The recorded peak energies were corrected for electrostatic sample charging by assigning a C1s core level binding energy of 285.0 eV to emission from adventitious surface carbon.

5.3 Results and discussion

Figure 5.1 shows θ-2θ x-ray diffractograms for PLZT thin films grown on buffered Si(001), with and without a $SrRuO_3$ electrode layer. The scan in Figure 5.1(a) pertains to a 150 nm thick film grown on CeO_2/YSZ-buffered Si(001) at a substrate temperature of 670°C. This diffractogram shows that the e-beam deposited CeO_2 and YSZ buffer layers grow with (001) crystalline orientation, which is also the predominant orientation of PLZT. The PLZT(002) diffraction peak at $2\theta = 44.4^\circ$ corresponds to a c-axis lattice parameter 4.077 Å, close to the reported bulk value of 4.074 Å for $Pb_{0.92}La_{0.08}Zr_{0.4}Ti_{0.6}O_3$ [7], which indicates that the (001)-oriented PLZT film is relaxed. The diffractogram also reveals formation of minor domains with different crystalline orientation (cf. the PLZT(111) diffraction peak in Figure 5.1(a)), which serve to accommodate the large lattice mismatch ($>$ 5 %) between the PLZT and CeO_2 unit cells.

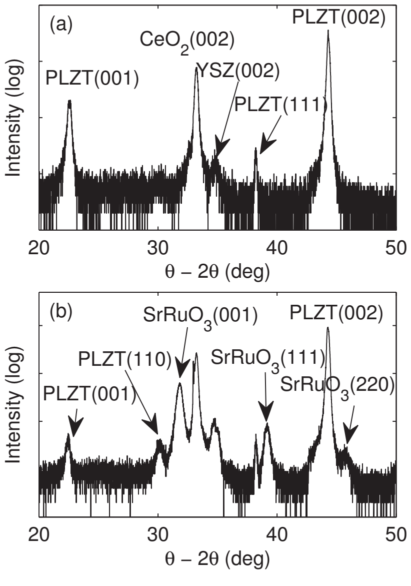

Figure 5.1: θ-2θ x-ray diffractograms of PLZT thin films grown on (a) CeO_2/YSZ/Si(001) and (b) $SrRuO_3$/CeO_2/YSZ/Si(001). The PLZT layer shows predominant (001) orientation in both cases.

Figure 5.1(b) shows the θ-2θ scan for PLZT grown on buffered Si(001) with a 20 nm $SrRuO_3$ electrode layer. This data unveils formation of more than one crystalline orientation for both PLZT and $SrRuO_3$. However, the PLZT film remains predominantly (001)-oriented. We find that a pyrochlore phase of PLZT prevails for films grown at substrate temperatures below 520°C, as previously observed for sputter-deposited thin films on $SrTiO_3$(001) [20]. The presence of pyrochlore has been reported to degrade the dielectric and optical properties of PLZT thin films [24].

Rocking curves recorded for the leading diffraction peaks of each layer in the PLZT/$SrRuO_3$/CeO_2/YSZ thin film heterostructure are shown in Figure 5.2. The rocking curves for CeO_2(002) and YSZ(002) demonstrate good crystalline quality for these e-beam deposited buffer layers, with a full width at half maximum (FWHM) of approximately 1°, in close correspondence with rocking curves previously reported for such layers [25, 26]. The FWHM of the SRO(001) rocking curve was measured at ~1.3°, and the rocking curve FWHM of the PLZT(002) and the PLZT(110) diffraction peaks were measured at

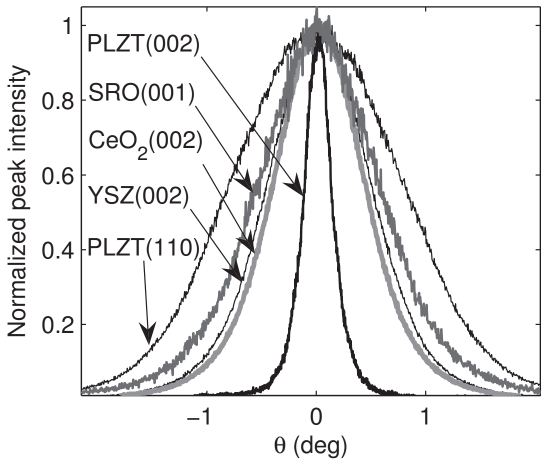

Figure 5.2: Rocking curves recorded for the leading diffraction peaks of the different layers in the PLZT/$SrRuO_3$/CeO_2/YSZ thin film stack.

0.3° and 1.7°, respectively. Thus, the PLZT films grown on buffered Si(001) exhibit good crystalline quality for the (001)-oriented phase, with noticeably poorer quality for (110)-oriented domains. The crystalline quality of the 001-oriented PLZT is comparable to that reported for films grown by sputter deposition on $SrTiO_3$(001) [20]. The narrower rocking curve for the PLZT(002) compared to that of the buffer layers may be attributed to the much larger thickness of the PLZT layer. The PLZT(002) rocking curve FWHM is observed to decrease with increasing thickness of the PLZT layer, due to strain relaxation. We note that the FWHM of the PLZT(002) rocking curve is not appreciably affected by introduction of a $SrRuO_3$ electrode layer in the multilayer thin film stack.

Figure 5.3(a) shows φ-scans of a PLZT thin film grown directly on CeO_2/YSZ-buffered Si(001). The fourfold rotational symmetry shows that the perovskite unit cell of PLZT is rotated 45° with respect to the CeO_2 lattice. This implies in-plane epitaxial alignment of PLZT[100] with CeO_2[110], as depicted in the sketch in Figure 5.3(b). The φ-scans also show that the YSZ(111) reflections coincide with the corresponding reflections of the silicon substrate, which implies that the YSZ layer grows cube-on-cube with Si(001).

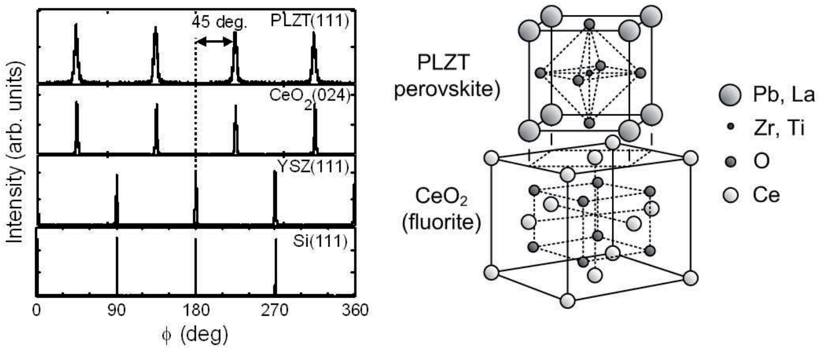

(a) (b)

Figure 5.3: (a) φ-scan diffractograms of a PLZT film grown on CeO_2/YSZ-buffered Si(001). (b) The perovskite unit cell of PLZT is rotated 45° with respect to the unit cell of CeO_2.

Such growth is also observed for the CeO_2 layer, in agreement with the lattice alignment reported by Méchin *et al.* [26] and by Kondo *et al.* [27]. These φ-scans and the θ-2θ scans in Figure 5.1 demonstrate that the PLZT films are highly oriented with a distinct in-plane alignment, and moreover, that (001)-oriented YSZ can be grown epitaxially on Si(001) without stripping the substrate of its native surface oxide prior to growth [21, 28].

Figure 5.4 shows a reciprocal space map (RSM) of the CeO_2/YSZ-buffered Si(001) substrate. The RSM reveals that the YSZ(113) reflection is shifted relative to that of Si(113) by $\Delta h = 0.06$, which implies relaxed growth of YSZ. Furthermore, the shift of the CeO_2(113) reflection relative to that of YSZ(113) implies relaxed growth of CeO_2 on YSZ. These findings suggest that the buffer layers grow cube-on-cube on Si(001).

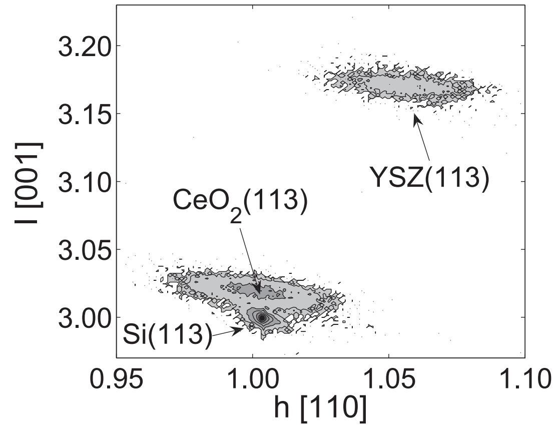

Figure 5.4: Reciprocal space map for the (113) lattice planes of the CeO_2/YSZ-buffered Si(001) substrate.

Figure 5.5 displays typical 1×1 µm^2 AFM scans of (a) the buffered Si(001) substrate and (b) a PLZT film grown on CeO_2/YSZ/Si(001). The CeO_2 surface appears smooth, with no pronounced texture and a measured root mean square (RMS) surface roughness of ~1 nm. By comparison, the RMS roughness of the polished substrate surface was measured at ~1.5 Å for a 1×1 µm^2 scan.

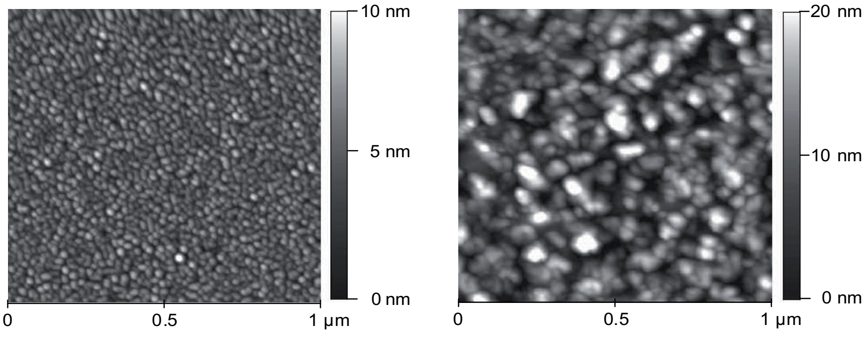

(a) (b)

Figure 5.5: $1\times1\ \mu m^2$ *AFM scans of (a) the e-beam evaporated* CeO_2/YSZ *buffer layer on Si(001) and (b) the* $PLZT/SrRuO_3/CeO_2/YSZ/Si(001)$ *multilayer stack, with a corresponding RMS surface roughness of 1.0 nm and 4.1 nm, respectively.*

The RMS roughness of the PLZT film surface in Figure 5.5(b) was measured at approximately 4.1 nm. This is close to the presumed upper bound on the surface roughness for propagation of light in such films with moderate optical scattering [29, 30], a prerequisite for their use in optical waveguide applications. The RMS roughness of the PLZT film surface was found to increase with the film thickness, e.g., the RMS surface roughness of a PLZT film with thickness 150 nm was measured at ~1.8 nm. The PLZT film surface appears dense and uniform with no visible voids or cracks, as measured with scanning electron microscopy (SEM).

Numerical simulation of light propagation in the $PLZT/SrRuO_3/CeO_2/YSZ/Si(001)$ heterostructure suggests that increasing the thickness of the dielectric buffer layers will substantially improve the confinement of horizontally propagating light to the PLZT layer [data not shown]. CeO_2 and YSZ both have a lower refractive index than PLZT, and these layers will reduce optical absorption in the semiconductor substrate if sufficiently thick. AFM analysis shows that increasing the CeO_2 layer thickness to 500 nm does not significantly affect the surface roughness of the PLZT film.

XPS data taken on the PLZT films uncovers no surface contamination beyond the presence of adventitious surface carbon. The measured Pb $4f_{7/2}$ (138.0 eV), La $3d_{5/2}$ (834.7 eV), Zr $3d_{5/2}$ (181.2 eV), and Ti $2p_{3/2}$ (458.1 eV) binding energies are in close agreement with the values previously reported for PLZT [20] and PZT [31, 32]. The recorded core level spectra suggest a single oxidation state for the PLZT cations. The La 3d spectrum shown in Figure 5.6 displays a multiplet structure with two distinct peaks characteristic of an $a_1|3d^{-1}4f^0\rangle + a_2|3d^{-1}4f^1\underline{L}\rangle$ final state of photoemission, where $\underline{L}$ denotes a hole in a ligand O 2p orbital from charge transfer to the La 4f shell [33, 34].

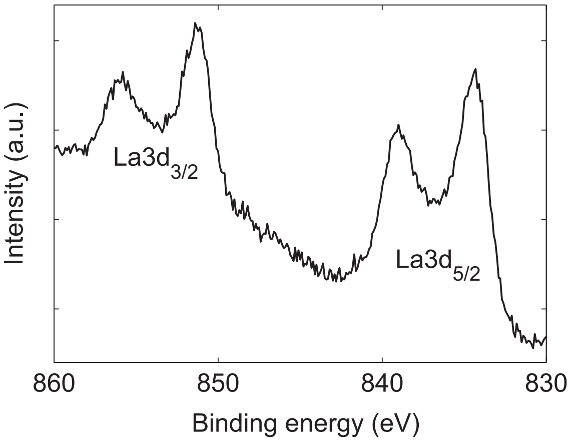

Figure 5.6: La 3d XPS core level spectrum of the PLZT thin film surface.

Figure 5.7 shows the surface cation stoichiometry of sputter-deposited PLZT films vs. substrate temperature during growth, as obtained from XPS analysis. The core level peak intensities were estimated from least-squares fits of Voigt lineshapes to the recorded spectra, after subtraction of a Shirley background [35]. Empirical atomic sensitivity factors [36] were used to obtain the relative cation concentrations. The plot in Figure 5.7 reveals a substantial decrease in the (Pb+La):(Zr+Ti) ratio with increasing substrate temperature from 500°C to 750°C, while the La:(Zr+Ti) ratio remains fixed at approximately 0.1.

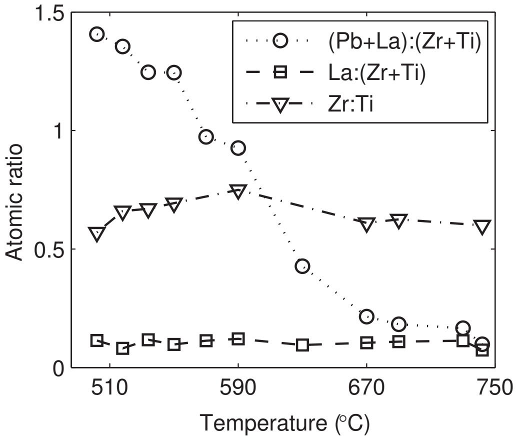

Figure 5.7: Surface cation stoichiometry of PLZT films grown on CeO_2/YSZ-buffered Si(001) as a function of substrate temperature during growth.

The loss of Pb in the film surface at high growth temperatures can be attributed to a high volatility of the Pb ions. As a result, the perovskite stoichiometry of PLZT is not preserved, which may lead to films with degraded dielectric and ferroelectric properties [37]. The target used in this experiment had 20 mol% excess Pb to compensate for the loss of Pb during growth. The XPS analysis suggests that this is not sufficient to prevent growth of Pb-depleted films for substrate temperatures above ∼630°C. The lanthanum content of the PLZT films is important both to their optical transparency and dielectric response. The optical transparency of PLZT is reported to deteriorate for material with less than 8 at.% La [7]. The measured XPS intensities (cf. Figure 5.7) indicate that this should be of no concern for films grown at substrate temperatures between 500°C and 750°C. Moreover, the Zr:Ti ratio is found to remain fixed at approximately 40:60 for this entire temperature range, in close agreement with the target stoichiometry. The (Pb+La):(Zr+Ti) atomic ratio for PLZT films grown at higher chamber pressures (up to 150 mTorr) was also analyzed with XPS. The measurements indicate that the recorded loss of Pb is slightly diminished by increasing the oxygen partial pressure during deposition.

5.4 Conclusions

Epitaxial PLZT thin films were grown on CeO_2/YSZ-buffered Si(001) substrate by on-axis RF magnetron sputtering. The films are preferentially (001)-oriented with a rocking curve FWHM of approximately 0.3° for the PLZT(002) diffraction peak. φ-scans show that the unit cell of PLZT is rotated 45° with respect to that of CeO_2, confirming an epitaxial relationship. Films of several hundred nanometer thickness exhibit smooth surfaces, with an RMS surface roughness of ∼4 nm. The crystalline quality and surface roughness is deemed sufficient for application of such films in electro-optic and photonic devices. Quantitative XPS analysis reveals a substantial loss of Pb in the film surface and thus, a deviation from the perovskite cation stoichiometry, with increasing substrate growth temperature. In contrast, the surface concentrations of La, Zr, and Ti remain constant throughout the investigated temperature range, which holds good promise for growth of thin films with the desired dielectric response and electro-optic properties.

References

[1] Haertling, G. H., “PLZT electrooptic materials and applications – a review,” *Ferroelectrics*, vol. 75, pp. 25–55, 1987.

[2] Scott, J. F., “Applications of modern ferroelectrics,” *Science*, vol. 315, pp. 954–959, 2007.

[3] Ramesh, R., Gilchrist, H., Sands, T., Keramidas, V. G., Haakenaasen, R., and Fork, D. K., “Ferroelectric La-Sr-Co-O/Pb-Zr-Ti-O/La-Sr-Co-O heterostructures on silicon via template growth,” *Appl. Phys. Lett.*, vol. 63, pp. 3592–3594, 1993.

[4] Ghonge, S. G., Goo, E., Ramesh, R., Haakenaasen, R., and Fork, D. K., “Microstructure of epitaxial oxide thin film heterostructures on silicon by pulsed laser deposition,” *Appl. Phys. Lett.*, vol. 64, pp. 3407–3409, 1994.

[5] Kondo, M., Sato, K., Ishii, M., Wakiya, N., Shinozaki, K., and Kurihara, K., “Electrooptic properties of lead zirconate titanate films prepared on silicon substrate,” *Jpn. J. Appl. Phys.*, vol. 45, pp. 7516–7519, 2006.

[6] Nordseth, Ø., Tybell, T., and Grepstad, J. K., “Simulation of photonic band gap waveguides in lead-lanthanum zirconate-titanate, in: 2006 Northern Optics Conference Proceedings,” pp. 51–54, 2006.

[7] Haertling, G. H., and Land, C. E., “Hot pressed (Pb,La)(Zr,Ti)O_3 ferroelectric ceramics for electrooptic applications,” *J. Am. Ceram. Soc.*, vol. 54, pp. 1–11, 1971.

[8] Hardtl, K. H., and Hennings, D., “Distribution of A-site and B-site vacancies in (Pb,La)(Ti,Zr)O_3 ceramics,” *J. Am. Ceram. Soc.*, vol. 55, pp. 230–231, 1972.

[9] Copetti, C. A., Soltner, H., Schubert, J., Zander, W., Hollricher, O., Buchal, C., Schulz, H., Tellmann, N., and Klein, N., “High quality epitaxy of $YBa_2Cu_3O_{7-x}$ on silicon-on-sapphire with the multiple buffer layer YSZ/CeO_2,” *Appl. Phys. Lett.*, vol. 63, pp. 1429–1431, 1993.

[10] Yamada, T., Wakiya, N., Shinozaki, K., and Mizutani, N., “Epitaxial growth of $SrTiO_3$ films on CeO_2/yttria-stabilized zirconia/Si(001) with TiO_2 atomic layer by pulsed-laser deposition,” *Appl. Phys. Lett.*, vol. 83, pp. 4815–4817, 2003.

[11] Wakiya, N., Yamada, T., Shinozaki, K., and Mizutani, N., “Heteroepitaxial growth of CeO_2 thin film on Si(001) with an ultra thin YSZ buffer layer,” *Thin Solid Films*, vol. 371, pp. 211–217, 2000.

[12] Suzuki, M., and Ami, T., “A proposal of epitaxial oxide thin film structures for future oxide electronics,” *Mater. Sci. Eng. B*, vol. 41, pp. 166–173, 1996.

[13] Moon, S., Kwak, M., Kim, Y. T., Ryu, H. C., Lee, S. J., and Kang, K. Y., “Microwave dielectric properties for

(Pb,La)(Zr,Ti)O_3 thin films on MgO(001) substrate grown by chemical solution deposition," *Int. Ferroelectr.*, vol. 77, pp. 37–44, 2005.

[14] Cheng, H. F., "Spectroscopic characteristics of $Pb_{0.95}La_{0.05}(Zr_{1-y}Ti_y)_{0.9875}O_3$ plasma and growth behavior of thin films by pulsed laser deposition," *J. Appl. Phys.*, vol. 78, pp. 4633–4639, 2005.

[15] Okada, M., and Tominaga, K., "Preparation and properties of (Pb,La)(Zr,Ti)O_3 thin films by metalorganic chemical vapor deposition," *J. Appl. Phys.*, vol. 71, pp. 1955–1959, 1992.

[16] Boyer, L. L., Wu, A. Y., Metzger, G. W., and Mcneil, J. R., "Properties of ion beam deposited $Pb_{1-x}La_x(Zr_yTi_z)_{1-x/4}O_3$," *J. Vac. Sci. Technol. A*, vol. 7, pp. 1199–1201, 1989.

[17] Ramakrishnan, E. S., and Howng, W. Y., "Ferroelectric lead zirconate titanate thin films by radio frequency magnetron sputtering," *J. Vac. Sci. Technol. A*, vol. 10, pp. 69–74, 1992.

[18] Cross, J. S., Tomotani, M., and Kotaka, Y., "(Pb,La)(Zr,Ti)O_3 film grain-boundary conduction with $SrRuO_3$ top electrodes," *Jpn. J. Appl. Phys.*, vol. 40, pp. L346–L348, 2001.

[19] Yoon, D. S., Kim, C. J., Lee, J. S., Lee, W. J., and No, K., "Epitaxial growth of sol-gel PLZT thin films," *J. Mater. Res.*, vol. 9, pp. 420–425, 1994.

[20] Kumar, A. K. S., Dahl, Ø., Pettersen, S. V., Grepstad, J. K., and Tybell, T., "Characterization of crystalline $Pb_{0.92}La_{0.08}Zr_{0.4}Ti_{0.6}O_3$ thin films grown by off-axis radio frequency magnetron sputtering," *Thin Solid Films*, vol. 492, pp. 71–74, 2005.

[21] Hirai, T., Teramoto, K., Koike, H., Nagashima, K., and Tarui, Y., "Initial stage and growth process of ceria, yttria-stabilized-zirconia and ceria-zirconia mixture thin films

on Si(100) surfaces," *Jpn. J. Appl. Phys.*, vol. 36, pp. 5253–5258, 1997.

[22] Wang, S. J., Ong, C. K., You, L. P., and Xu, S. Y., "Epitaxial growth of yttria-stabilized zirconia oxide thin film on natively oxidized silicon wafer without an amorphous layer," *Semicond. Sci. Technol.*, vol. 15, pp. 836–839, 2000.

[23] Lindau, I., and Spicer, W. E., "The probing depth in photoemission and auger-electron spectroscopy," *J. Electron Spectrosc.*, vol. 3, pp. 409–413, 1974.

[24] Nakagawa, T., Yamaguchi, J., Usuki, T., Matsui, Y., Okuyama, M., and Hamakawa, Y., "Ferroelectric properties of rf sputtered PLZT thin film," *Jpn. J. Appl. Phys.*, vol. 18, pp. 897–902, 1979.

[25] Fork, D. K., Fenner, D. B., Connell, G. A. N., Philips, J. M., and Geballe, T. H., "Epitaxial yttria-stabilized zirconia on hydrogen-terminated Si by pulsed laser deposition," *Appl. Phys. Lett.*, vol. 57, pp. 1137–1139, 1990.

[26] Méchin, L., Villégier, J.-C., Rolland, G., and Laugier, F., "Double CeO_2/YSZ buffer layer for the epitaxial growth of $YBa_2Cu_3O_{7-\delta}$ films on Si(001) substrates," *Physica C*, vol. 269, pp. 124–130, 1996.

[27] Kondo, M., Maruyama, K., and Kurihara, K., "Epitaxial ferroelectric thin films on silicon substrates for future electronic devices," *Fujitsu Sci. Tech. J.*, vol. 38, pp. 46–53, 2002.

[28] Bardal, A., Matthee, T., Wecker, J., and Samwer, K., "Initial stages of epitaxial growth of Y-stabilized ZrO_2 thin films on a-SiO_x/Si(001) substrates," *J. Appl. Phys.*, vol. 75, pp. 2902–2910, 1994.

[29] Wessels, B. W., Nystrom, M. J., Chen, J., Studebaker, D., and Marks, T. J., "Epitaxial niobate thin films and their nonlinear optical properties," *Mater. Res. Soc. Symp. Proc.*, vol. 401, pp. 211–218, 1996.

[30] Leng, W. J., Yang, C. R., Ji, H., Zhang, J. H., Chen, H. W., and Tang, J. L., "Structure-related optical properties of (Pb,La)(Zr,Ti)O_3 thin films on indium tin oxide/quartz substrates," *J. Appl. Phys.*, vol. 100, p. 083505, 2006.

[31] Wakiya, N., Kuroyanagi, K., Xuan, Y., Shinozaki, K., and Mizutani, N., "An XPS study of the nucleation and growth behavior of an epitaxial Pb(Zr,Ti)O_3/MgO(100) thin film prepared by MOCVD," *Thin Solid Films*, vol. 372, pp. 156–162, 2000.

[32] Kim, J.-N., Shin, K.-S., Kim, D.-H., Park, B.-O., Kim, N.-K., and Cho, S.-H., "Changes in chemical behavior of thin film lead zirconate titanate during Ar^+-ion bombardment using XPS," *Appl. Surf. Sci.*, vol. 206, pp. 119–128, 2003.

[33] Suzuki, C., Kawai, J., Takahashi, M., Vlaicu, A. M., Adachi, H., and Mukoyama, T., "The electronic structure of rare-earth oxides in the creation of the core hole," *Chem. Phys.*, vol. 253, pp. 27–40, 2000.

[34] Honma, T., Benino, Y., Fujiwara, T., Komatsu, T., Sato, R., and Dimitrov, V., "Electronic polarizability, optical basicity, and interaction parameter of La_2O_3 and related glasses," *J. Appl. Phys.*, vol. 91, pp. 2942–2950, 2002.

[35] Shirley, D. A., "High-resolution x-ray photoemission spectrum of the valence bands of gold," *Phys. Rev. B*, vol. 5, pp. 4709–4714, 1972.

[36] Wagner, C. D., Davis, L. E., Zeller, M. V., Taylor, J. A., Raymond, R. H., and Gale, L. H., "Empirical atomic sensitivity factors for quantitative analysis by electron spectroscopy for chemical analysis," *Surf. Interface Anal.*, vol. 3, pp. 211–225, 1981.

[37] Lefevre, M. J., Speck, J. S., Schwartz, R. W., Dimos, D., and Lockwood, S. J., "Microstructural development in sol-gel derived lead zirconate titanate thin films: The role of

precursor stoichiometry and processing environment,” *J. Mater. Res.*, vol. 11, pp. 2076–2084, 1996.

Chapter 6

Sputter-deposited (Pb,La)(Zr,Ti)O_3 thin films: Effect of substrate and optical properties

Nordseth, Ø., Røyset, A., Tybell, T., and Grepstad, J. K., *J. Vac. Sci. Technol. A*, vol. 27, pp. 548–553, 2009.

Abstract: Optically transparent (Pb,La)(Zr,Ti)O_3 (PLZT) thin films were sputter-deposited on $SrTiO_3(001)$ and MgO(001) substrates with a $SrRuO_3(110)$ bottom electrode. X-ray diffraction analysis showed epitaxial growth of monocrystalline PLZT, with (001) rocking curve full width at half maxima of ∼0.03° and ∼0.3° for films deposited on $SrTiO_3$ and MgO, respectively. In-plane epitaxial alignment of the $SrRuO_3$ and PLZT epilayers was verified from φ-scans. It was established from atomic force microscopy measurements that the PLZT surface roughness meets the requirement for optical waveguide applications. Recorded P-E loops for films grown on both substrates showed a remanent polarization of ∼36 $\mu C/cm^2$. The refractive index of the PLZT layer was estimated from rutile prism coupling measurements at ∼2.56 for $\lambda = 633$ nm, consistent with data obtained by spectroscopic ellipsometry. The ferroelectric and optical characteristics of the films, as well as their surface rough-

ness, were not appreciably different for the two substrates. This makes MgO the preferred choice of substrate for optical waveguide devices due to its low refractive index compared to that of $SrTiO_3$.

6.1 Introduction

The large family of perovskite oxides offers a rich variety of functional properties [1], such as pyro-, piezo-, and ferroelectricity, ferro- and antiferromagnetism, and electro-optic effect, which render these materials attractive for a wide range of device applications [2–4]. These include nonvolatile memory, ferroelectric field effect transistors, transducers, and sensors [5, 6]. The transparent perovskite $(Pb,La)(Zr,Ti)O_3$ (PLZT) is recognized as a useful material for optical device applications, mainly by virtue of its low propagation losses at visible and near infrared wavelengths combined with a strong electro-optic response [7]. The addition of lanthanum to $Pb(Zr,Ti)O_3$ diminishes the optical anisotropy in the material [8], resulting in substantially reduced light scattering for a La content in excess of 6 at.% [9]. The electro-optic characteristics of PLZT depend on the cation stoichiometry and may be classified as "linear", "quadratic", or "memory" according to the ferroelectric hysteresis behavior [10, 11]. In this work, PLZT with 8 % La substitution for Pb and a Zr:Ti cation ratio of 40:60 were chosen in order to obtain a linear electro-optic response (i.e., Pockels effect). A linear relation between refractive index and applied field is a prerequisite for electro-optic devices such as modulators and switches [12].

The application of thin films in integrated optics places strict requirements on homogeneity and film thickness, as well as on surface morphology, to prevent losses from optical scattering [13]. Moreover, the electro-optic properties of thin films will be affected by the crystalline quality and orientation, residual stresses, grain boundaries, and the film-electrode interfaces [14]. In this study, we discuss epitaxial growth of PLZT/$SrRuO_3$ (SRO) bilayers on $SrTiO_3$(001) and MgO(001) substrates using radio frequency (RF) magnetron sputtering. The thin SRO epilayer, grown prior to PLZT, was introduced to serve as bottom electrode for subsequent dielectric and ferroelectric measurements [15]. This planar electrode geometry renders a high electric field in the PLZT layer compatible with low-voltage operation, advantageous to electro-optic modulation. The $SrTiO_3$ substrate offers good lattice match with a wide selection of perovskite oxides. However, the relatively high refractive index of $SrTiO_3$ (n = 2.38) restricts the use of this substrate in thin film waveguide devices. MgO on the other hand has a low refractive index of $n = 1.74$, a prerequisite for strong optical mode confinement in the PLZT active layer. The MgO substrate has a larger lattice mismatch with PLZT, however, which tends to complicate epitaxial growth. This paper analyzes and compares the crystalline, ferroelectric, dielectric, and optical properties of $Pb_{0.92}La_{0.08}Zr_{0.4}Ti_{0.6}O_3$ thin films grown on these two substrates.

6.2 Experimental

6.2.1 Thin film growth

Polished, (001)-oriented crystalline wafers of $SrTiO_3$ (Shinkosha Co., Ltd.) and MgO (MTI Crystal) were cut in 5×5 mm^2 dies, cleaned ultrasonically in acetone, and subsequently rinsed with isopropyl alcohol. The substrates were fixed to a 2 in. diameter Inconel sample holder by silver paste, before introduction in the sputter chamber (Kurt J. Lesker Co.), equipped with Torus magnetron cathodes. The substrates were radiatively heated *in situ*, and their surface temperature was measured using an optical pyrometer with the emissivity set at 0.7. The vacuum chamber base pressure was 5×10^{-8} Torr. The overall gas pressure was controlled with a manually operated gate valve, and the flow of Ar and O_2 (both of 99.9999% purity) was regulated by mass-flow controllers. The SRO and PLZT targets were both 3 in. diameter (Praxair, 99.9% purity), solder bonded to a copper alloy backing plate. The RF (13.56 MHz) power was 90 W for deposition of PLZT and 100 W for SRO.

The SRO epilayers were deposited in a 90° off-axis sputter geometry [16], with a target center to substrate separation of $\sim$100 mm. The layers were grown in a mixed ambient of O_2:Ar = 4:10 at a total pressure in the growth chamber of 100 mTorr. The substrate temperature was ∼630°C. The typical thickness of the SRO electrode layer was 20 nm, as determined from x-ray reflectivity measurements [17], and the deposition rate was approximately 0.4 nm/min. Prior to deposition of PLZT, the substrate temperature was lowered and stabilized within the range 490–570°C, without breaking the vacuum. In order to achieve sufficient growth rates of films suitable for optical waveguide applications, i.e., with a typical thickness of 0.5 µm or more, the PLZT epilayers were deposited in a planar sputter geometry. The composition of the PLZT target was $Pb_{1.104}La_{0.08}Zr_{0.4}Ti_{0.6}O_3$, i.e., with 20 mol% excess lead to compensate for a disproportionate loss of lead from the film surface during deposition. The gun holding the PLZT target was mounted on a linear translator in order to allow for multilayer deposition. Optimum growth conditions for PLZT were established for a target-to-substrate separation of 48 mm. The films were grown in a mixed ambient of O_2:Ar = 4:10 at total pressures of 100 mTorr and 165 mTorr for deposition on $SrTiO_3$(001) and MgO(001), respectively. The deposition rate under these conditions was approximately 2.5 nm/min. The samples were allowed to cool to room temperature in their growth ambient before being removed from the growth chamber.

6.2.2 Materials characterization

X-ray diffraction (XRD) measurements were carried out on a Bruker D8 Discover diffractometer to establish phase and crystalline orientation of the individual thin film layers. The x-rays were Cu$K\alpha$ ($\lambda = 1.54$ Å) radiation, with the source operating at 40 kV and 40 mA. The film surface morphology was examined by tapping mode atomic force microscopy (AFM) using a Veeco Multimode V scanning probe microscope. The resonance frequency of the tips used was in the range 310–490 kHz, and the force constant varied between 22 and 91 N/m. The scan area was typically 5×5 µm^2, with a scan rate of 1 Hz. In order to investigate the ferroelectric and dielectric properties of the PLZT layers, circular Au(200 nm)/Pt(50 nm) top electrodes, 100 µm in diameter, were deposited on the perovskite thin film surface using e-beam evaporation. Polarization hysteresis and capacitance-voltage loops were measured on as grown films at 2 kHz with a small signal amplitude of 0.4 V using an Aixacct TF Analyzer 2000 system. The dielectric properties were analyzed for frequencies from 20 Hz to 1 MHz, at a bias level of 1 V_{RMS}, with an HP 4284A Precision *LCR* meter.

Polarized light from a $\lambda = 633$ nm HeNe laser (Melles Griot 25-LHR-151) was coupled into PLZT layers with a thickness of ~650 nm, for films grown on both $SrTiO_3$ and MgO, without the SRO electrode layer, using an ADT-6 rutile prism pressed against the perovskite film surface. This setup, commonly referred to as a prism-film coupler [18–20], is used to determine the thickness and refractive index of optically transparent thin films by running a numerical fit to the observed m-lines [21]. A schematic of the prism-film coupler is shown in Figure 6.1. Light directed into the prism undergoes total reflection at the prism base. Reflected light emerging from the right face of the prism is projected onto a detector screen. Propagating optical modes are exited in the PLZT layer at certain angles of incidence θ_{in}, via overlapping evanescent fields [18], i.e., provided that the air gap d_0 between prism and film is less than $\sim\lambda/4$ [22]. The energy losses associated with this excitation can be visually observed as a pattern of streaks (m-lines) on the detector screen, revealing the mode spectrum of the optical thin film. Complementary ellipsometric data for PLZT films grown on both $SrTiO_3$ and MgO was obtained using an MM-16 (Horiba Jobin Yvon) spectroscopic ellipsometer. The measurements were carried out with a 2 nm increment in wavelength over the full 430–850 nm range. The angle of incidence was 65°. A commercial software package (DeltaPsi2) was used to obtain a numerical fit to the recorded data, adopting the Levenberg-Marquardt nonlinear least-squares algorithm [23] and a single oscillator Sellmeier model for the refractive index dispersion, [24, 25]

$$n^2(\lambda) - 1 = \frac{S_0\lambda_0^2}{1 - (\lambda_0/\lambda)^2}, \tag{6.1}$$

where S_0 and λ_0 represent the average oscillator strength and position, respectively.

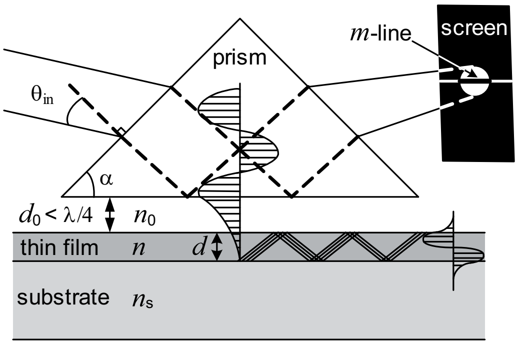

Figure 6.1: Schematic of the prism-film coupler. The incident focused laser beam is totally reflected at the prism base. Wave guided modes in the optical thin film are excited selectively at certain angles of incidence, θ_{in}. The m-lines appearing on the detector screen are used to estimate numerically the thickness d and refractive index n of the optical thin film.

6.3 Results and discussion

6.3.1 Thin film crystalline structure and topography

Figures 6.2(a) and (b) display typical θ-2θ x-ray diffractograms for the PLZT/SRO bilayer for deposition on $SrTiO_3(001)$ and MgO (001), respectively. The diffractograms show (110)-oriented SRO and (001)-oriented PLZT. For films grown on $SrTiO_3$, purely (001)-oriented perovskite PLZT was obtained for substrate temperatures in the range 490–570°C, whereas a pyrochlore phase was found to prevail for substrate temperatures below ∼490°C. For films grown on MgO, domains of different crystalline orientations were commonly observed, dependent on the substrate temperature as well as the overall gas pressure. In order to prevent the formation of pyrochlore for films grown on MgO, an increased ambient pressure of 165 mTorr was required, compared to 100 mTorr for films grown on $SrTiO_3$. Purely (001)-oriented PLZT could be grown on MgO at this total pressure (165 mTorr) for a limited range of substrate temperatures,

$T_{\text{sub}} = 550\pm10°\text{C}$.

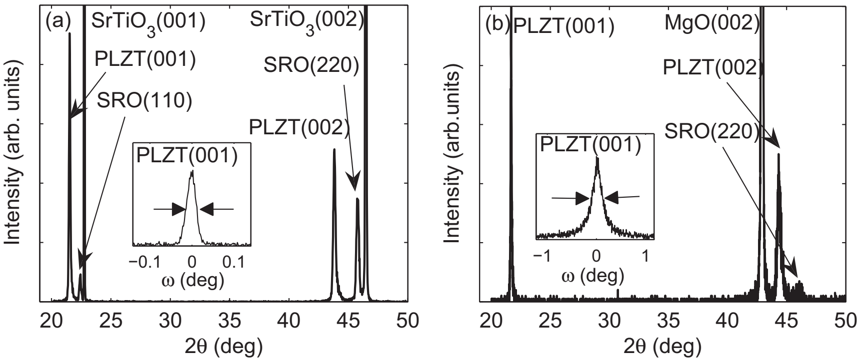

Figure 6.2: θ-2θ scans of a PLZT/SRO bilayer grown on (a) $SrTiO_3$(001) and (b) MgO(001). The diffractograms show purely (001)-oriented monocrystalline PLZT and (110)-oriented SRO on both substrates. The insets show the rocking curves for the PLZT(001) diffraction, with a FWHM of ∼0.03° and ∼0.3° for films grown on $SrTiO_3$ and MgO, respectively.

For films grown on $SrTiO_3$, the rocking curve full width at half maximum (FWHM) for the PLZT(001) and SRO(110) diffraction peaks were measured at ∼0.03°, comparable to that of the substrate (001) Bragg reflection. The FWHM of the corresponding rocking curves for PLZT and SRO deposited on MgO was measured at ∼0.3° and ∼1°, respectively. In Figure 6.2, the rocking curve recorded for the PLZT(001) reflection is shown in the inset of each θ-2θ scan. The FWHM for PLZT on SRO/MgO(001) is comparable to that previously reported for deposition on CeO_2/YSZ-buffered Si(100) [4], and smaller than that reported for deposition on Pt/MgO(001) [26, 27]. The larger mosaic spread of PLZT and SRO grown on MgO, as compared to films grown on $SrTiO_3$, is attributed to the larger lattice mismatch with the substrate. For PLZT, these mismatches for growth on MgO and $SrTiO_3$ are 4.6 % and 3.1 %, respectively. The XRD data confirms that the crystalline quality of the PLZT film is not appreciably affected by incorporation of a thin SRO layer in the heteroepitaxial thin film stack.

For PLZT grown on $SrTiO_3(001)$ without the SRO electrode layer, a minimum (001) rocking curve FWHM of ~0.03° was obtained for a substrate temperature of 530±10°C. For films grown at substrate temperatures above 550°C the crystalline quality of the sputter-deposited PLZT film deteriorates, as judged from the rocking curve FWHM, presumably due to loss of Pb, as was previously observed with x-ray photoelectron spectroscopy for films deposited at elevated substrate temperatures [4].

Figure 6.3 shows typical φ-scans for a PLZT/SRO bilayer on (a) $SrTiO_3(001)$ and (b) MgO(001). The fourfold symmetry of these azimuthal scans is evidence of in-plane alignment of the PLZT and SRO layers, with the [100] crystalline axis of PLZT parallel to that of the substrate.

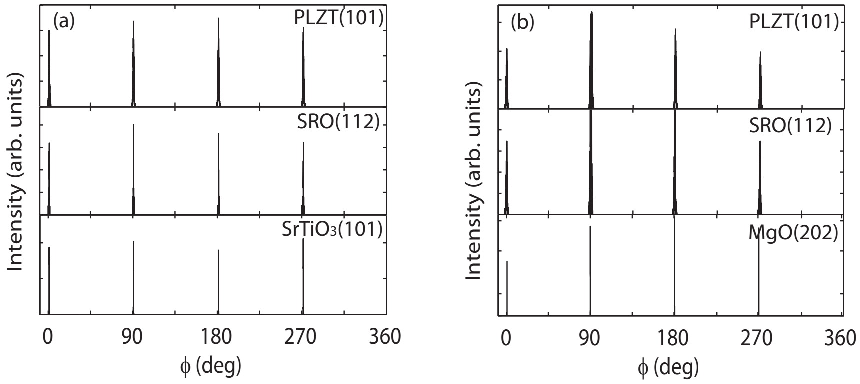

Figure 6.3: φ-scans of a PLZT/SRO bilayer grown on (a) $SrTiO_3$ and (b) MgO. The observed fourfold symmetry verifies in-plane alignment of the PLZT and SRO layers.

Figure 6.4 shows a reciprocal space map of the PLZT/SRO bilayer on $SrTiO_3$. The recorded h and l coordinates of the (332) reflection of the orthorhombic SRO unit cell ($a = 0.5532$ nm, $b = 0.5572$ nm, $c = 0.7850$ nm) [28] imply that the SRO layer is compressively strained from isomorphic growth on the $SrTiO_3$ substrate. The SRO unit cell will expand accordingly, perpendicular to the film surface. The recorded (220) diffraction from SRO at $2\theta = 45.78°$ in

Figure 6.2(a) corroborates this finding. The measured 2θ angle corresponds to an out-of-plane lattice constant $c = 0.3961$ nm, exceeding that of the pseudo-cubic lattice constant for bulk SRO (0.3928 nm) by approximately 1 %. The reciprocal space map also shows that the PLZT(103) reflection is shifted relative to that of $SrTiO_3$(103) by $\Delta h = 0.029$. This translates into a PLZT in-plane lattice parameter of ~0.4020 nm, as compared to $a = b = 0.4029$ nm for bulk $Pb_{0.92}La_{0.08}Zr_{0.4}Ti_{0.6}O_3$ [9]. The PLZT(002) reflection at $2\theta = 43.85°$ in Figure 6.2(a) implies an out-of-plane lattice parameter $c = 0.4126$ nm, consistent with the measured in-lattice parameters, to render a PLZT unit cell volume of 66.7 $Å^3$, in good agreement with that of bulk $Pb_{0.92}La_{0.08}Zr_{0.4}Ti_{0.6}O_3$. Similar measurements for PLZT on MgO yielded in-plane and out-of-plane lattice parameters of $a = 0.4021$ nm and $c = 0.4108$ nm, respectively, suggesting partially relaxed growth of PLZT for these ~500 nm thick films also on the MgO substrate.

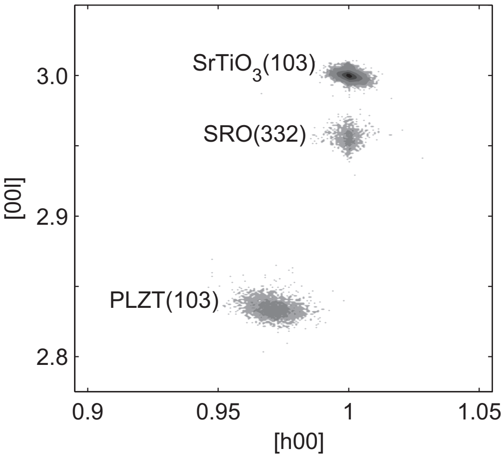

Figure 6.4: Reciprocal space map of a PLZT/SRO bilayer on $SrTiO_3$(001). The PLZT(103) peak is shifted by $\Delta h = 0.029$ relative to that of the orthorhombic SRO(332) and $SrTiO_3$(103) Bragg peaks.

AFM scans of the PLZT/SRO bilayer showed that the root mean square (RMS) surface roughness of the PLZT films increases with layer thickness for films grown on $SrTiO_3(001)$ and MgO(001) alike. For PLZT films 150, 300, and 500 nm thick, the RMS surface roughness was measured at 0.9, 1.5, and 2.3 nm, respectively. Their surface roughness was not appreciably affected by introduction of an SRO electrode layer. Hence, the surface roughness of films with sufficient thickness for optical waveguide applications meets the requirements for light propagation with moderate losses from surface scattering, (i.e., an RMS surface roughness less than ∼2–4 nm) [29]. This suggests that the surface topography of the sputter-deposited PLZT is adequate for application in optical waveguides and integrated optics.

Inspection of the film surface with scanning electron microscopy shows uniform PLZT layers with no visible voids or cracks. Moreover, the measured surface roughness of ∼80 nm thin PLZT layers grown by on-axis sputter deposition is comparable to that previously reported for films grown on $SrTiO_3(001)$ in the off-axis sputter geometry [30]. This observation suggests that the target geometry has little impact on the surface roughness of the sputter-deposited PLZT films.

6.3.2 Ferroelectric and dielectric measurements

The ferroelectric hysteresis behavior of PLZT films grown on SRO/$SrTiO_3$ and SRO/MgO is displayed in Figure 6.5(a). The P-E loops show an average remanent polarization $P_r = 36$ µC/cm^2 and a coercive field $E_c = 230$ kV/cm for PLZT on $SrTiO_3$ and corresponding values $P_r = 36$ µC/cm^2 and $E_c = 140$ kV/cm for PLZT on MgO. The measured remanent polarization and coercive fields are larger than that previously reported for $Pb_{0.92}La_{0.08}Zr_{0.4}Ti_{0.6}O_3$ thin films (26 µC/cm^2, 37 kV/cm) and bulk crystals (28 µC/cm^2, 21 kV/cm) [9, 31]. The distinct hysteresis loops suggest that the sputter-deposited PLZT films are well suited for optical waveguide devices, for which a linear electro-optic response is desired.

The inset in Figure 6.5(a) shows the corresponding C-V switching curve for PLZT on $SrTiO_3$. We observe that the P-E and C-V loops are shifted toward a negative bias, as was previously reported for $Pb(Zr,Ti)O_3$ and PLZT thin films [32, 33]. The different work functions for the Pt ($q\Phi_m = 5.5$ eV) [34] and SRO ($q\Phi_m = 5.2$ eV)

[35] top and bottom electrodes contribute to this bias [36, 37]. $\Delta\Phi_m$ cannot entirely account for the observed negative bias (~90 kV/cm), however. Trapped charges near the film-electrode interfaces and defects may also contribute to the observed bias shift [38].

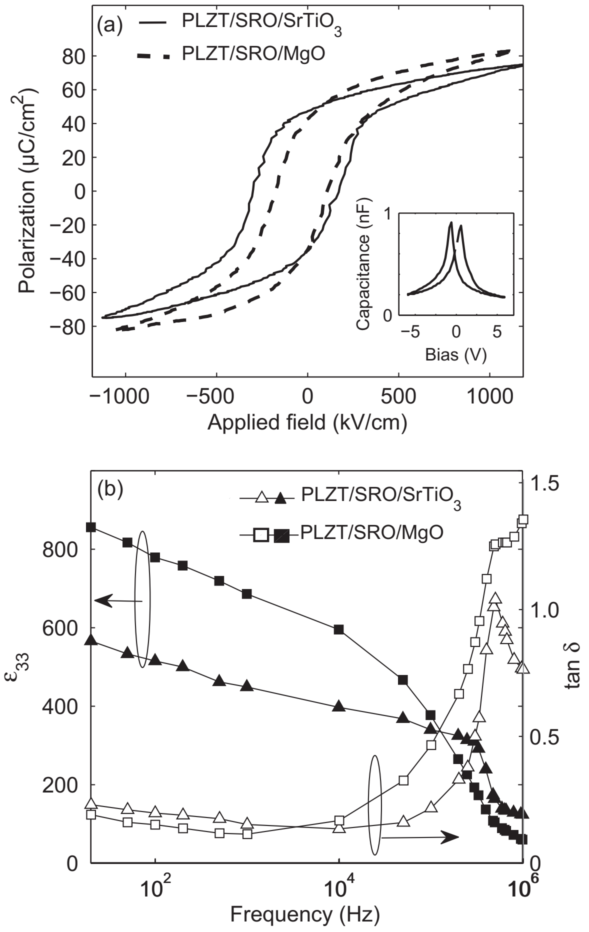

Figure 6.5: (a) P-E hysteresis loops and (b) frequency responses of the dielectric constant ε_{33} (filled symbols) and the loss tangent tan δ (open symbols) for PLZT thin films grown on SRO/SrTiO$_3$ and SRO/MgO. The inset in (a) shows the measured C-V curve for the PLZT/SRO/SrTiO$_3$ sample.

Figure 6.5(b) shows the room temperature dielectric frequency responses of PLZT grown on SRO/$SrTiO_3$ and SRO/MgO, respectively. The dielectric tensor component ε_{33} was estimated from the measured capacitance, assuming an ideal parallel-plate geometry. For frequencies below 100 kHz, ε_{33} is larger for PLZT on MgO, as compared to films deposited on $SrTiO_3$ substrate. At 10 kHz, ε_{33} is measured at $\sim$600 and $\sim$400 for films grown on MgO and $SrTiO_3$, respectively. These values are comparable to the dielectric constant ($\varepsilon = 982$) reported for bulk $Pb_{0.92}La_{0.08}Zr_{0.4}Ti_{0.6}O_3$ [9]. The loss tangent (tan δ) is measured at $\sim$0.2 for frequencies below 10 kHz and increases rapidly around 100 kHz for PLZT thin films grown on both substrates. Similar behavior was previously reported for capacitance measurements on PLZT, Pb(Zr,Ti)O_3, and (Pb,La)TiO_3 thin films [39, 40], and attributed to a resonance in the measurement setup [41].

6.3.3 Optical characterization

In Figure 6.6, the laser beam angle of incidence θ_{in} (cf. Figure 6.1) is plotted versus mode order for the observed m-lines of transverse electric (TE) and transverse magnetic (TM) polarized light coupled into a PLZT film grown on MgO substrate. The continuous curves in this plot are best fits from corresponding model calculations relating θ_{in} to mode order for TE and TM polarized light of λ = 633 nm. The optically transparent thin film layer in this simulation had a film thickness of d = 640 nm, refractive index of n = 2.57, birefringence of $\Delta n = n_{\text{TE}} - n_{\text{TM}} = 5 \times 10^{-3}$, and an opening angle of $\alpha = 45°$ of the rutile prism. Corresponding fits to the m-lines observed for PLZT on $SrTiO_3$ rendered a refractive index n = 2.56, consistent with that reported for bulk $Pb_{0.92}La_{0.08}Zr_{0.4}Ti_{0.6}O_3$ at λ = 633 nm [42]. In these model calculations, the refractive index of the substrate was set at $n_s = 2.38$ for $SrTiO_3$ and $n_s = 1.74$ for MgO [43, 44].

Figure 6.7(a) shows the recorded ellipsometric parameters Ψ and Δ for the PLZT thin film on MgO, along with a numerical fit to the data. A surface roughness of 2 nm (RMS) for the PLZT layer was implemented in the model, adopting an effective medium approxima-

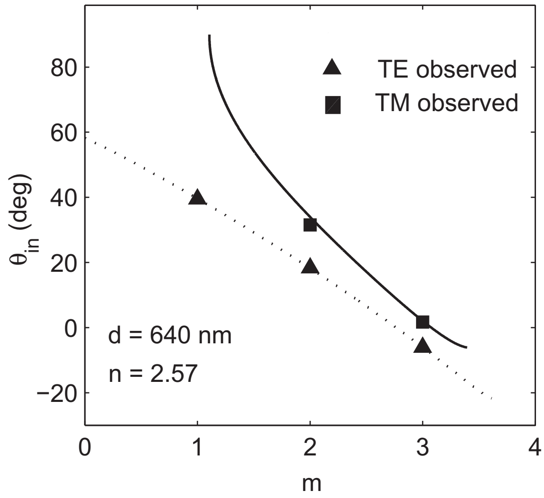

Figure 6.6: Measured interdependence of the laser beam angle of incidence θ_{in} and the mode order m for rutile prism coupling measurements (cf. Figure 6.1) of a PLZT thin film on MgO for TE and TM polarized light. The best fit for TE (dashed line) and TM polarization (solid line) suggests a refractive index $n = 2.57$ and a film thickness $d = 640$ nm for the actual wavelength of $\lambda = 633$ nm.

tion [45, 46]. The fit in Figure 6.7(a) corresponds to $S_0 = 1.05 \times 10^{14}$ m^{-2} and $\lambda_0 = 215.1$ nm (of Eq. 6.1), which suggests a film thickness of ∼650 nm and a refractive index $n \sim 2.55$ for $\lambda = 633$ nm, in good agreement with the data obtained from the prism coupling measurements. These values for the single Sellmeier oscillator match those previously reported for PLZT thin films [47–49]. Figure 6.7(b) shows the calculated dispersion of the refractive index for PLZT grown on $SrTiO_3$ and MgO for wavelengths spanning the 450–1600 nm range. We note that there is no major difference in the calculated dispersions for PLZT films on these two substrate materials. At the main communication wavelength of $\lambda = 1550$ nm, the refractive index of the PLZT layer is $n \sim 2.45$.

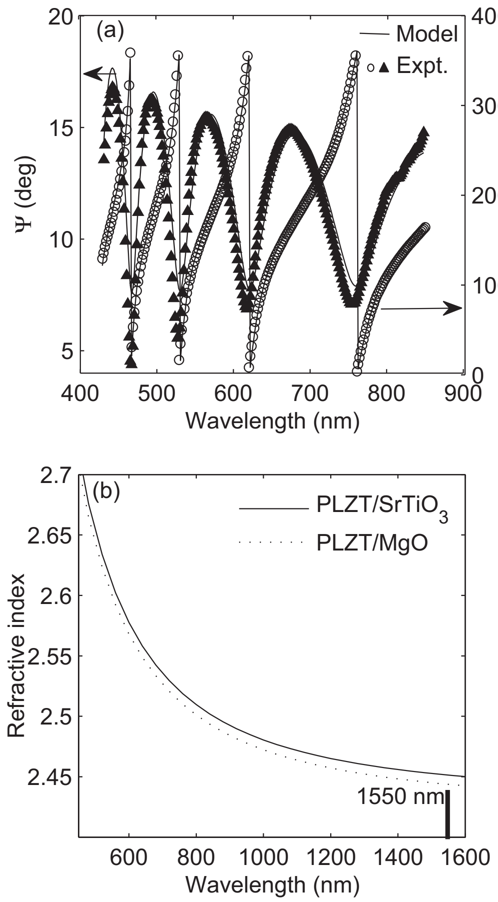

Figure 6.7: (a) Spectrometric ellipsometry data (Ψ, Δ) with best fit from model calculations for a PLZT thin film on MgO. (b) Calculated dispersion of the refractive index for PLZT/SrTiO$_3$ and PLZT/MgO.

6.4 Conclusions

PLZT and SRO thin films were grown epitaxially on SrTiO$_3$(001) and MgO(001) substrates by RF magnetron sputtering. The recorded rocking curves suggest that the PLZT epilayers are of good crystalline quality on both substrates. In-plane epitaxial alignment was confirmed from φ-scans, and the RMS surface roughness was measured at ∼2 nm for PLZT films of ∼0.5 µm thickness, sufficient to meet the requirements for low-loss optical mode propagation in such films. The measured P-E hysteresis loops showed good ferroelectric behavior for films grown on both substrates, with a large coercive field and an average remanent polarization of $P_r = 36$ µC/cm^2. The dielectric constants (ε_{33}) at 10 kHz were measured at ∼600 and ∼400 for films deposited on MgO and $SrTiO_3$, respectively. Film thickness and refractive index were determined by rutile prism coupling and were found to be consistent with values derived from spectroscopic ellipsometry measurements. The dispersion of the refractive index was computed by means of a single oscillator Sellmeier model and was estimated at $n \approx 2.55$ for $\lambda = 633$ nm and $n \approx 2.45$ for $\lambda = 1550$ nm for PLZT epilayers grown on both substrates. The ferroelectric and optical characteristics of these PLZT thin films, as well as their surface roughness, were not appreciably different for the two substrates. This finding favors MgO as the preferred choice of substrate for optical waveguide applications due to its low refractive index compared with $SrTiO_3$.

References

[1] Lines, M. E., and Glass, A. M., *Principles and applications of ferroelectric and related materials.* Oxford, UK: Clarendon Press, 1988.

[2] Scott, J. F., "Applications of modern ferroelectrics," *Science*, vol. 315, pp. 954–959, 2007.

[3] Ramesh, R., and Spaldin, N. A., "Multiferroics: progress and prospects in thin films," *Nat. Mater.*, vol. 6, pp. 21–29, 2007.

[4] Nordseth, Ø., Tybell, T., and Grepstad, J. K., "Epitaxial (Pb,La)(Zr,Ti)O_3 thin films on buffered Si(100) by on-axis radio frequency magnetron sputtering," *Thin Solid Films*, vol. 517, pp. 2623–2626, 2009.

[5] Cross, L. E., "Relaxor ferroelectrics," *Ferroelectrics*, vol. 76, pp. 241–267, 1987.

[6] Dawber, M., Rabe, K. M., and Scott, J. F., "Physics of thin-film ferroelectric oxides," *Rev. Mod. Phys.*, vol. 77, pp. 1083–1130, 2005.

[7] Haertling, G. H., "PLZT electrooptic materials and applications – a review," *Ferroelectrics*, vol. 75, pp. 25–55, 1987.

[8] Wu, Y. J., Li, J., Chen, X. M., Kimura, R., and Kakegawa, K., "Effects of La_2O_3 addition and PbO excess on the transmittance of $PbZrO_3$-$PbTiO_3$-$Pb(Zn_{1/3}Nb_{2/3})O_3$ ceramics by spark plasma sintering," *J. Am. Ceram. Soc.*, vol. 91, pp. 13–16, 2008.

[9] Haertling, G. H., and Land, C. E., "Hot pressed $(Pb,La)(Zr,Ti)O_3$ ferroelectric ceramics for electrooptic applications," *J. Am. Ceram. Soc.*, vol. 54, pp. 1–11, 1971.

[10] Haertling, G. H., "Improved hot pressed electrooptic ceramics in the $(Pb,La)(Zr,Ti)O_3$ system," *J. Am. Ceram. Soc.*, vol. 54, pp. 303–309, 1970.

[11] Rouchon, J. M., and Micheron, F., "Electrooptical properties and photoinduced effects in PLZT ceramics applications to optical storage and processing of information," *Czech. J. Phys. B*, vol. 25, pp. 575–584, 1975.

[12] Thacher, P. D., "A linear electrooptic effect in ferroelectric ceramics: PLZT 12/40/60," *Ferroelectrics*, vol. 3, pp. 147–150, 1972.

[13] Ruppe, C., and Duparre, A., "Roughness analysis of optical films and substrates by atomic force microscopy," *Thin Solid Films*, vol. 288, pp. 8–13, 1996.

[14] Nashimoto, K., Nakamura, S., Morikawa, T., Moriyama, H., Watanabe, M., and Osakabe, E., "Electrooptical properties of heterostructure $(Pb,La)(Zr,Ti)O_3$

waveguides on Nb-SrTiO$_3$," *Jpn. J. Appl. Phys.*, vol. 38, pp. 5641–5645, 1999.

[15] Hartmann, A. J., Nielson, M., Lamb, R. N., Watanabe, K., and Scott, J. F., "Ruthenium oxide and strontium ruthenate electrodes for ferroelectric thin-film capacitors," *Appl. Phys. A*, vol. 70, pp. 239–242, 2000.

[16] Triscone, J.-M., Frauchiger, L., Decroux, M., Mieville, L., Fischer, Ø., Beeli, C., Stadelmann, P., and Racine, G.-A., "Growth and structural properties of epitaxial Pb(Zr$_x$Ti$_{1-x}$)O$_3$ films and Pb(Zr$_x$Ti$_{1-x}$)O$_3$-cuprate heterostructures," *J. Appl. Phys.*, vol. 79, pp. 4298–4305, 1996.

[17] Parratt, L. G., "Surface studies of solids by total reflection of x-rays," *Phys. Rev.*, vol. 95, pp. 359–369, 1954.

[18] Tien, P. K., Ulrich, R., and Martin, R. J., "Modes of propagating light waves in thin deposited semiconductor films," *Appl. Phys. Lett.*, vol. 14, pp. 291–294, 1969.

[19] Harris, J. H., Shubert, R., and Polky, J. N., "Beam coupling to films," *J. Opt. Soc. Am.*, vol. 60, pp. 1007–1016, 1970.

[20] Ulrich, R., and Torge, R., "Measurement of thin film parameters with a prism coupler," *Appl. Opt.*, vol. 12, pp. 2901–2908, 1973.

[21] Tien, P. K., and Ulrich, R., "Theory of prism-film coupler and thin-film light guides," *J. Opt. Soc. Am.*, vol. 60, pp. 1325–1337, 1970.

[22] Tien, P. K., "Light waves in thin film and integrated optics," *Appl. Opt.*, vol. 10, pp. 2395–2413, 1971.

[23] Marquardt, D. W., "An algorithm for least squares estimation of non-linear parameters," *J. Soc. Industr. Appl. Math.*, vol. 11, pp. 431–441, 1963.

[24] DiDomenico, M., and Wemple, S. H., "Oxygen-octahedra ferroelectrics. I. Theory of electro-optical and nonlinear optical effects," *J. Appl. Phys.*, vol. 40, pp. 720–734, 1969.

[25] Wemple, S. H., and DiDimenico, M., "Behavior of the electronic dielectric constant in covalent and ionic materials," *Phys. Rev. B*, vol. 3, pp. 1338–1351, 1971.

[26] Kobune, M., Matsuura, O., Matsuzaki, T., Mineshige, A., Fujii, S., Fujisawa, H., Shimizu, M., and Niu, H., "Effects of Pt/$SrRuO_3$ top electrodes on ferroelectric properties of epitaxial $(Pb,La)(Zr,Ti)O_3$ thin films," *Jpn. J. Appl. Phys.*, vol. 39, pp. 5451–5455, 2000.

[27] Wakabayashi, R., Kobune, M., Sawada, T., Kojima, S., and Honda, K., "Physical properties of $(Pb,La)(Zr,Ti)O_3$ films crystallized by one-step postdeposition annealing using nucleus-insertion method," *Int. Ferroelectr.*, vol. 46, pp. 27–35, 2002.

[28] Bouchard, R. J., and Gillson, J. L., "Electrical properties of $CaRuO_3$ and $SrRuO_3$ single crystals," *Mater. Res. Bull.*, vol. 7, pp. 873–878, 1972.

[29] Leng, W. J., Yang, C. R., Ji, H., Zhang, J. H., Chen, H. W., and Tang, J. L., "Structure-related optical properties of $(Pb,La)(Zr,Ti)O_3$ thin films on indium tin oxide/quartz substrates," *J. Appl. Phys.*, vol. 100, p. 083505, 2006.

[30] Kumar, A. K. S., Dahl, Ø., Pettersen, S. V., Grepstad, J. K., and Tybell, T., "Characterization of crystalline $Pb_{0.92}La_{0.08}Zr_{0.4}Ti_{0.6}O_3$ thin films grown by off-axis radio frequency magnetron sputtering," *Thin Solid Films*, vol. 492, pp. 71–74, 2005.

[31] Kobune, M., Matsuura, O., Matsuzaki, T., Sawada, T., Fujisawa, H., Shimizu, M., Niu, H., and Honda, K., "Microstructure and electrical properties of $(Pb,La)(Zr,Ti)O_3$ films crystallized from amorphous state by two-step postdeposition annealing," *Jpn. J. Appl. Phys.*, vol. 40, pp. 5554–5558, 2001.

[32] Lee, J., Choi, H., Park, B. H., Noh, T. W., and Lee, J. K., "Built-in voltages and asymmetric polarization switching in Pb(Zr,Ti)O_3 thin film capacitors," *Appl. Phys. Lett.*, vol. 72, pp. 3380–3382, 1998.

[33] Pike, G. E., Warren, W. L., Dimos, D., Tuttle, B. A., Ramesh, R., Lee, J., Keramidas, V. G., and Evans, J. T., "Voltage offsets in (Pb,La)(Zr,Ti)O_3 thin films," *Appl. Phys. Lett.*, vol. 66, pp. 484–486, 1995.

[34] Goldmann, A., *Landolt-Börnstein - Group III: Condensed Matter.* Berlin, Germany: Springer-Verlag, edited by W. Martienssen, 23rd ed., 2003.

[35] Yoshida, C., Yoshida, A., and Tamura, H., "Nanoscale conduction modulation in Au/Pb(Zr,Ti)O_3/SrRuO_3 heterostructure," *Appl. Phys. Lett.*, vol. 75, pp. 1449–1451, 1999.

[36] Lin, Y., Zhao, B. R., Peng, H. B., Hao, Z., Xu, B., Zhao, Z. X., and Chen, J. S., "Asymmetry in the hysteresis loop of Pb($Zr_{0.53}Ti_{0.47}$)O_3/SiO_2/Si structures," *J. Appl. Phys.*, vol. 86, pp. 4467–4472, 1999.

[37] Lo, V. C., and Chen, Z. J., "Simulation of the effects of space charge and Schottky barriers on ferroelectric thin film capacitor using Landau Khalatnikov theory," *IEEE Trans. Ultrason. Ferroelectr. Freq. Control*, vol. 49, pp. 980–986, 2002.

[38] Dimos, D., Warren, W. L., Sinclair, M. B., Tuttle, B. A., and Schwartz, R. W., "Photoinduced hysteresis changes and optical storage in (Pb,La)(Zr,Ti)O_3, thin films and ceramics," *J. Appl. Phys.*, vol. 76, pp. 4305–4315, 1994.

[39] Dey, S. K., and Lee, J. J., "Cubic paraelectric (nonferroelectric) perovskite PLT thin films with high permittivity for ULSI DRAM's and decoupling capacitors," *IEEE Trans. Electron. Dev.*, vol. 39, pp. 1607–1613, 1992.

[40] Thomas, R., Mochizuki, S., Mihara, T., and Ishida, T., "PZT(65/35) and PLZT(8/65/35) thin films by sol-gel process:

a comparative study on the structural, microstructural and electrical properties," *Thin Solid Films*, vol. 443, pp. 14–22, 2003.

[41] Polishchuk, I., Brown, G., and Huff, H., "Sources of resonance-related errors in capacitance versus voltage measurement systems," *Rev. Sci. Instrum.*, vol. 71, pp. 3962–3963, 2000.

[42] Thacher, P. D., "Refractive index and surface layers of ceramic (Pb,La)(Zr,Ti)O_3 compounds," *Appl. Opt.*, vol. 16, pp. 3210–3213, 1977.

[43] McKee, R. A., Walker, F. J., Specht, E. D., Jellison, G. E., Boatner, L. A., and Harding, J. H., "Interface stability and the growth of optical quality perovskites on MgO," *Phys. Rev. Lett.*, vol. 72, pp. 2741–2744, 1994.

[44] Hwang, K. S., Kim, C. K., Kim, S. B., Kwon, J. T., Lee, J. S., Yun, Y. H., Kim, Y. H., and Kang, B. A., "Preparation of epitaxial and polycrystalline bismuth titanate thin films on single crystal (100) MgO by chemical solution deposition," *Surf. Coat. Technol.*, vol. 150, pp. 177–181, 2002.

[45] Bruggemann, D. A. G., "The calculation of various physical constants of heterogeneous substances. I. The dielectric constants and conductivities of mixtures composed of isotropic substances," *Ann. Phys.*, vol. 24, pp. 636–664, 1935.

[46] Aspnes, D. E., "Optical response of microscopically rough surfaces," *Phys. Rev. B*, vol. 41, pp. 10334–10343, 1990.

[47] Tunaboylu, B., Harvey, P., and Esener, S. C., "Characterization of dielectric and electro-optic properties of PLZT 9/65/35 films on sapphire for electro-optic applications," *IEEE Trans. Ultrason. Ferroelectr. Freq. Control*, vol. 45, pp. 1105–1112, 1998.

[48] Okuyama, M., Usuki, T., Hamakawa, Y., and Nakagawa, T., "Epitaxial growth of ferroelectric PLZT thin films and their optical properties," *Appl. Phys.*, vol. 21, pp. 339–343, 1980.

[49] Li, H., Zhang, Y., Wen, J., Yang, S., Mo, D., Cheng, C. H., Xu, Y., and Meckenzie, J. D., "Optical properties of lead lanthanum zirconate titanate amorphous ferroelectric-like thin films," *Jpn. J. Appl. Phys.*, vol. 39, pp. 1180–1183, 2000.

Chapter 7

Growth and characterization of (Pb,La)(Zr,Ti)O_3 thin film epilayers on $SrTiO_3$-buffered Si(001)

Nordseth, Ø., You, C. C., Folven, E., Gariglio, S., Sambri, A., Triscone, J. -M., Reiner, J. W., Ahn, C. H., Tybell, T., and Grepstad, J. K., accepted for publication in Thin Solid Films.

Abstract: Ferroelectric $Pb_{0.92}La_{0.08}Zr_{0.4}Ti_{0.6}O_3$ (PLZT) thin films were deposited on $SrTiO_3$-buffered Si(001) substrate by on-axis radio frequency magnetron sputtering. X-ray diffraction analysis revealed epitaxial growth of monocrystalline PLZT films, with an (001) rocking curve full width at half maximum of $\sim 0.3°$. φ-scans showed 45° in-plane orientation of the perovskite unit cell relative to that of silicon. The elemental composition of the thin film heterostructure was examined by Auger sputter depth profiling measurements. The recorded profiles suggest that the $SrTiO_3$ buffer layer serves not only as a template for epitaxial growth, but also as a barrier suppressing Pb-Si interdiffusion between the PLZT layer and the Si substrate. The surface roughness of the PLZT layer was measured at $\sim$4 nm for films with $\sim$500 nm thickness. Wavelength dispersions for the refractive index (n) and the extinction coefficient (k) were

obtained from spectroscopic ellipsometry measurements, with $n \sim 2.48$ at the main communication wavelength $\lambda = 1550$ nm and $k < 0.001$ for $\lambda > 650$ nm. Recorded polarization vs. electric field (P-E) loops for the PLZT epilayer, with a $SrRuO_3$ electrode layer interposed between PLZT and $SrTiO_3$, showed a remanent polarization $P_r \approx 40$ µC/cm^2 and coercive field $E_c \approx 100$ kV/cm. These findings suggest that the sputter-deposited PLZT thin films retain the functional properties critical to ferroelectric and electro-optic device applications, also when integrated on a semiconductor substrate.

7.1 Introduction

Perovskite complex oxides offer a variety of functional properties [1], which render these materials attractive for a broad range of device applications, including capacitors [2], nonvolatile memory [3], and electro-optic components [4]. The possibility to combine such oxides epitaxially with common semiconductor materials is intriguing from the prospect of integrating these materials with Si-based technology. Epitaxial growth of high quality perovskite thin films on silicon is a challenge [5–8], on account of lattice mismatch, formation of amorphous surface oxide, and cation interdiffusion at the film/substrate interface. Deposition of a $SrTiO_3$ (STO) buffer layer on Si(001) by molecular beam epitaxy (MBE) has been shown to facilitate subsequent growth of monocrystalline perovskite thin films on this substrate [9–12]. Moreover, the STO buffer layer may serve as a diffusion barrier, to prevent chemical reactions with the Si substrate during perovskite thin film growth and processing [13].

The ferroelectric perovskite (Pb,La)(Zr,Ti)O_3 (PLZT) is recognized as an attractive material for thin film waveguide applications, with high transparency at visible and infrared frequencies, strong linear electro-optic response (Pockels effect), and large spontaneous polarization [14, 15]. For low-loss waveguide devices, monocrystalline thin films are desired, since propagation losses are expected to be lower than in those prepared with polycrystalline films, in which the grain boundaries cause optical scattering [16, 17]. Optical losses in thin film waveguides also have other causes, such as scattering from defects and pores, material absorption, and surface scattering [18]. For monocrystalline thin films, the predominant loss mechanism is surface scattering governed by the film surface morphology. In order to satisfy the requirement of low scattering losses (1–2 dB/cm) in electro-optic thin film devices, the root mean square (RMS) surface roughness should not exceed ∼2-4 nm [19]. Moreover, the electro-optic properties of perovskite oxides are highly anisotropic [16]. This implies that the optimum configuration of an electro-optic device, such as waveguide orientation, polarization of the propagating optical modes, and direction of the applied electric field, will depend on the crystalline orientation of the thin film. Thus, good control of the growth orientation is an important concern for device applications.

In this study, we report growth of monocrystalline PLZT thin film epilayers on STO-buffered Si(001) by radio frequency (RF) magnetron sputtering. The chosen composition of PLZT, with 8 % lanthanum substitution for Pb and a Zr:Ti cation ratio of 40:60, is known to crystallize in a tetragonal phase with linear electro-optic response and a large coercive field [14], characteristics attractive to a variety of optical devices (e.g., electro-optic switches, modulators, detectors). The structural, ferroelectric, and optical properties, as well as the surface morphology of these Si-integrated PLZT epilayers were investigated. Furthermore, the PLZT interface with STO-buffered Si(001) was examined by means of Auger sputter depth profiling and compared with the PLZT/Si(001) interface, i.e., without the STO buffer layer.

7.2 Experimental

A 2 in. diameter Si(001) wafer with an 8 nm thick STO(001) buffer layer grown by MBE methods [9, 20] was cut into 5×5 mm^2 dies before introduction in the sputter deposition system (Kurt J. Lesker Co.). The growth chamber base pressure was 5×10^{-7} Torr. A manually operated gate valve was used to control the overall gas pressure during deposition, and the flow of argon and oxygen (both 6.0 purity) was regulated with mass-flow controllers. The surface temperature of the radiatively heated substrate was measured using an optical pyrometer (IR-CAI, Chino Corp.), with the emissivity set at 0.7 ($\lambda = 1.55$ µm). The PLZT films were deposited in a conventional planar sputter geometry, in order to achieve sufficient growth rates for optical waveguide applications [21], i.e., films with a typical thickness of ∼0.5 µm. A composite target with 20 mol% excess lead, i.e., $Pb_{1.104}La_{0.08}Zr_{0.4}Ti_{0.6}O_3$ (Praxair, 99.9 % purity), was used to obtain a cation make-up close to the desired composition, $Pb_{0.92}La_{0.08}Zr_{0.4}Ti_{0.6}O_3$. The separation between target and substrate was kept at 48 mm, and the substrate surface temperature was controlled within the range 450–600°C. The sputter deposition ambient was a mix of oxygen and argon (O_2:Ar = 4:10) with a total pressure of 165 mTorr, and the RF (13.56 MHz) power was 90 W, yielding a deposition rate of ∼1.7 nm/min. In order to provide a bottom electrode for ferroelectric measurements, a thin (∼40 nm) conducting $SrRuO_3$ (SRO) epilayer was deposited on the STO/Si(001) substrate prior to PLZT growth. This layer was deposited in a 90° off-axis sputter geometry, advantageous to complex oxide thin film epitaxy [22], at a substrate temperature of ∼650°C. The total pressure of the growth ambient was 100 mTorr, and the RF power was 100 W, with a deposition rate of ∼0.5 nm. The PLZT/SRO bilayers were grown without breaking the vacuum. After deposition, the samples were left to cool to room temperature in the growth ambient, before being removed from the sputter chamber. The cooling rate was measured independently at ∼40 K/min for a substrate temperature of 500°C and a chamber pressure of 170 mTorr.

In order to establish the phase and crystalline orientation of the different layers, x-ray diffraction (XRD) measurements were carried out with a Bruker D8 Discover x-ray diffractometer. Grazing incidence measurements were accomplished with the x-ray source rotated through 90°, in order to increase the diffraction intensity from sets of vertically oriented low-index planes in the ultra-thin STO buffer layer. The surface composition of the STO/Si(001) substrate was examined with x-ray photoelectron spectroscopy (XPS), using a VG Escalab MkII spectrometer, and compared with data recorded for HF-etched STO(001) substrates (Shinkosha Co. Ltd.). The XPS data were taken in normal emission as well as for a photoelectron take-off angle (TOA) of approximately 30°, for enhanced surface intensity. The core level peak intensities were estimated using least-squares fitting of Voigt lineshapes to the recorded spectra, adopting CasaXPS ver. 2.3.14 [23]. The binding energies were corrected for electrostatic sample charging by setting the C 1s core level binding energy for emission from adventitious surface carbon to 285.0 eV. Auger depth profiling measurements were carried out with a JEOL JAMP-9500F Auger microprobe to examine the elemental composition of the thin film epilayers, with a special focus on interdiffusion at the film-substrate interface. The argon ion partial pressure in the Auger microprobe during sputter profiling was controlled at 6 $\times$ 10^{-1} mTorr, and the ion beam voltage and current were set at 500 V and 6 $\times$ 10^{-7} A, respectively. Under these conditions, the etching rate of the PLZT layer was estimated at approximately 1.6 nm/min. Element concentrations were assessed from the measured Auger peak intensities, using tabulated elemental sensitivity factors [24]. To investigate the ferroelectric properties of the PLZT films, Au(200 nm)/Pt(10 nm) electrodes of 100 µm in diameter were deposited on the sample surface by electron beam evaporation. Polarization vs. electric field (P–E) and capacitance-voltage (C–V) hysteresis loops were measured with an Aixacct TF 2000 analyzer. The applied bias voltage in the P–E measurements was varied from −7 V to +7 V, and the capacitance was measured at 2 kHz with a small-signal amplitude of 0.4 V. The film surface morphology was examined with tapping mode atomic force microscopy (AFM), using a Veeco Multimode V scanning probe microscope. A variable angle spectroscopic ellipsometer (J. A. Woollam Co.) was employed to obtain the refractive index and extinction coefficient, as well as a measure for the thickness of the PLZT films. The measurements were carried out for wavelengths λ = 350–1700 nm, with a 10 nm increment and 45° angle of incidence. Numerical fits to the recorded ellipsometry parameters (Ψ, Δ) were obtained using a commercial software package [25].

7.3 Results

7.3.1 Structural characterization

To help assess the growth conditions for PLZT epitaxy on the STO/Si(001) substrate, separate XRD measurements were carried out on the STO buffer layer. Figure 7.1(a) shows a θ-2θ scan of the STO(002) diffraction peak for the STO/Si(001) substrate. The STO (002) reflection is centered at $2\theta = 46.33°$, which corresponds to a c-axis lattice constant of 3.916 Å, i.e., slightly stretched compared to the lattice constant of bulk crystalline STO (3.905 Å). The rocking curve full width at half maximum (FWHM) of the STO(002) reflection was measured at $\sim$0.1°. The STO buffer layer thickness was determined at $\sim$15 unit cells, from a numerical fit to the measured oscillation fringes of the STO(002) reflection [26], shown by the solid curve in Figure 7.1(a).

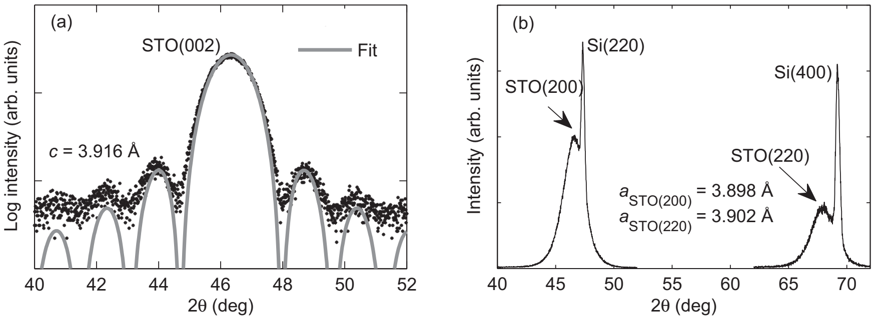

Figure 7.1: (a) θ-2θ scan the STO(002) diffraction from the STO/Si(001) substrate, with a numerical fit to the recorded finite thickness oscillation fringes. (b) Grazing incidence in-plane θ-2θ scans for the STO(200) and STO(220) reflections of the STO buffer layer with the adjacent Si(220) and Si(400) reflections, respectively.

Figure 7.1(b) shows the STO(200) and STO(220) reflections recorded in grazing incidence, with the adjacent Si(220) and Si(400) reflections. The measured 2θ diffraction angles, as obtained using Gaussian fits, correspond to an in-plane lattice constant $a = 3.898$ Å and $a = 3.902$ Å for STO(200) and STO(220), respectively. This implies a small in-plane compressive strain compared to the crystal lattice of bulk STO, which is corroborated by the measured out-of-plane (c-axis) lattice constant.

The θ-2θ x-ray diffractogram of a PLZT thin film grown on STO-buffered Si(001) is shown in Figure 7.2. This diagram shows PLZT(00l) reflections, only, which implies that the layers are monocrystalline with no perceptible impurity phases or grains of a different crystalline orientation. Such growth was observed for substrate temperatures in the range 490–570°C, whereas a pyrochlore phase of PLZT prevailed for growth temperatures below ~490°C. Diffraction from the ultrathin STO buffer layer (nominally 15–20 unit cells thick) could not be clearly discerned in this θ-2θ scan, suppressed by the far thicker PLZT thin film layer. For PLZT/SRO bilayers deposited on STO/Si(001), the θ-2θ scans also showed ($hh0$) diffraction peaks of the orthorhombic SRO unit cell.

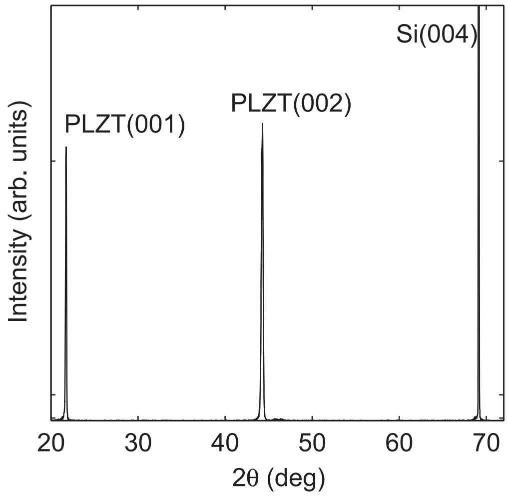

Figure 7.2: θ-2θ x-ray diffractogram of a PLZT epilayer deposited on STO/Si(001). The PLZT thin film is [001]-oriented with no sign of pyrochlore or domains of different crystalline orientation.

The c-axis lattice constant of the PLZT epilayer, as obtained from the measured (001) diffraction angle 2θ, is plotted in Figure

7.3 for films grown directly on STO/Si(001) at different substrate temperatures. The data shows that this lattice constant attains a maximum value of ∼4.09±0.01 Å for substrate temperatures in the range 500–550°C. Also shown in Figure 7.3 is the corresponding rocking curve FWHM for the PLZT(001) reflection. A minimum FWHM of ∼0.3° was obtained for PLZT grown at a substrate temperature of 520°C±10°C. For growth temperatures above ∼550°C, the rocking curve halfwidth increases, presumably due to loss of lead, as was formerly seen in XPS measurements on films grown at elevated substrate temperatures [8]. Moreover, the XRD analyses show that the crystalline quality of the PLZT film is not appreciably affected by introduction of an SRO electrode layer between STO and PLZT.

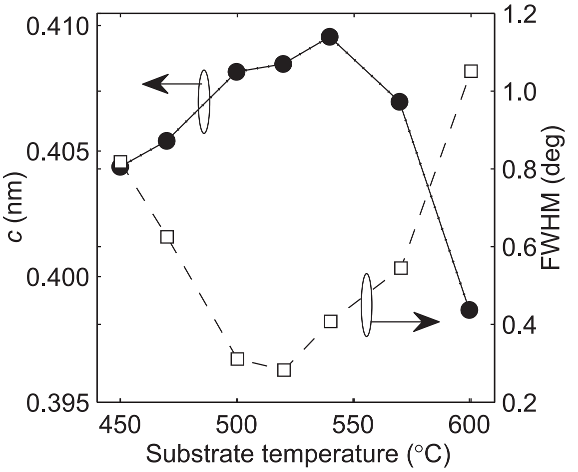

Figure 7.3: Substrate temperature dependence of the c-axis lattice parameter and the rocking curve FWHM for films grown on STO/Si(001), as obtained from the PLZT(001) reflection.

Figure 7.4(a) shows typical φ-scans of a PLZT thin film grown on STO/Si(001). The four-fold symmetry and alignment of the peaks in these diffractograms are evidence of in-plane epitaxial growth of PLZT, with the $\langle 100 \rangle$ crystalline axes of PLZT parallel to that of Si[110], as depicted in Figure 7.4(b). Also, the φ-scans demonstrate that the STO unit cell is rotated by 45° in the surface plane with respect to the low-index crystalline axes of the Si(001) wafer. This implies in-plane epitaxial alignment of STO[100] with Si[110], cf. Figure 7.4(b), consistent with previous reports for thicker films of STO grown on Si(001) substrates [12, 13, 27].

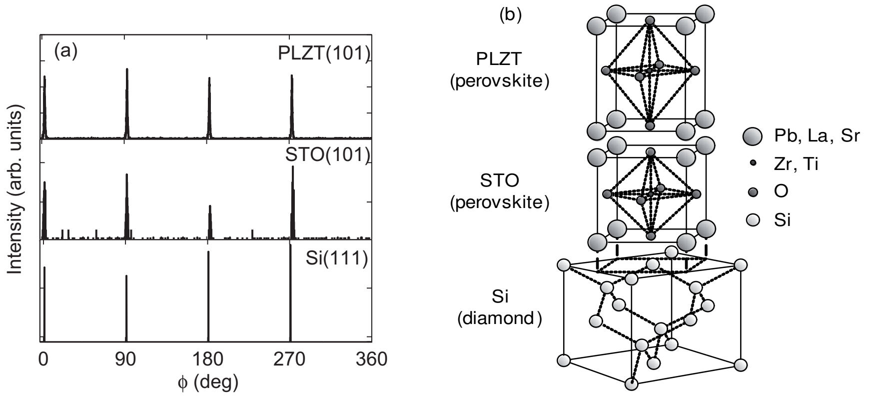

Figure 7.4: (a) φ-scans of the PLZT(101), STO(101), and Si(111) reflections for a thin film epilayer grown on STO/Si(001). The STO(101) scan was obtained from measurements on the STO/Si(001) substrate. (b) The perovskite unit cell of the thin film layers is rotated 45° with respect to the [001]-axis of the Si substrate unit cell.

A reciprocal space map of the PLZT(103) reflection for a film grown on STO/Si(001) is shown in Figure 7.5, superimposed on a corresponding map of the PLZT(103) and STO(103) reflections for a film grown on single-crystal STO(001) [28]. Both films were ∼100 nm thick, grown at a substrate temperature of ∼520°C. The reciprocal lattice parameters of the (103) reflection for the PLZT epilayer on STO/Si(001) translates to an in-plane lattice constant $a = b = 4.024$ Å and an out-of-plane lattice constant $c = 4.085$ Å. This implies a unit cell volume of 66.15 Å^3, in close correspondence with that previously reported for bulk $\mathrm{Pb_{0.92}La_{0.08}Zr_{0.4}Ti_{0.6}O_3}$ [14].

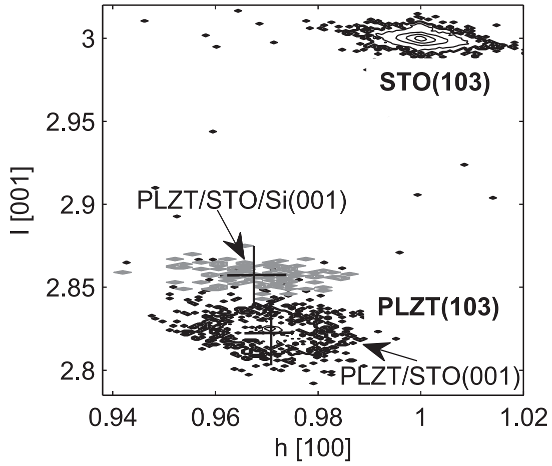

Figure 7.5: Reciprocal space map of the (103) reflection for PLZT grown on STO-buffered Si(001) (grey) and PLZT grown on a single-crystal STO(001) substrate (black). The (103) reflection for the bulk STO substrate is also shown.

7.3.2 Film surface topography analysis

The RMS surface roughness of ~120 nm thick films of PLZT on STO-buffered Si(001), as obtained from 5 × 5 µm^2 AFM scans, is plotted as a function of substrate temperature in Figure 7.6. This data reveals that the PLZT surface roughness is strongly dependent on the substrate temperature during growth. A minimum surface roughness of ~1.0 nm is obtained for growth temperatures in the range ~500–540°C. The inset in Figure 7.6 shows a 5 × 5 µm^2 AFM scan for the surface of a PLZT epilayer grown on STO/Si(001) for a substrate temperature of ~520°C. This surface roughness is comparable to that of the STO/Si(001) substrate, with an RMS value measured at ~0.8 nm for a 10 × 10 µm^2 AFM scan. For temperatures above ~550°C, the film surface roughness increases, which could derive from depletion of Pb [8]. The surface roughness of the PLZT epilayer was not appreciably affected by introduction of an SRO bottom electrode layer, but was found to increase with the PLZT film thickness, e.g., the RMS surface roughness of PLZT layers with 520 nm thickness was measured at 4.5 nm. In comparison, the RMS surface roughness of ∼520 nm PLZT thin films deposited on HF-etched STO(001) substrate was measured at 2.3 nm [28]. Inspection of the PLZT film surface with scanning electron microscopy (SEM) showed uniform layers with no visible voids, pores, or cracks.

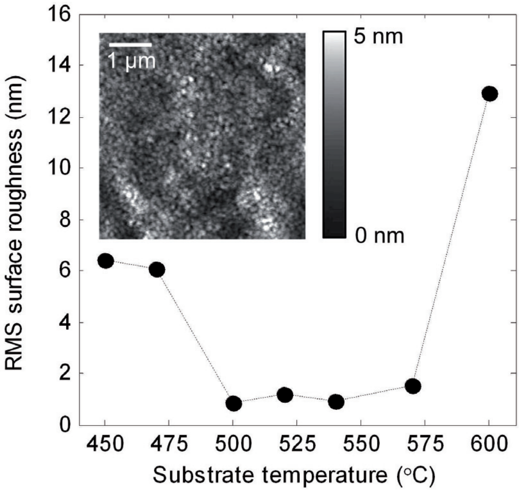

Figure 7.6: RMS surface roughness versus substrate temperature, as obtained from 5 × 5 µm^2 AFM scans on the PLZT/STO/Si(001) surface. The inset shows a 5 × 5 µm^2 scan of the PLZT surface for a 120 nm thick film grown at a substrate temperature of 520°C.

7.3.3 Electron spectroscopy analysis

XPS analysis of the STO/Si(001) and the HF-etched STO(001) substrates unveils some distinct differences between the two growth surfaces, apparent in the recorded oxygen and carbon core level spectra. Figure 7.7(a) shows the O 1s spectrum of the STO/Si(001) substrate, recorded in normal (solid curve) and oblique emission (TOA = 30°, dotted curve). The predominant peak at 529.4 eV is attributed to oxygen in the perovskite STO lattice. The high binding energy shoulder at ∼531.5 eV, which prevails in the spectrum recorded at oblique emission, appears to derive from carbonate impurities. This is concluded from the presence of a minor peak in the C 1s core level spectrum of this substrate at ∼290 eV binding energy, cf. Figure 7.7(b), which is a clear signature of carbonate.

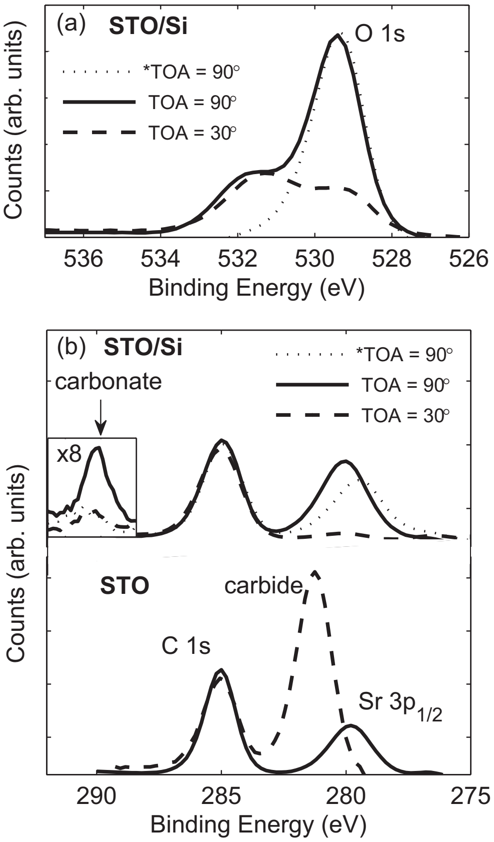

Figure 7.7: (a) O 1s core level spectra for STO/Si(001), recorded at photoemission take off angles (TOAs) of 30° and 90°. (b) C 1s core level spectra for STO/Si(001) and single-crystal STO(001) recorded at TOAs of 30° and 90°. The asterisks denote corresponding spectra after annealing at 600°C for 1 hour.

The C 1s spectra in Figure 7.7(b) are normalized to show identical count rates for emission from adventitious surface carbon at ∼285.0 eV binding energy. The high binding energy features in the O 1s and C 1s spectra both virtually disappear when the sample is annealed (dashed curves) for 1 hour at 600°C in ultra high vacuum ($\sim 10^{-9}$ Torr). Figure 7.7(b) also shows the corresponding C 1s spectrum for a HF-etched monocrystalline STO(001) substrate. The prominent, C 1s peak at ~281 eV in the STO spectrum (TOA = 30°) suggests the presence of superficial carbide, presumably TiC [29]. No signature of surface carbide was found in the C 1s spectrum of STO/Si(001). Conversely, no trace of carbonate was found in the XPS data from the HF-etched (TiO_2-terminated) STO(001) substrate. The integrated peak intensities of the Sr $3p_{3/2}$ and Ti $2p_{3/2}$ core level spectra show a noticeable enrichment of strontium at the surface of the STO/Si(001) substrate (Sr $3p_{3/2}$:Ti $2p_{3/2}$ peak intensity ratio = 1.55), compared to HF-etched single-crystal STO(001) (Sr $3p_{3/2}$:Ti $2p_{3/2}$ = 1.06). Annealing of the STO/Si(001) substrate had little impact on the measured Sr $3p_{3/2}$:Ti $2p_{3/2}$ peak intensity ratio, suggesting that the measured enrichment in Sr cannot be attributed to superficial $SrCO_3$ impurities [30]. Also, the recorded Sr 3d core level spectra of the STO/Si(001) substrates showed no chemical shift.

Figure 7.8(a) and (b) show composition depth profiles, recorded with Auger electron spectroscopy, of two 100 nm thick films of PLZT grown on Si(001) and STO-buffered Si(001), respectively. The two films were deposited in the same growth run, with a substrate temperature of 520°C. For the sample without an STO buffer layer (Figure 7.8(a)), the Auger depth profiles unveil noticeable interdiffusion of Si and PLZT cations at the film-substrate interface. Si is found to an approximate depth of 20 nm in the PLZT layer, whereas Pb cations diffuse ~30 nm into the Si substrate. In contrast, the depth profiles of the PLZT/STO/Si sample in Figure 7.8(b) show only negligible amounts of Si diffusion into the PLZT epilayer. Moreover, the concentration of Pb is slightly higher throughout the PLZT layer than that measured for the sample in Figure 7.8(a).

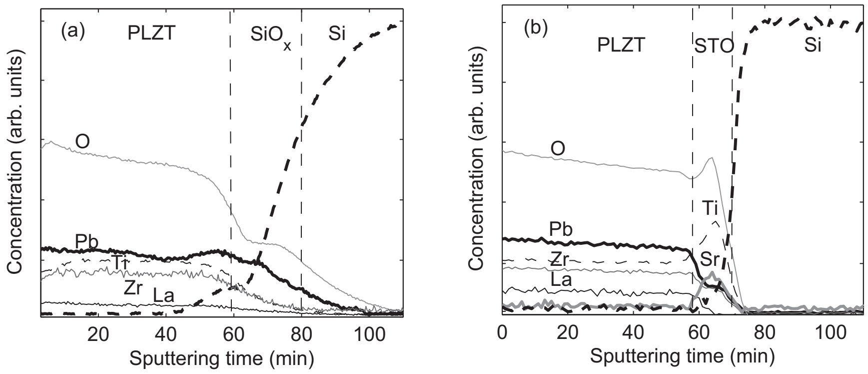

Figure 7.8: Auger depth profiles of a 100 nm thick PLZT thin film grown on (a) Si(001) and (b) STO/Si(001).

7.3.4 Ferroelectric and optical characterization

The room temperature ferroelectric response of a PLZT epilayer grown on SRO/STO/Si(001) is displayed in Figure 7.9. The recorded P–E loop exhibits a remanent polarization $P_{\mathrm{r}} \sim 40$ µC/cm^2 and coercive field $E_{\mathrm{c}} \sim 100$ kV/cm. The inset in Figure 7.9 shows the

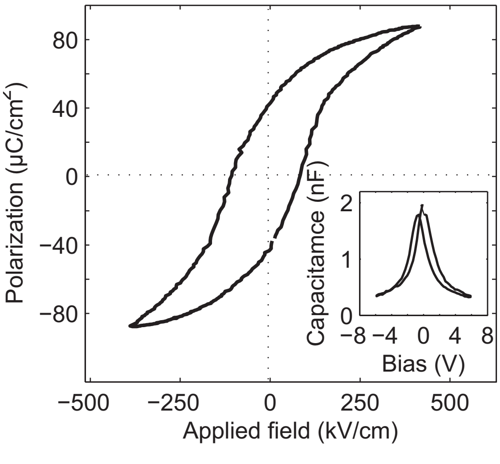

Figure 7.9: P–E hysteresis loop for a PLZT epilayer grown on SRO/STO/Si(001). The inset shows the measured C–V switching curve.

corresponding C–V switching curve for the PLZT layer.

Figure 7.10 shows the wavelength dispersion of the refractive index (n) and the extinction coefficient (k), as obtained from a numerical fit to spectroscopic ellipsometry data (Ψ, Δ) for PLZT grown on STO/Si(001). The optical constants were modeled using a Cauchy dispersion with an Urbach absorption tail [31]. The surface topography of the PLZT layer was modeled using the Bruggemann effective medium approximation [32]. The calculated dispersion curves in Figure 7.10 render a refractive index $n \sim 2.48$ for the PLZT epilayer at the main communication wavelength, $\lambda = 1550$ nm, in good agreement with the estimated refractive index for films grown on STO(001) and MgO(001) [28], and an extinction coefficient $k < 0.001$ for $\lambda > 650$ nm, in keeping with the k vs. λ dispersions previously reported for PLZT films [31, 33, 34].

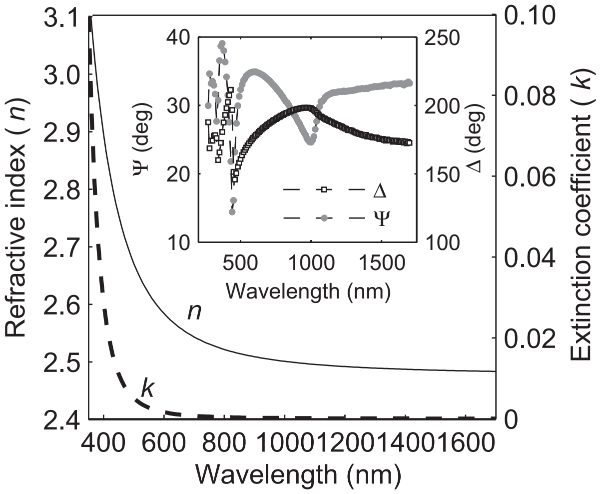

Figure 7.10: Calculated dispersion of the refractive index n and extinction coefficient k for a PLZT thin film on STO-buffered Si(001). The inset shows the recorded spectroscopic ellipsometry data (Ψ, Δ) for a ~117 nm thick PLZT epilayer.

7.4 Discussion

It is established from the XRD analysis that the sputter-deposited PLZT thin films are epitaxial, with their in-plane low-index crystalline axes aligned with those of the STO buffer layer. The ∼4.09 ±0.01 Å *c*-axis lattice constant measured for films grown at the optimum substrate temperature of 520°C compares to 4.126 Å for films grown on single-crystal STO(001) [28] and to 4.074 Å [14] for unstrained bulk $Pb_{0.92}La_{0.08}Zr_{0.4}Ti_{0.6}O_3$. The distinct shift in reciprocal lattice parameter of the PLZT(103) reflection in Figure 7.5 is evidence of a smaller unit cell tetragonality for PLZT thin films deposited on STO/Si(001), $c/a = 1.014$, compared to that for films grown on single-crystal STO(001) substrates, $c/a = 1.026$. The rocking curve FWHM of the PLZT(001) reflection for films grown at the optimum substrate temperature of ∼520°C is $\Delta\omega \sim 0.3°$, comparable to that previously reported for sputter-deposited PLZT on CeO_2/YSZ-buffered Si(001) [8], but larger than for films grown on STO(001), $\Delta\omega \sim 0.03°$ [28]. This goes to show that the crystalline perfection of the PLZT epilayers grown on STO-buffered silicon does not quite match that of films grown on HF-etched monocrystalline STO(001). This may be explained by the presence of excess strontium at the substrate surface. The lower Sr $3p_{3/2}$:Ti $2p_{3/2}$ XPS core level peak intensity ratio measured for HF-etched STO(001) is not unexpected, since this substrate is TiO_2-terminated [35]. From a simple model calculation, assuming an STO buffer layer composed of alternate layers with SrO and TiO_2, each half a unit cell thick, the thickness of the Sr-rich termination layer for the STO/Si(001) substrate was estimated at ∼2.5 Å.

For PLZT grown on Si(001) without the STO buffer layer, XRD measurements show that the thin film growth is deranged by formation of a pyrochlore phase, which adversely affects the ferroelectric and optical properties of the PLZT thin films [36, 37]. Moreover, diffusion of PLZT cations into the Si substrate may be detrimental to the performance of integrated silicon-based electronic devices and circuits [38]. Comparison of the Auger depth profiles for films grown directly on Si(001), Figure 7.8(a), and on STO/Si(001), Figure 7.8(b), shows that this ∼8 nm thick STO buffer layer serves as an effective barrier to diffusion of Pb into the semiconductor substrate, thus suppressing formation of the pyrochlore phase [39]. This result is in agreement with previous Auger depth profiles of Pb(Zr,Ti)O_3 gate oxides on STO/Si(001) [40]. Moreover, waveguide device applications place strict requirements on material uniformity in order to ensure homogeneous physical properties and prevent optical scattering from local variations in composition [41]. The recorded depth profiles in Figure 7.8(b) indicate good composition uniformity throughout the PLZT epilayer.

The ferroelectric measurements confirm that PLZT(001) epilayers with the selected composition, integrated on silicon, exhibit a ferroelectric response with high remanent polarization and a large coercive field. The measured values for P_r and E_c are actually larger than those previously reported for $Pb_{0.92}La_{0.08}Zr_{0.4}Ti_{0.6}O_3$ bulk crystals [14] and thin films [28, 42]. The refractive index obtained for the PLZT epilayer suggests sputter-deposited thin films with a high density [43], and the sharp drop of the extinction coefficient with increasing wavelength implies low optical absorption in the near infrared range [44]. The somewhat inferior crystalline quality of PLZT grown on STO-buffered silicon, compared to those grown on single-crystal STO(001) substrate, thus appears to have little impact on the ferroelectric response and the refractive index [28].

The surface roughness of the ∼500 nm PLZT epilayers on STO-buffered Si(001) (RMS ∼ 4.5 nm) is comparable to that measured for films grown on CeO2/YSZ-buffered Si(001) (RMS ∼ 4.1 nm) [8]. These values for the surface roughness exceed those recorded for films of comparable thickness grown on STO(001) and MgO(001) (RMS ∼ 2.3 nm) [28]. However, an RMS surface roughness of ∼4–5 nm remains within the confines required for low-loss wave propagation, which suggests that the films grown on STO/Si(001) are fit for integrated electro-optic device applications. The [001] crystalline orientation of PLZT in combination with the planar electrode geometry, offered by epitaxial integration of an SRO bottom electrode, implies that high electric fields can be applied along the optical axis of the PLZT thin film. This device configuration provides for strong electro-optic coupling, which is highly desirable for device miniaturization, i.e., it reduces the required interaction length [45].

7.5 Conclusions

Monocrystalline perovskite PLZT thin films were grown on STO-buffered Si(001) substrate by on-axis RF magnetron sputtering. Epitaxial growth of the tetragonal phase with excellent in-plane alignment was confirmed. Composition depth profiles recorded with Auger electron spectroscopy demonstrate good composition uniformity throughout the film and show that the STO buffer layer serves as an effective diffusion barrier against interdiffusion of Pb and Si. Films of several hundred nm thickness exhibit an RMS surface roughness less than 5 nm, thus satisfying the requirements for low-loss light propagation. A strong ferroelectric response combined with a high refractive index, low absorption for near infrared wavelengths, and a smooth film surface open up perspectives for potential applications of these Si-integrated PLZT epilayers, ranging from nonvolatile memory and nano-electro-mechanical systems (NEMS) to integrated electro-optic devices.

References

[1] Scott, J. F., and Araujo, C. A., "Ferroelectric memories," *Science*, vol. 246, pp. 1400–1405, 1989.

[2] Francombe, M. H., "The research status and device potential of ferroelectric thin films," *Ferroelectrics*, vol. 3, pp. 199–211, 1972.

[3] Ramesh, R., Aggarwal, S., and Auciello, O., "Science and technology of ferroelectric films and heterostructures for non-volatile ferroelectric memories," *Mater. Sci. Eng.*, vol. 32, pp. 191–236, 2001.

[4] Nordseth, Ø., Kjellman, J. Ø., You, C. C., Røyset, A., Tybell, T., and Grepstad, J. K., "The case for electro-optic waveguide devices from ferroelectric (Pb,La)(Zr,Ti)O_3 thin film epilayers," *Proc. of SPIE*, vol. 7381, p. 73810F, 2009.

[5] Lichtensteiger, C., Triscone, J. M., Junquera, J., and Ghosez, P., “Ferroelectricity and tetragonality in ultrathin $PbTiO_3$ films,” *Phys. Rev. Lett.*, vol. 94, p. 047603, 2005.

[6] Paruch, P., and Triscone, J. M., “High-temperature ferroelectric domain stability in epitaxial $PbZr_{0.2}Ti_{0.8}O_3$ thin films,” *Appl. Phys. Lett.*, vol. 88, p. 162907, 2006.

[7] Dawber, M., Stucki, N., Lichtensteiger, C., Gariglio, S., Ghosez, P., and Triscone, J. M., “Tailoring the properties of artificially layered ferroelectric superlattices,” *Adv. Mater.*, vol. 19, pp. 4153–4159, 2007.

[8] Nordseth, Ø., Tybell, T., and Grepstad, J. K., “Epitaxial $(Pb,La)(Zr,Ti)O_3$ thin films on buffered Si(100) by on-axis radio frequency magnetron sputtering,” *Thin Solid Films*, vol. 517, pp. 2623–2626, 2009.

[9] McKee, R. A., Walker, F. J., and Chisholm, M. F., “Crystalline oxides on silicon: The first five monolayers,” *Phys. Rev. Lett.*, vol. 81, pp. 3014–3017, 1998.

[10] Lin, A., Hong, X., Wood, V., Verevkin, A. A., Ahn, C. H., McKee, R. A., Walker, F. J., and Specht, F. D., “Epitaxial growth of $Pb(Zr_{0.2}Ti_{0.8})O_3$ on Si and its nanoscale piezoelectric properties,” *Appl. Phys. Lett.*, vol. 78, pp. 2034–2036, 2001.

[11] Yu, Z., Ramdani, J., Curless, J. A., Finder, J. M., Overgaard, C. D., Droopad, R., Eisenbeiser, K. W., Hallmark, J. A., Ooms, W. J., Conner, J. R., and Kaushik, V. S., “Epitaxial perovskite thin films grown on silicon by molecular beam epitaxy,” *J. Vac. Sci. Technol. B*, vol. 18, pp. 1653–1657, 2000.

[12] Tambo, T., Nakamura, T., Maeda, K., Ueba, H., and Tatsuyama, C., “Molecular beam epitaxy of $SrTiO_3$ films on Si(100)-2×1 with SrO buffer layer,” *Jpn. J. Appl. Phys.*, vol. 37, pp. 4454–4459, 1998.

[13] Tokumitsu, E., Itani, K., Moon, B. K., and Ishiwara, H., "Crystalline quality and electrical properties of $PbZr_xTi_{1-x}O_3$ thin films prepared on $SrTiO_3$-covered Si substrates," *Jpn. J. Appl. Phys.*, vol. 34, pp. 5202–5206, 1995.

[14] Haertling, G. H., and Land, C. E., "Hot pressed $(Pb,La)(Zr,Ti)O_3$ ferroelectric ceramics for electrooptic applications," *J. Am. Ceram. Soc.*, vol. 54, pp. 1–11, 1971.

[15] Haertling, G. H., "PLZT electrooptic materials and applications – a review," *Ferroelectrics*, vol. 75, pp. 25–55, 1987.

[16] Lee, S.-H., Noh, T. W., and Lee, J.-H., "Control of epitaxial growth of pulsed laser deposited $LiNbO_3$ films and their electro-optic effects," *Appl. Phys. Lett.*, vol. 68, pp. 472–474, 1996.

[17] Lu, Y., Zheng, J., Golomb, M. C., Wang, F., Jiang, H., and Zhao, J., "In-plane electro-optic anisotropy of $(1-x)Pb(Mg_{1/3}Nb_{2/3})O_3$-$xPbTiO_3$ thin films grown on (100)-cut $LaAlO_3$," *Appl. Phys. Lett.*, vol. 74, pp. 3764–3766, 1999.

[18] Leng, W., Yang, C., Ji, H., Zhang, J., Tang, J., Chen, H., and Gao, L., "Linear and nonlinear optical properties of $(Pb,La)(Zr,Ti)O_3$ ferroelectric thin films grown by radio-frequency magnetron sputtering," *J. Phys. D: Appl. Phys.*, vol. 40, pp. 1206–1210, 2007.

[19] Wessels, B. W., Nystrom, M. J., Chen, J., Studebaker, D., and Marks, T. J., "Epitaxial niobate thin films and their nonlinear optical properties," *Mater. Res. Soc. Symp. Proc.*, vol. 401, pp. 211–218, 1996.

[20] Reiner, J. W., Garrity, K. F., Walker, F. J., Ismail-Beigi, S., and Ahn, C. H., "Role of strontium in oxide epitaxy on silicon (001)," *Phys. Rev. Lett.*, vol. 101, p. 105503, 2008.

[21] Nordseth, Ø., Tybell, T., and Grepstad, J. K., "Simulation of photonic band gap waveguides in lead-lanthanum

zirconate-titanate, in: 2006 Northern Optics Conference Proceedings," pp. 51–54, 2006.

[22] Triscone, J.-M., Frauchiger, L., Decroux, M., Mieville, L., Fischer, Ø., Beeli, C., Stadelmann, P., and Racine, G.-A., "Growth and structural properties of epitaxial Pb(Zr_xTi_{1-x})O_3 films and Pb(Zr_xTi_{1-x})O_3-cuprate heterostructures," *J. Appl. Phys.*, vol. 79, pp. 4298–4305, 1996.

[23] *Casa Software Ltd.* http://www.casaxps.com.

[24] Sekine, T., Nagasawa, Y., Kudoh, M., Sakai, Y., Parkes, A. S., Geller, J. D., Mogami, A., and Hirata, K., *Handbook of Auger Electron Spectroscopy.* Tokyo: JEOL Ltd., 1982.

[25] *WVASE32 Software.* ver. 3.668, J. A. Woollam Co.

[26] Thompson, C., Foster, C. M., Eastman, J. A., and Stephenson, G. B., "Observation of the polarization of domains in ferroelectric thin films using x-ray interference," *Appl. Phys. Lett.*, vol. 71, pp. 3516–3518, 1997.

[27] Mori, H., and Ishiwara, H., "Epitaxial growth of $SrTiO_3$ films on Si(100) substrates using a focused electron beam evaporation method," *Jpn. J. Appl. Phys.*, vol. 30, pp. L1415–L1417, 1991.

[28] Nordseth, Ø., Røyset, A., Tybell, T., and Grepstad, J. K., "Sputter-deposited (Pb,La)(Zr,Ti)O_3 thin films: Effect of substrate and optical properties," *J. Vac. Sci. Technol. A*, vol. 27, pp. 548–553, 2009.

[29] Santerre, F., Khakini, M. A. E., Chaker, M., and Dodelet, J. P., "Properties of TiC thin films grown by pulsed laser deposition," *Appl. Surf. Sci.*, vol. 148, pp. 24–33, 1999.

[30] Bhaskar, S., Allgeyer, D., and Smythe, J. A., "Depth profiling of dielectric $SrTiO_3$ thin films by angle-resolved x-ray photoelectron spectroscopy," *Appl. Phys. Lett.*, vol. 89, p. 254103, 2006.

[31] Tang, X. G., Liu, Q. X., Jiang, L. L., and Ding, A. L., "Optical properties of $Pb(Zr_xTi_{1-x})O_3$ ($x = 0.4, 0.6$) thin films on Pt-coated Si substrates studied by spectroscopic ellipsometry," *Mater. Chem. Phys.*, vol. 103, pp. 329–333, 2007.

[32] Bruggemann, D. A. G., "The calculation of various physical constants of heterogeneous substances. I. The dielectric constants and conductivities of mixtures composed of isotropic substances," *Ann. Phys.*, vol. 24, pp. 636–664, 1935.

[33] Kao, J. S., Tsai, C. H., Jamn, G., Liu, K. S., and Lin, I. N., "Crystalline and optical properties of PLZT films prepared by pulsed laser deposition," *Integr. Ferroelectr.*, vol. 31, pp. 69–75, 2000.

[34] Echizen, M., Nishida, T., Nozaka, T., Takeda, H., Uchiyama, K., and Shiosaki, T., "Preparation of $(Pb,La)(Zr,Ti)O_3$ epitaxial thin films by modified sol-gel method and their crystallinity evaluation," *Jpn. J. Appl. Phys.*, vol. 46, pp. 6933–6937, 2007.

[35] Baniecki, J. D., Ishii, M., Kurihara, K., Yamanaka, K., Yano, T., Shinozaki, K., Imada, T., Nozaki, K., and Kin, N., "Photoemission and quantum chemical study of $SrTiO_3(001)$ surfaces and their interaction with CO_2," *Phys. Rev. B*, vol. 78, p. 195415, 2008.

[36] Nakagawa, T., Yamaguchi, J., Usuki, T., Matsui, Y., Okuyama, M., and Hamakawa, Y., "Ferroelectric properties of rf sputtered PLZT thin film," *Jpn. J. Appl. Phys.*, vol. 18, pp. 897–902, 1979.

[37] Tunaboylu, B., Ozkan, C. S., Ata, A., Ring, K., and Esener, S., "Phase transformation and paired-plate precipitate formation in $Pb_{0.91}La_{0.09}Zr_{0.65}Ti_{0.35}O_3$ films grown on sapphire substrates," *Mat. Sci. Semicond. Proc.*, vol. 5, pp. 199–206, 2003.

[38] Tokumitsu, E., Itani, K., Moon, B. K., and Ishiwara, H., "Preparation of $PbZr_xTi_{1-x}O_3$ films on Si substrates using

$SrTiO_3$ buffer layers," *Proc. Mater. Res. Soc. Symp.*, vol. 361, pp. 427–432, 1995.

[39] Shichi, Y., Tanimoto, S., Goto, T., Kuroiwa, K., and Tarui, Y., "Interaction of $PbTiO_3$ films with Si substrate," *Jpn. J. Appl. Phys.*, vol. 33, pp. 5172–5177, 1994.

[40] Shin, D. S., Park, S. T., Choi, H. S., Choia, I. H., and Lee, J. Y., "Characteristics of $Pt/SrTiO_3/Pb(Zr_{0.52},Ti_{0.48})O_3/SrTiO_3/Si$ ferroelectric gate oxide structure," *Thin Solid Films*, vol. 354, pp. 251–255, 1999.

[41] Nakada, M., Ohashi, K., and Akedo, J., "Optical and electro-optical properties of $Pb(Zr,Ti)O_3$ and $(Pb,La)(Zr,Ti)O_3$ films prepared by aerosol deposition method," *J. Cryst. Growth*, vol. 275, pp. 1275–1280, 2005.

[42] Kobune, M., Matsuura, O., Matsuzaki, T., Sawada, T., Fujisawa, H., Shimizu, M., Niu, H., and Honda, K., "Microstructure and electrical properties of $(Pb,La)(Zr,Ti)O_3$ films crystallized from amorphous state by two-step postdeposition annealing," *Jpn. J. Appl. Phys.*, vol. 40, pp. 5554–5558, 2001.

[43] Khawaja, E. E., Durrani, S. M. A., Hallak, A. B., Salim, M. A., and Hussain, M. S., "Density of thin vapour-deposited films of zinc selenide," *J. Phys. D: Appl. Phys.*, vol. 27, no. 1008–1013, 1994.

[44] Li, H., Zhang, Y., Wen, J., Yang, S., Mo, D., Cheng, C. H., Xu, Y., and Meckenzie, J. D., "Optical properties of lead lanthanum zirconate titanate amorphous ferroelectric-like thin films," *Jpn. J. Appl. Phys.*, vol. 39, pp. 1180–1183, 2000.

[45] Petraru, A., Schubert, J., Schmid, M., and Buchal, C., "Ferroelectric $BaTiO_3$ thin-film optical waveguide modulators," *Appl. Phys. Lett.*, vol. 81, pp. 1375–1377, 2002.

Chapter 8

Simulation of photonic band gap waveguides in lead-lanthanum zirconate-titanate

NORDSETH, Ø., TYBELL, T., AND GREPSTAD, J. K., *2006 Northern Optics Conference Proceedings*, pp. 51–54, Bergen, Norway, 14–16 June 2006.

Abstract: Simulations of photonic crystals slabs (PCSs) in thin films of lead-lanthanum zirconate-titanate (PLZT) show band gaps larger than 27 % of the mid-gap frequency for a hexagonal hole-type photonic crystal. The vertical asymmetry caused by the introduction of electrode and buffer layers in a thin film stack, required for epitaxial growth on silicon, does not appreciably affect the photonic crystal properties. Waveguides can be formed in the PCS by removing rows of holes from the crystal lattice. We find that the propagation losses in such waveguide are strongly affected by the thickness and optical attenuation coefficient of the electrode layer, and that the transmission through a 60 degree waveguide bend can be substantially increased by introduction of additional defects.

8.1 Introduction

Recent progress in combining ferroelectric perovskites and conventional semiconductors epitaxially renders feasible the incorporation of such materials in silicon-based nano-electronics and photonic device applications. Thin films of the ferroelectric perovskite lead-lanthanum zirconate-titanate (PLZT) features a number of properties attractive to integrated optics, such as a high electro-optic coefficient and propagation losses of less than 1 dB/cm at infrared frequencies [1–3]. Photonic band gap (PBG) waveguides may be fabricated in a hole-type photonic crystal slab (PCS) by introducing line defects in the periodic lattice [4]. Such waveguides have attracted noticeable attention over the last decade, mainly for their capability to guide light through sharp bends with low losses [5, 6].

8.2 Photonic crystal slab design and photonic band gaps

The simulations reported in this section pertain to PCSs (PCSs), defined in a multilayered thin film structure of (001)-oriented PLZT grown epitaxially on strontium ruthenate (SRO), serving as the metallic electrode for polarization of the PLZT layer, and cerium oxide and yttria-stabilized zirconia (YSZ) buffer layers, required for the epitaxial growth of perovskites on a silicon wafer [7]. Figure 8.1 depicts this multilayer thin film structure.

In order to design photonic crystals and waveguides in this thin film structure, numerical simulations of the photonic band structure were performed by computing the eigenmodes of the periodic dielectric system, assuming a linear, time invariant, lossless dielectric medium. To this end, a full vector 3D frequency-domain (FD) method, based on a preconditioned block-iterative solution of the Maxwell equations in a plane wave basis [8], was used. In order to compute the dispersion characteristics of the line-defect waveguide, a supercell approach was adopted. The extension of the supercell in the y-direction was set to 7 periods, where one period corresponds to $a\sqrt{3}/2$, whereas the extension of the air background above and

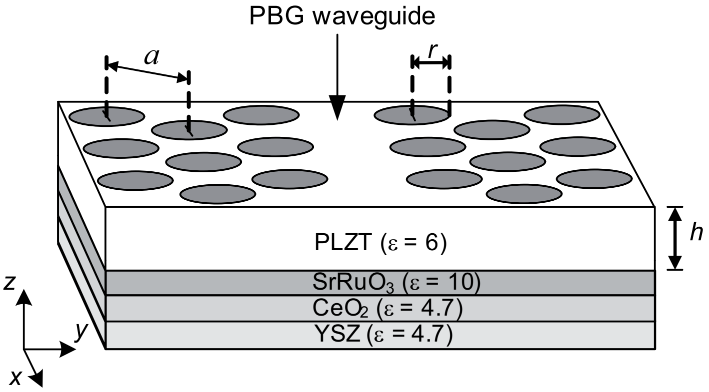

Figure 8.1: Photonic band gap waveguide in a PLZT photonic crystal slab with SRO electrode and CeO_2*, YSZ buffer layers, required for epitaxial growth on silicon. h, a, and r are slab thickness, lattice constant, and hole radius, respectively.*

below the slab was set to $2a$. Mode propagation and transmission data were calculated using 3D finite-difference time-domain (FDTD) algorithms, with perfectly matched layers employed as the absorbing boundary condition to terminate the computational domain. A Gaussian pulse was adopted for excitation of transverse electric (TE) polarized light. The computational resolution was 32 points per lattice constant.[1]

The principal design parameters for a hole-type PCS are the thickness and dielectric constant of the slab materials, as well as hole radius and lattice configuration. Initial simulations showed that for a slab with dielectric constant $\varepsilon = 6$, the appropriate value for PLZT at infrared frequencies, a hexagonal lattice of holes result in larger PBGs compared to a square lattice. Therefore, the hexagonal lattice was implemented in the analytical study presented in the following. First, a symmetric PCS is considered, i.e., a slab without the vertical asymmetry introduced by the metallic SRO and the dielectric CeO_2 and YSZ buffer layers. Figure 8.2 shows the size of the largest

---

[1] A detailed description of the computational techniques is provided in Appendix D

band gap in percent of the mid-gap frequency, versus slab thickness for various hole radii of a PLZT PCS suspended in air. The graphs pertain to a hexagonal hole lattice. A band gap larger than 27 % was obtained for a slab thickness of $0.8a$ and hole radius of $0.38a$, where a is the lattice constant of the PCS. For a slab with excessive thickness, i.e. $h > 0.8a$, there is a small energy barrier for higher-order modes to form via a horizontal nodal planes. These modes may populate the band gap, resulting in a reduced or completely closed gap. Moreover, a slab with insufficient thickness will not be able to provide strong confinement for the fundamental mode, with the outcome that the periodicity of the 2D lattice becomes insignificant [9].

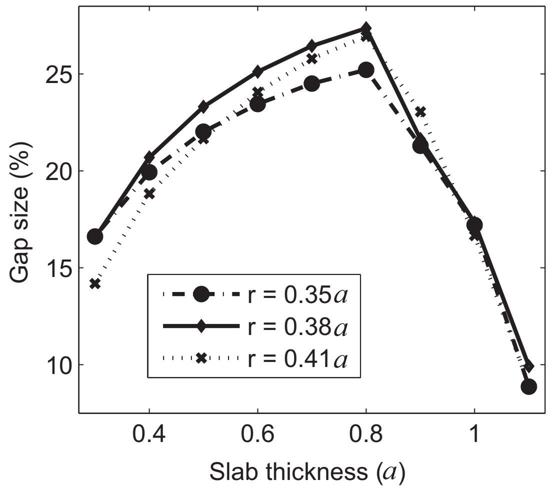

Figure 8.2: The largest band gap in even (TE-like) modes versus slab thickness for various hole radii. The maximum gap is obtained for a slab thickness of 0.8a and hole radius of 0.38a.

The photonic band diagram in Figure 8.3 displays the guided even (TE-like) and odd (TM-like) modes of the PLZT PCS, optimized with respect to the size of the band gap, i.e., a slab of thickness $0.80a$ and hole radius of $0.38a$. The largest band gap is found between the first and second even mode bands, marked with grey shading in Figure 8.3. It has a mid-gap frequency of $0.43c_0/a$, where c_0 is the speed of light in vacuum. Conversely, a lattice constant of

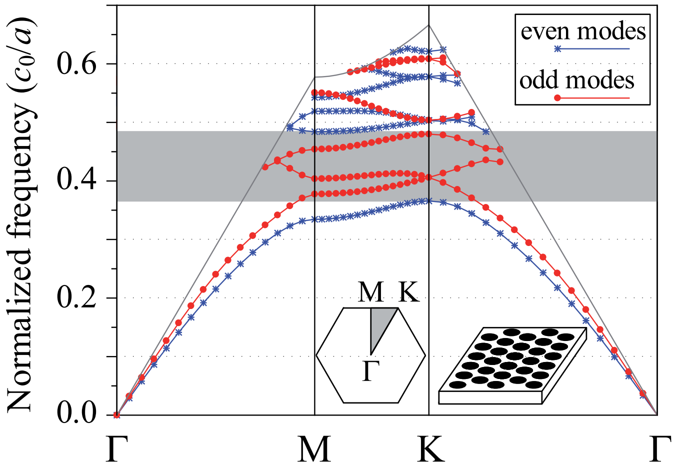

Figure 8.3: Photonic band diagram for a symmetric PLZT PCS, showing the frequency dispersions of even (TE-like) and odd (TM-like) propagating modes for low-index symmetry axes of the 2D Brillouin zone of a hexagonal, hole-type lattice. The mid-gap frequency of the largest band gap (shaded in grey) is 0.43c_0/a.

$a = 0.43\lambda_0$ places the corresponding wavelength (λ_0) in the middle of this band gap. There are additional (minor) gaps in this photonic band structure for both even and odd modes. However, none of these overlap in frequency. For comparison, the maximum band gap obtained for a PLZT PCS with a square lattice of holes was found to be approximately 15 %, cf. Figure 8.4.

The photonic band diagram of the asymmetric PCS shown in Figure 8.1 was calculated and compared to that of the symmetric PLZT PCS. The frequency band dispersions of the asymmetric slab, with metallic electrode and dielectric buffer layers, are shown in Figure 8.5, along with the even and odd mode bands of the symmetric PLZT PCS (cf. Figure 8.3). In these calculations, the dielectric losses in the thin film layers were disregarded. The dielectric constant was set at $\varepsilon = 10$ and 4.7 for the SRO and the two dielectric buffer layers, respectively, their appropriate values at infrared frequencies [10], [11]. The layer thicknesses were 0.71a for PLZT, 0.05a for SRO, and 0.02a for the CeO_2 and YSZ buffer layers, adding up to an overall

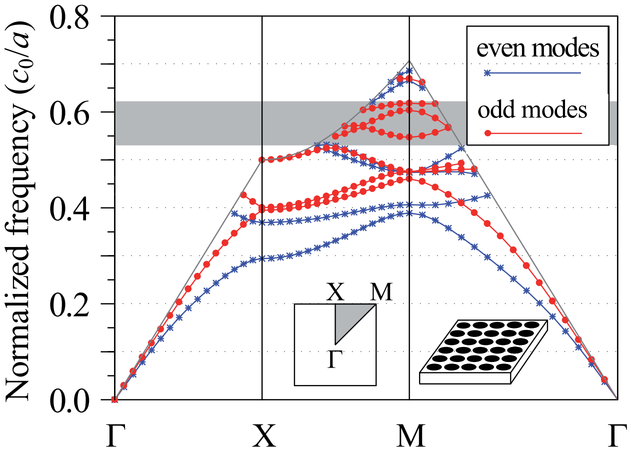

Figure 8.4: Photonic band diagram for a symmetric PLZT PCS, showing the frequency dispersions of even (TE-like) and odd (TM-like) propagating modes for low-index symmetry axes of the 2D Brillouin zone of a square, hole-type lattice. For a slab thickness 0.50a and hole radius 0.30a, the mid-gap frequency of the largest even mode band gap (shaded in grey) is $0.58c_0/a$.

film thickness of $0.80a$. The holes defining the translation symmetry of the PCS were extended through the full stack of the multilayer.

The band diagram in Figure 8.5 shows that the guided modes of the PCS are shifted only slightly in frequency by introduction of the metallic electrode and the two dielectric buffer layers. The modes become hybridized however, which perturbs the characteristic transmission properties of the PCS [9], since there are no longer genuine band gaps for even and odd modes. Still, the FDTD simulations presented in the following show that introduction of vertical asymmetry in the thin film slab has little impact on the optical transmission properties, compared to the symmetric slab. An effective PBG is still present and waveguiding thus remains possible with the asymmetric PCS.

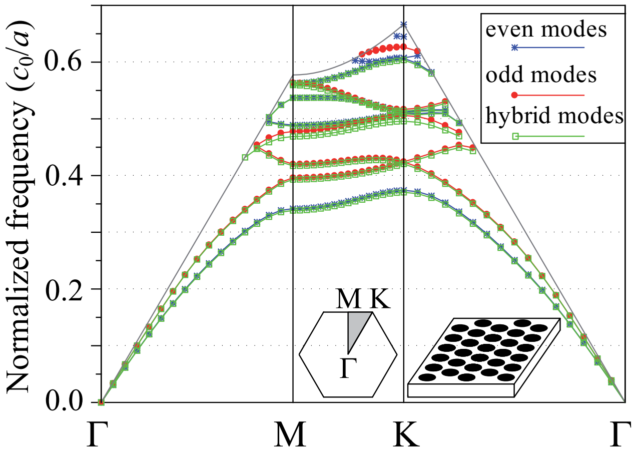

Figure 8.5: Photonic band diagram of the asymmetric PLZT PCS, including metal electrode and buffer layers. Also shown are the even and odd modes of the symmetric PCS. The propagating modes of the asymmetric PCS structure become hybridized.

8.3 Photonic band gap waveguiding and light propagation

Rows of adjacent (nearest neighbor) holes in the PCS were removed to form a linear PBG waveguide in the (10)-direction of the 2D crystal lattice. Figure 8.6 shows the even mode frequency dispersions of the PLZT PCS projected onto the Γ–K direction of the corresponding 2D reciprocal lattice [12], along with guided even modes (green diamonds) for frequencies in the PCS band gap, assuming a symmetric slab. In the vertical direction, the guided modes are confined to the thin film waveguide by index guiding. We note that the PBG waveguide is multi-mode. However, the guided bands do not overlap in frequency. Thus, the waveguide can remain single-mode when operating in a narrow band of frequencies.

The propagation characteristics of the PBG waveguide for the asymmetric PLZT PCS were computed using FDTD analysis. In these simulations, optical absorption in the metallic SRO layer is accounted for by introduction of an attenuation coefficient, α, which

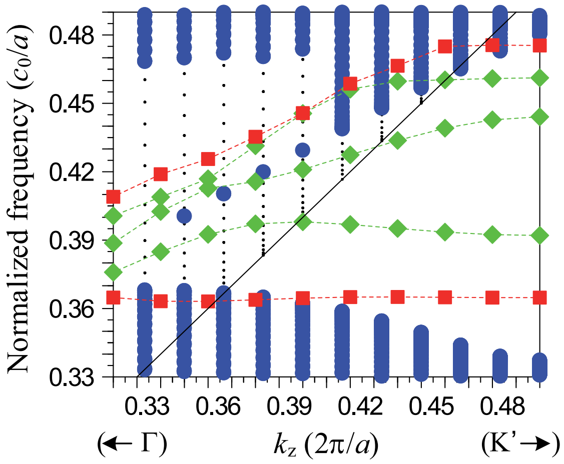

Figure 8.6: Frequency dispersions for the even (TE-like) modes of the symmetric PLZT PCS projected onto the Γ–K direction of the 2D reciprocal lattice (blue circles). Three modes supported by the waveguide (green diamonds) fall inside the gap in the projected bands for all k_z and are thus guided. The straight solid line shows the dielectric continuum light cone.

can be derived from the simple relation between α and the optical skin depth,

$$\delta = \frac{1}{\alpha} = \sqrt{\frac{2}{\omega\mu_0\sigma}} \tag{8.1}$$

where $\omega = 2\pi f$ is the angular frequency, σ is the electrical conductivity, and μ_0 is the magnetic permeability of vacuum [13]. The conductivity of SRO at optical frequencies can be assessed at $\sigma = 1 \times 10^3 - 5 \times 10^3\ \Omega^{-1}\text{cm}^{-1}$ [10, 14]. The corresponding attenuation coefficient α was estimated at $8.7 \times 10^4 - 2.0 \times 10^5$ cm^{-1}. This estimate seems reasonable, when compared to tabulated values of α for excellent conductors such as gold, platinum and silver, which all have attenuation coefficients in the range $5 \times 10^5 - 8 \times 10^5$ cm^{-1} at optical frequencies.

Table 8.1 summarizes the attenuation of $\lambda_0 = 1.55$ µm optical pulses propagated through a straight PBG waveguide. Intrinsic losses in the PLZT thin film, estimated at 1 dB/cm [1, 2] have no appreciable impact on this data. Such losses, as well as losses in the

Table 8.1: Propagation losses in a photonic band gap waveguide for different electrode thicknesses and attenuation coefficients.

Thickness (nm)	Waveguide attenuation (dB/µm)			
	α=3×10^4 cm^{-1}	α=1×10^5 cm^{-1}	α=5×10^5 cm^{-1}	α=1×10^6 cm^{-1}
0	0.038	0.038	0.038	0.038
20	0.273	0.966	0.978	0.501
40	0.673	2.085	0.875	0.471
60	1.295	3.033	0.811	0.463
80	2.231	3.466	0.783	0.462
100	3.494	3.436	0.770	0.462

dielectric buffer layers, were thus ignored in the present simulations. The table shows calculated propagation losses for various attenuation coefficients and thicknesses of the SRO electrode layer. With no metallic electrode incorporated in the PCS structure and all dielectric layers assumed to be lossless, a propagation loss of 0.038 dB/µm was obtained for this waveguide. The data show that the thin film thickness dependence of the propagation losses is more prominent at low attenuation coefficients, $\alpha < 5 \times 10^5$ cm^{-1}. For higher attenuation coefficients, the propagation losses in the waveguide decrease and become less dependent on the electrode layer thickness. This is due to the reduced penetration depth of the metal electrode. For a moderately good conductor such as SRO, we should thus keep the electrode layer at minimum thickness. Experiments suggest that the thickness of the SRO electrode layer must be on the order of 20–30 nm to ensure adequate conduction properties [15].

Figure 8.7 shows the photon flux distribution in the vertical cross-section of a PBG waveguide for different attenuation coefficients α of a metallic electrode with thickness $t = 100$ nm. The PLZT and dielectric buffer layers were assumed to be lossless. When the attenuation coefficient is less than 5×10^5 cm^{-1}, an increasing portion of the total flux passes through the metallic electrode layer, which leads to reduced waveguide transmittance. The simulated flux distributions in Figure 8.7 attest to the importance of a thin electrode layer in the actual PCS thin film stack.

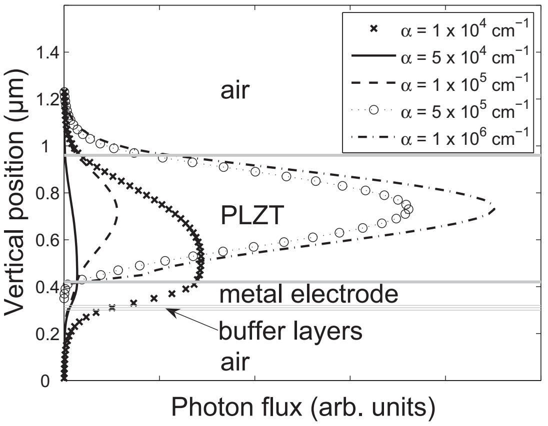

Figure 8.7: Calculated flux distribution in the vertical cross-section of a PBG waveguide for various attenuation coefficients α of the metallic electrode layer. The thickness of this layer was fixed at 100 nm. The horizontal lines indicate the vertical extension of the individual layers of the PCS thin film stack.

Figure 8.8 displays the propagation of a continuous wave of $\lambda_0 = 1.55$ μm coupled into a PBG waveguide with two 60 degree bends, defined in the asymmetric PLZT PCS. In these simulations, all materials, including the electrode layer, were assumed to be lossless. At this wavelength, the PBG is maximum for a lattice constant $a = 0.43\lambda_0 = 666$ nm, which implies an optimal thickness for the PCS of 533 nm with a hole radius of 253 nm for the hexagonal crystal lattice. Figure 8.8 (a) shows that the intensity of the guided wave drops sharply at the first bend, due to strong reflection.

The simulations show that less than 1 % of the incident optical power is transmitted at the far end. The transmission through the waveguide bends can be substantially improved by introduction of additional defects, i.e., holes with a radius $r_{\mathrm{def}} = 275$ nm positioned as depicted in Figure 8.8(b). The optical transmittance of this waveguide is approximately 70 % of the input power, an increase by a factor close to 80, compared to the waveguide in Figure 8.8(a).

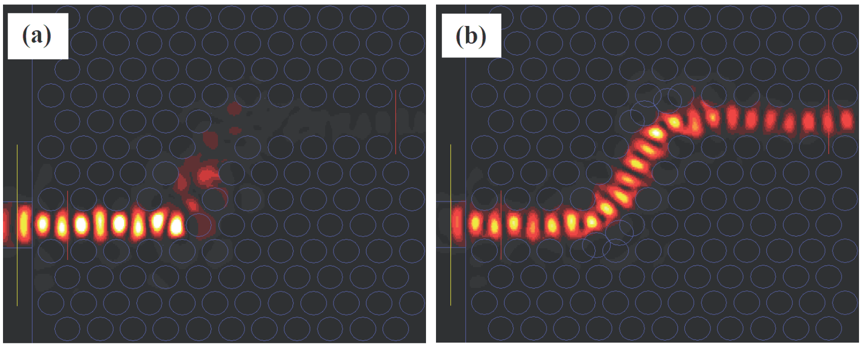

Figure 8.8: Optical transmission through a PBG waveguide with two 60 degree bends. The materials of the asymmetric PLZT PCS are assumed to be lossless. (a) Most of the energy is reflected at the waveguide bends. (b) Defects (added holes) at the waveguide bends substantially improve the transmission through the bends compared to the waveguide shown in (a).

8.4 Conclusion

The simulations show that large photonic band gaps can be obtained in photonic crystals of PLZT thin films perforated in a hexagonal lattice configuration. Optical waveguides can be realized in these PCSs by removing rows of holes from the hexagonal 2D lattice. Waveguide propagation losses for an asymmetric PCS with a metallic electrode layer are strongly dependent on the thickness and the attenuation coefficient of this layer. The transmission through 60 degree waveguide bends can be improved by introduction of added defects. The simulations reported in this work demonstrate that there is a case for ferroelectric perovskite PLZT in PCS applications.

References

[1] Nashimoto, K., Moriyama, H., Nakamura, S., Watanabe, M., Morikawa, T., Osakabe, E., and Haga, K., "PLZT electro-optic waveguides and switches," *Optical Fiber*

Communication Conference and Exhibit 2001, OFC 2001, vol. 4, pp. PD10–1, 2001.

[2] Nashimoto, K., "PLZT thin film optical waveguide devices," *Proceedings of the 13th IEEE International Symposium on Applications of Ferroelectrics, ISAF 2002*, pp. 123–128, 2002.

[3] Kumar, A. K. S., Dahl, Ø., Pettersen, S. V., Grepstad, J. K., and Tybell, T., "Characterization of crystalline $Pb_{0.92}La_{0.08}Zr_{0.4}Ti_{0.6}O_3$ thin films grown by off-axis radio frequency magnetron sputtering," *Thin Solid Films*, vol. 492, pp. 71–74, 2005.

[4] Joannopoulos, J. D., Villeneuve, P. R., and Fan, S., "Photonic crystals: putting a new twist on light," *Nature*, vol. 386, pp. 143–149, 1997.

[5] Meade, R. D., Devenyi, A., Joannopoulos, J. D., Alerhand, O. L., Smith, D. A., and Kash, K., "Novel applications of photonic band gap materials: Low-loss bends and high Q cavities," *J. Appl. Phys.*, vol. 75, pp. 4753–4755, 1994.

[6] Mekis, A., Chen, J. C., Kurland, I., Fan, S., Villeneuve, P. R., and Joannopoulos, J. D., "High transmission through sharp bends in photonic crystal waveguides," *Phys. Rev. Lett.*, vol. 77, pp. 3787–3790, 1996.

[7] Kondo, M., Maruyama, K., and Kurihara, K., "Epitaxial ferroelectric thin films on silicon substrates for future electronic devices," *Fujitsu Sci. Tech. J.*, vol. 38, pp. 46–53, 2002.

[8] Johnson, S. G., and Joannopoulos, J. D., "Block-iterative frequency-domain methods for Maxwell's equations in a planewave basis," *Opt. Express*, vol. 8, pp. 173–190, 2001.

[9] Johnson, S. G., Fan, S., Villeneuve, P. R., Joannopoulos, J. D., and Kolodziejski, L. A., "Guided modes in photonic crystal slabs," *Phys. Rev. B*, vol. 60, pp. 5751–5758, 1999.

[10] Kostic, P., Okada, Y., Collins, N. C., Schlesinger, Z., Reiner, J. W., Klein, L., Kapitulnik, A., Geballe, T. H., and Beasley, M. R., "Non-fermi-liquid behavior of $SrRuO_3$: Evidence from infrared conductivity," *Phys. Rev. Lett.*, vol. 81, pp. 2498–2501, 1998.

[11] Méchin, L., Chabli, A., Bertin, F., Burdin, M., Rolland, G., Vannuffel, C., and Villégier, J. C., "A combined x-ray specular reflectivity and spectroscopic ellipsometry study of CeO_2/yttria-stabilized-zirconia bilayers on Si(001) substrates," *J. Appl. Phys.*, vol. 84, pp. 4935–4940, 1998.

[12] Johnson, S. G., Fan, S., Villeneuve, P. R., and Joannopoulos, J. D., "Linear waveguides in photonic-crystal slabs," *Phys. Rev. B*, vol. 62, pp. 8212–8222, 2000.

[13] Cheng, D. K., *Field and Wave Electromagnetics.* New York, USA: Addison-Wesley, 2nd ed., 1989. pp. 369–371.

[14] Dodge, J. S., Weber, C. P., Corson, J., Orenstein, J., Schlesinger, Z., Reiner, J. W., and Beasley, M. R., "Low-frequency crossover of the fractional power-law conductivity in $SrRuO_3$," *Phys. Rev. Lett.*, vol. 85, pp. 4932–4935, 2000.

[15] Lee, W. S., Ahn, K. C., Yoon, S. G., and Kim, C. S., "Effect of film thickness on the ferroelectric properties of $Pb(Zr_{0.2}Ti_{0.8})O_3$ thin films for nano-data storage applications," *J. Vac. Sci. Technol. B*, vol. 23, pp. 1901–1904, 2005.

Chapter 9

The case for electro-optic waveguide devices from ferroelectric (Pb,La)(Zr,Ti)O_3 thin film epilayers

Nordseth, Ø., Kjellman, J. Ø., You, C. C., Røyset, A., Tybell, T., and Grepstad, J. K., *Proc. of SPIE*, vol. 7381, pp. 73810F-1–73810F-13, 2009.

Abstract: (Pb,La)(Zr,Ti)O_3 (PLZT) thin films were grown epitaxially on MgO(001) substrate by radio frequency magnetron sputtering. Different ridge-type waveguides, including a Mach-Zehnder interferometer with co-planar metal electrodes, were defined in the PLZT epilayer using standard photolithographic techniques. The propagation losses for transverse electric polarized infrared light (λ_0 = 1550 nm) in these ridge-type channel waveguides were measured at ~10 dB/cm. Electro-optic modulation was demonstrated with a half-wave voltage $V_\pi \approx 150$ V for a 3 mm interaction length, corresponding to a Pockels coefficient $\mathfrak{r}_{51} \approx 8.3$ pm/V. Photonic crystal slabs (PCSs) were defined by etching a hexagonal two-dimensional lattice of holes in prepatterned ridge-type waveguides, using a focused ion beam. The sidewalls of the etched holes were inclined by an angle of ~10°. The impact on the transmission properties of these

PCSs caused by out-of-plane structural asymmetries, such as deviation from a cylindrical shape of the FIB-etched air holes and the presence of a substrate with refractive index different from that of air, was investigated by numerical simulation. Auger depth profiling was used to investigate Ga^+ ion implantation into the PLZT epilayer during FIB processing. The measurements suggest that such implantation of Ga^+ is confined to the uppermost $\sim$50 nm of the sample surface.

9.1 Introduction

The perovskite oxides offer a comprehensive selection of physical properties, such as dielectric, semiconducting, and metallic behavior, superconductivity, ferromagnetism, ferroelectricity, and electro-optic effects, which make them attractive for device applications. Moreover, these materials permit engineering of epitaxially integrated thin film devices. The ferroelectric perovskite $(Pb,La)(Zr,Ti)O_3$ (PLZT) has been recognized as a promising material for electro-optic devices, with high transparency at visible and infrared frequencies and large electro-optic coefficients [1, 2]. In bulk crystalline PLZT, Pockels and Kerr coefficients up to 10^{-10} m/V and 10^{-16} m^2/V^2 have been reported [3], exceeding those of commonly used electro-optic materials such as $LiNbO_3$ and $KTiOPO_4$ (KTP) [4]. By virtue of these characteristics, PLZT has the potential to reduce the physical size and driving voltage of electro-optic devices. For PLZT thin films, the electro-optic properties depend on several factors, including chemical composition and crystalline quality and orientation, with different reported values for the electro-optic coefficients [5–7]. Thus, the introduction of PLZT thin films in optical waveguide devices requires a thorough understanding of their electro-optic response. From a device perspective, it is important to measure the electro-optic characteristics of the thin film material, which calls for fabrication of a functional device [8–10].

Photonic crystals provide a new way to control and manipulate light with potential benefits to integrated opto-electronics [11, 12]. By domain engineering using a local probe [13, 14] or by taking advantage of the electro-optic effect to modulate the refractive index [15, 16], photonic crystals defined in thin films of PLZT may be put to use in high density, ultra-compact photonic circuits, as well as active optical devices with an intrinsic response in the gigahertz range [17, 18]. Quasi-two-dimensional photonic crystals, also referred to as photonic crystal slabs (PCSs), hold substantial promise for application in integrated optics, since they allow excellent control of in-plane light propagation and may be fabricated using established thin film processing methods [19–21]. In order to explore the potential of PLZT for planar photonic devices, reliable techniques for synthesis of high quality thin films as well as the fabrication of photonic nanostructures in such material are required.

In this study, we discuss the case for introduction of ferroelectric PLZT thin films, sputter-deposited on (001)-oriented MgO substrate, in electro-optic device applications. MgO(001) permits epitaxial growth of perovskite PLZT, and its low refractive index at infrared frequencies makes this substrate suitable for planar waveguiding [22, 23]. Magnetron sputter deposition allows for the growth of high-quality PLZT thin film epilayers with good control of the cation stoichiometry. The composition of the sputter target was chosen so as to obtain a linear electro-optic response (Pockels effect) and ferroelectric hysteresis behavior with large coercive fields, characteristics favorable to electro-optic devices operating without a biasing field [24]. A ridge-type Mach-Zehnder (MZ) interferometer was designed and processed to allow for experimental investigation of the electro-optic properties of the PLZT thin films. Furthermore, we have explored the possibilities offered by focused ion beam (FIB) etching to define PCSs in these PLZT epilayers. The impact on the transmission properties of the PCS from out-of-plane structural asymmetries, such as those arising from the presence of the MgO substrate and deviations from the ideal cylindrical geometry of the ion-milled air holes, has been explored by numerical simulation. Moreover, we discuss possible effects of gallium ion implantation in the PLZT epilayer upon FIB processing.

9.2 Waveguide, photonic crystal slab modelling

Ridge-type channel waveguides and a MZ interferometer were designed[1] using a commercially available computer software package (FIMMWAVE ver. 4.61, Photon Design Ltd.). The waveguide profile and the MZ interferometer geometry are depicted in Figure 9.1(a) and (b), respectively. The numerical analysis pertains to propagation of the fundamental transverse electric (TE) mode ($\lambda_0 = 1550$ nm) in a lossless dielectric material. The refractive index of the PLZT film was set at $n = 2.45$, as obtained from spectroscopic ellipsometry measurements [25], whereas the refractive index of the substrate was set at $n = 1.72$, corresponding to that reported for MgO at infrared wavelengths [26]. For a ridge-type waveguide of width $W \approx 2$–3 µm and height $d \approx 75$–100 nm, defined in a PLZT epilayer of thickness $h = 500$ nm, the two lowest order TE modes are supported. The Y-junctions of the MZ interferometer were designed with a bend extension $s_x = 1$ mm and a separation $s_y = 100$ µm between the branches. The absorption coefficient of the electrode material was set at $\alpha = 7.98 \times 10^5$ cm^{-1}, corresponding to that of gold at infrared wavelengths. The thickness and length (L) of the electrodes were 250 nm and 3 mm, respectively, which implies an electro-optic interaction length of 3 mm for the device. The gap between the center electrode and the outer electrodes was $g_e = 8$

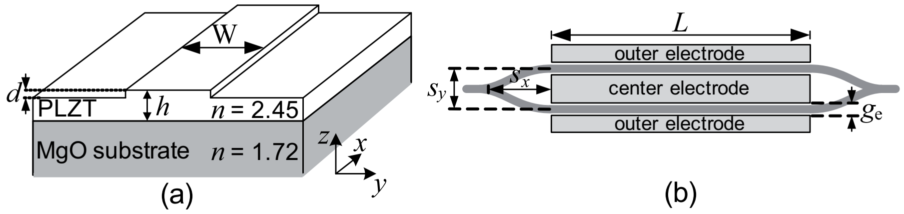

Figure 9.1: Schematic of (a) a ridge-type channel waveguide and (b) the Mach-Zehnder interferometer defined in PLZT thin films on MgO.

---

[1] The numerical analysis is presented in Appendix C

µm. With these design parameters, the overall losses for propagation of the fundamental TE mode through the MZ interferometer were estimated at ∼5–6 dB.

The design of a hole-type PCS in an air-suspended PLZT membrane was previously established by numerical simulation [27] using the MIT Photonic-Bands (MPB) software package [28]. The essential design parameters for this PCS include the refractive index of the slab material (n), the slab thickness (h), the air hole radius (r), and the configuration and lattice constant (a) of the 2D air hole lattice. The photonic band diagram in Figure 9.2(a) displays the guided even and odd modes of the air-suspended PLZT PCS for a hexagonal lattice of air holes. For a dielectric slab with refractive index $n = 2.45$, a hexagonal lattice typically leads to a larger photonic band gap than that of a square lattice. The largest band gap (shaded in grey) is found between the first and second even mode bands and extends from 0.358 to 0.485 in normalized frequency units (a/λ_0). Maximum band gap, $\Delta f/f_c = 27$ % (where Δf is the size of the gap and f_c is its center frequency), is obtained for a slab thickness $h = 0.8a$ and a hole radius $r = 0.38a$ [27]. Figure 9.2(b) shows the even

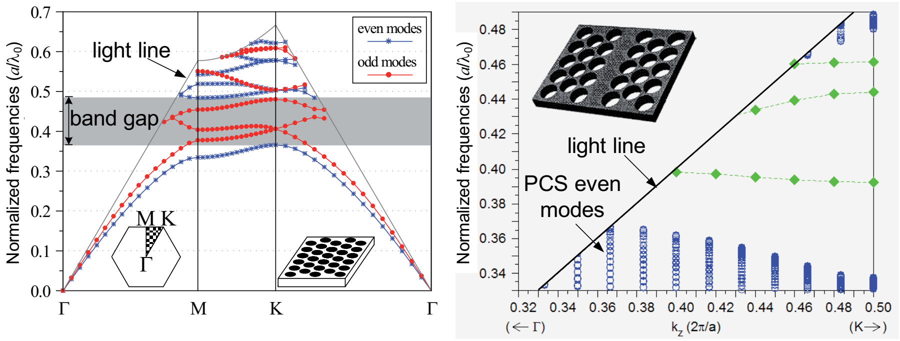

(a) (b)

Figure 9.2: (a) Photonic band diagram of an air-suspended PLZT PCS for a slab thickness h = 0.8a, a hole radius r = 0.38a, and a hexagonal configuration of holes. (b) Even mode frequency dispersions (green diamonds) of a line-defect waveguide in the 2D crystal lattice, as depicted in the inset.

mode frequency dispersions of a line-defect waveguide, defined in the PLZT PCS by removing a row of adjacent (nearest neighbor) holes from the 2D crystal lattice (cf. the inset). Only waveguide modes that fall inside the even mode band gap of the PCS are shown. The frequency dispersions of the PLZT PCS are projected onto the Γ–K axis of the hexagonal 2D reciprocal lattice [29], cf. the left inset in Figure 9.2(a). The calculated frequency dispersions show that this single-row line-defect waveguide supports three even modes in the photonic band gap.

Transmission data for the PLZT PCS was obtained from 3D finite-difference time-domain (FDTD) simulations (CrystalWave ver. 4.0, Photon Design Ltd.) with uniaxial perfectly matched layers used as boundary conditions for termination of the computational domain [30].[2] A sinusoidally modulated Gaussian pulse was adopted to represent excitation of TE polarized light. Wave propagation in a linear, time-invariant, lossless dielectric medium was assumed, with a computational resolution of 32 points per lattice constant. Figure 9.3(a) shows the calculated TE transmission spectrum for an air-suspended PLZT PCS, with $h = 0.8a$ and cylindrical air holes of radius $r = 0.38a$. This spectrum shows that the transmission stop band coincides with the calculated band gap for even modes, shown in Figure 9.2(a), with a maximum attenuation of ∼37 dB in the frequency range $0.41–0.47a/\lambda_0$.

PCSs defined in a PLZT epilayer on MgO substrate are asymmetric with respect to the plane bisecting the PLZT film. FIB-processed PCSs exhibits an additional asymmetry with respect to this plane, as will be discussed in section 9.4.2, due to the non-cylindrical shape of the etched air holes. Figure 9.3(b) shows the calculated transmission spectrum for a PLZT PCS on MgO substrate for $h = 0.8a$, $r = 0.38a$, and an air hole taper angle $\theta = 10^\circ$ (cf. inset in Figure 9.3(b)). The calculations show that maximum attenuation for TE polarized light (∼29 dB) is significantly reduced compared to that of an air-suspended PLZT PCS with cylindrical air holes. Hence, this numerical analysis demonstrates that the optical isolation properties of the PLZT PCS are impaired by the vertical

---

[2] A detailed description of the computational techniques is provided in Appendix D

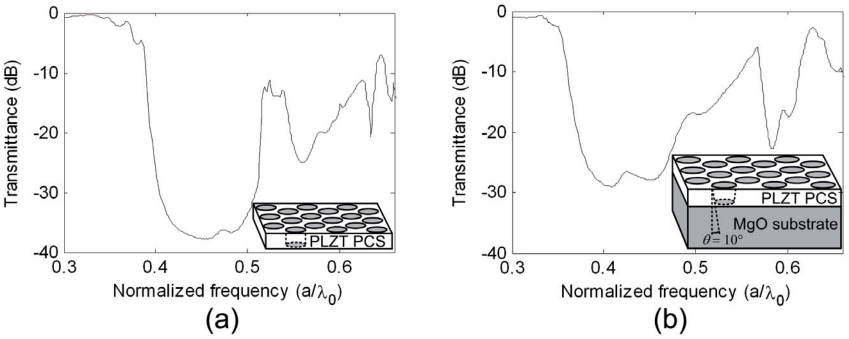

(a) (b)

Figure 9.3: Calculated TE transmission spectrum for (a) an air-suspended PLZT PCS with cylindrical air holes and (b) a PLZT PCS with tapered air holes (θ = 10°) on MgO substrate.

structural asymmetry introduced by the non-cylindrical air holes and the underlying MgO substrate. These findings are in good agreement with previous studies of structural asymmetries in PCSs [31–33], and can be ascribed to TE-TM mode coupling [34].

9.3 Experimental

9.3.1 Thin film growth and device processing

$Pb_{0.92}La_{0.08}Zr_{0.4}Ti_{0.6}O_3$ thin film epilayers with thickness $h \approx 500$ nm were grown on (001)-oriented MgO substrate by on-axis radio frequency magnetron sputtering. The details of the growth are described in section 6.2.1. Figure 9.4(a) displays a typical θ-2θ x-ray diffractogram of PLZT on MgO(001). The scan shows monocrystalline (001)-oriented PLZT of good crystalline quality, as judged by the rocking curve full width at half maximum (FWHM) of the (001) Bragg reflection. Figure 9.4(b) shows typical φ-scans of the PLZT(101) and MgO(202) reflections. The fourfold symmetry and in-plane alignment of the diffraction peaks confirm epitaxial growth of PLZT, with the [100] crystalline axis of PLZT parallel to that of the substrate. Atomic force microscopy (AFM) measurements showed a root-mean-square (RMS) surface roughness of ~2 nm for the PLZT thin film, which should be adequate for optical waveguides in terms of low scattering losses [35]. Ferroelectric hysteresis loop measurements showed a remanent polarization $P_\mathrm{r} \approx 36$ µC/cm^2 and a coercive field $E_\mathrm{c} \approx 140$ kV/cm. The refractive index for $\lambda_0 = 1550$ nm was estimated at $n \approx 2.45$ from spectroscopic ellipsometry measurements [25].

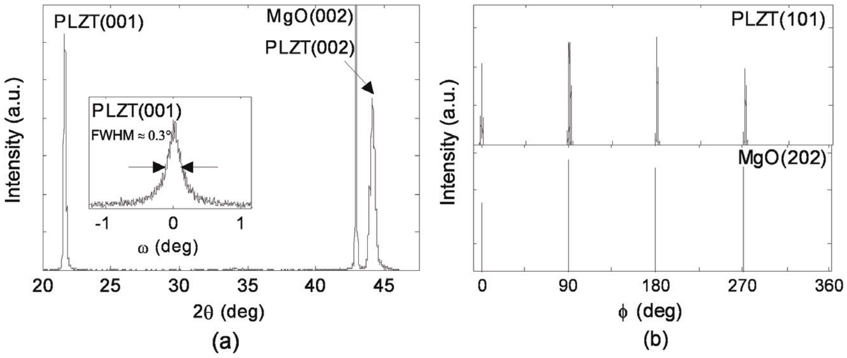

Figure 9.4: (a) Typical θ-2θ x-ray diffractogram of PLZT on MgO(001). The inset shows the rocking curve recorded on the PLZT(001) reflection. (b) φ-scans of the PLZT(101) and MgO(202) reflections.

Ridge-type channel waveguides were defined in the PLZT epilayer using conventional photolithography and chemical wet etching. The etchant was prepared according to the recipe proposed by Zheng *et al.* [36], which implies mixing buffered hydrofluoric acid, hydrochloric acid, ammonium chloride and deionized (DI) water, with a volume ratio HF:HCl:NH_4Cl:H_2O = 1:2:4:100. The samples were subsequently immersed in NHO_3:H_2O = 2:1 for 30 s in order to remove chemical residues. Co-planar electrodes were defined by electron beam evaporation of a metal bilayer of 10 nm Pt and 200 nm Au, followed by a lithographic lift-off process. AFM measurements were used to determine the etch rate for PLZT (~6 nm/s) and to examine the topography of the fabricated ridges. The waveguides were oriented parallel to the [100]-direction of the MgO substrate, and their facets were mechanically polished to an RMS surface roughness of ~4 nm.

9.3.2 Focused ion beam processing of photonic crystal slabs

FIB etching was used to process hole-type PCSs and line-defect PCS waveguide structures in ridge-type waveguides preprocessed in the PLZT/MgO thin film sample. The structural parameters of the PCSs were chosen so as to place the fundamental band gap for TE-like modes around the telecommunication wavelength $\lambda_0 = 1550$ nm. From numerical analysis we obtain an optimum PCS lattice constant $a = 660$ nm, a slab thickness $h = 528$ nm, and a hole radius $r = 250$ nm for the hexagonal hole-type PLZT PCS. The corresponding (calculated) band gap for TE-like modes spans a range of wavelengths from 1400 to 1700 nm. Figure 9.5 shows a scanning electron microscope (SEM) image of a hexagonal 2D lattice of air holes defined in the PLZT epilayer. The lattice constant a, the hole radius r, and the crystal symmetry directions Γ–M and Γ–K are indicated on the image. The FIB processing was carried out using a FEI Strata 235DB dual-beam FIB/SEM system. Ga^+ ions from a liquid metal ion source were accelerated to 30 kV in high vacuum ($\sim 1 \times 10^{-5}$ mbar), providing a spot size of approximately 10 nm for the focused beam. The best results were obtained with sequential milling of the air holes, using a probe current of ∼115 pA. Each hole was etched for

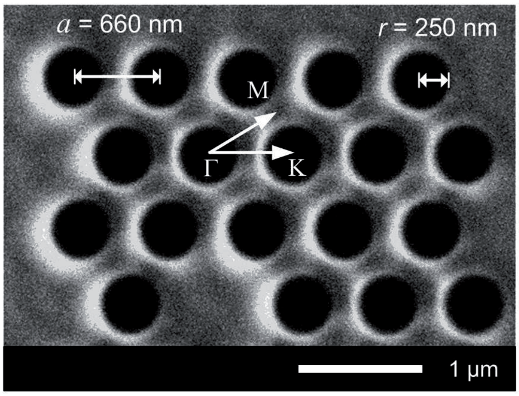

Figure 9.5: Top-view SEM image of the hexagonal array of cylindrical air holes in the PLZT epilayer, processed by FIB etching.

5 s and the etching rate was estimated at $\sim$0.16 µm^3/s. Initial charging problems were overcome by coating parts of the PLZT/MgO sample surface with colloidal graphite paste. After FIB processing, this paste was readily removed by an ultrasonic rinse in isopropyl alcohol.

In order to look for possible implantation of Ga$^+$ ions in the PLZT epilayer, Auger depth profile measurements were carried out using a JEOL JAMP-9500F FE Auger microprobe. Prior to this analysis, the sample surface was coated with a thin ($\sim$5 nm) Pt layer to prevent electrostatic charging.

9.3.3 Optical measurement set-up

The experimental set-up for end-fire coupling of infrared (IR) light ($\lambda_0 = 1550$ nm) from a CW distributed feedback laser (Anritsu GB-5A-016) into the ridge-type waveguides is depicted in Figure 9.6(a). This set-up allows for precise alignment of the sample stage and the polarization-conserving single-mode tapered lensed fibers (Nanonics Imaging), as shown in the microscope image in Figure 9.6(b). The input fiber is mounted on a rotation stage, and the polarization of the light input is controlled with an in-fiber polarizer (Chiral Photonics IFP-155D-SM). Light propagation along the waveguide is

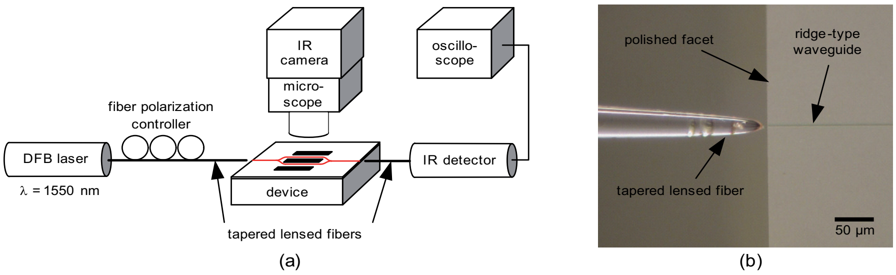

Figure 9.6: (a) Optical measurements set-up for end-fire coupling of IR light into the thin film waveguide device. (b) Microscope image showing alignment of the tapered lensed fiber with the input waveguide close to the polished facet of the device.

monitored with a microscope objective coupled to an IR video camera (Xenics XEVA-FPA-1.7-640) mounted above the device. The transmitted intensity at the waveguide output is measured with an IR photodetector connected to a digital oscilloscope (Tektronix TDS2004B). Contact needles attached to probe-head manipulators (Süss MicroTec PH100) were used to apply a modulation voltage to the electrodes of the MZ interferometer.

9.4 Results and discussion

9.4.1 Device characterization and optical measurements

Low propagation losses are essential to the use of thin film waveguides in integrated optics. The main sources of such losses are material absorption and optical scattering from defects and surfaces. Figure 9.7 shows (a) an AFM image (5 × 5 µm^2) and (b) a cross-section line-scan of a ridge-type channel waveguide defined in the PLZT epilayer by UV lithography and wet etching. The ridge-top RMS surface roughness was measured at ∼4 nm, as compared to ∼2 nm for the surface of the as-grown film, whereas the RMS surface roughness of the ridge sidewalls was measured at ∼20–30 nm.

The theoretical work of Payne and Lacey relates scattering losses to the sidewall roughness of optical waveguides [37]. For the 3 µm wide PLZT ridge-type waveguide, with a sidewall roughness of ∼20–30 nm, the scattering losses were estimated at ∼5 dB/cm for the fundamental TE mode. The impact of sidewall roughness on scattering losses decreases with increasing ridge width. Propagation losses caused by sidewall roughness can thus be reduced by increasing the ridge width. However, this also increases the probability that the waveguide turns multimode. Moreover, various etching techniques, such as inductively coupled plasma (ICP) etching, reactive ion etching (RIE) followed by thermal oxidation, and chemically assisted ion beam etching (CAIBE), were adopted in order to produce thin film optical waveguides with modest sidewall roughness [38–40].

Propagation losses for excitation of the fundamental TE mode

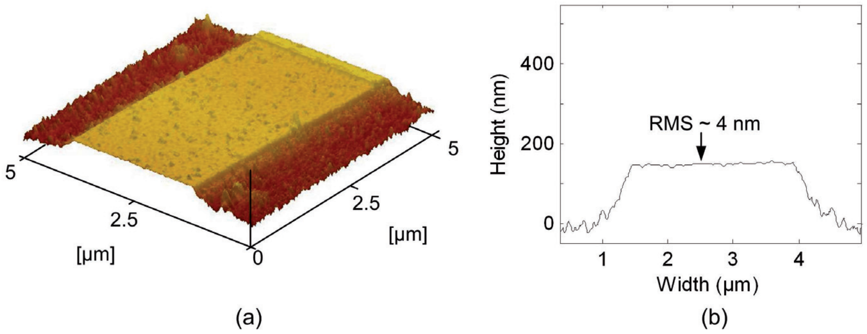

Figure 9.7: (a) AFM image (5 × 5 µm^2) and (b) line-scan across a ridge-type channel waveguide processed in the PLZT epilayer by UV lithography and chemical wet etching.

(λ_0 = 1550 nm) in a ridge-type waveguide (W = 3 µm) were evaluated by measuring the out-of-plane scattered intensity. The recorded intensity vs. propagation distance in the waveguide is shown in Figure 9.8(a). The slope of the measured decrease in scattered light intensity renders a power loss of 13.4 dB/cm. Figure 9.8(b) shows the dependence of the measured propagation losses on the ridge width for λ_0 = 1300 nm and λ_0 = 1500 nm IR light. This data reveals that the losses decrease with increasing ridge width, suggesting that scattering from the waveguide sidewalls affects the overall propagation losses. By subtraction of calculated scattering losses caused by sidewall roughness from the measured losses, the propagation losses for the 3 µm wide PLZT ridge-type waveguide are estimated at ∼10 dB/cm. These losses are comparable to those previously reported for pulsed laser deposited PLZT thin films [41]. Moreover, we find that the measured propagation losses are noticeably higher for λ_0 = 1300 nm, compared to λ_0 = 1550 nm. This difference was previously observed for a PLZT reversed ridge waveguide, and attributed to reduced Rayleigh scattering for longer wavelengths [42].

Preliminary data from electro-optic modulation experiments on the ridge-type MZ interferometer (cf. Figure 9.1(b)) is shown in Figure 9.9. The applied modulation voltage and the resulting modulation of the optical intensity (I) at the output of the MZ inter-

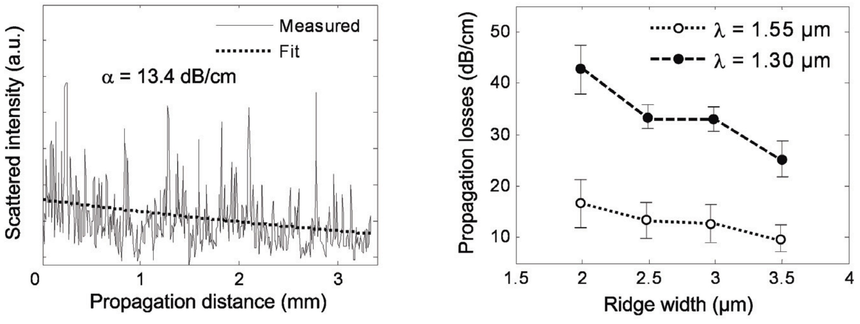

(a) (b)

Figure 9.8: (a) Out-of-plane scattered intensity as a function of propagation distance along the ridge-type waveguide in Figure 9.6(b). (b) Propagation losses vs. ridge width for $\lambda = 1300$ nm and $\lambda = 1550$ nm.

ferometer for TE polarized light are shown in Figure 9.9(a). The data shows a distinct electro-optic response, with ~80 % intensity modulation (I/I_{max}). The corresponding plot of intensity modulation vs. applied field for 10 different periods is shown in Figure 9.9(b). The observed offset of this curve (~20 V with respect to zero applied voltage) is tentatively ascribed to asymmetries in the modulator design and fabrication, cf. Figure 3.13. A phase retardation difference π between the two arms of the MZ interferometer was obtained for a first half period voltage $V_{\mathrm{fhp}} = 150$ V, which translates to a Pockels coefficient[3] $\mathfrak{r}_{51} = 8.3 \times 10^{-12}$ m/V for a birefringence $|n_{\mathrm{o}} - n_{\mathrm{e}}| = 0.005$. For anisotropic crystals with 4mm symmetry, such as $\mathrm{Pb_{0.92}La_{0.08}Zr_{0.4}Ti_{0.6}O_3}$, the Pockels coefficient $\mathfrak{r}_{51}$ (equal to $\mathfrak{r}_{42}$) is normally large. However, the *c*-axis orientation of the PLZT epilayer combined with the co-planar electrode geometry implies that electro-optic modulation will not be very effective unless the ferroelectric thin film is uniformly poled perpendicular to the film plane, i.e., along the optical axis. In this experiment, the MZ interferometer was processed in as-grown PLZT films, without additional poling. Moreover, the modulation field was applied across one of the

---

[3] Using the expression $\mathfrak{r}_{15} = \frac{g_{\mathrm{e}}}{n^3 V_{\mathrm{fhp}}} \sqrt{\left(\frac{\lambda_0}{L} \cdot 2|n_{\mathrm{o}} - n_{\mathrm{e}}|\right)}$, cf. Ref. 43.

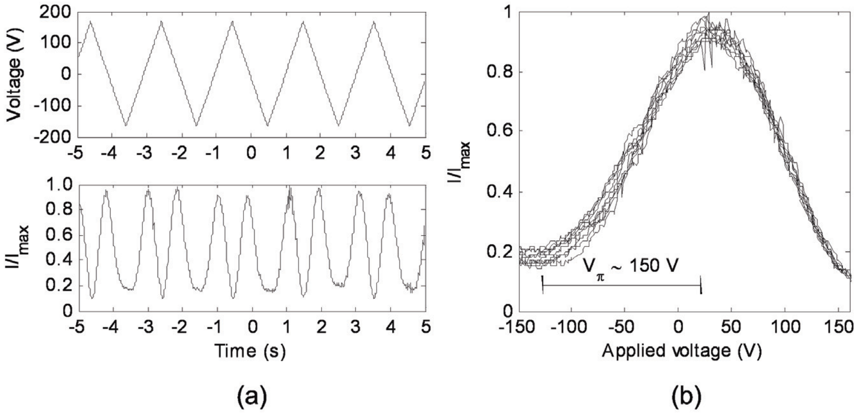

Figure 9.9: (a) Time dependence of applied voltage and intensity modulation for the ridge-type MZ interferometer. (b) Corresponding plot of intensity modulation vs. applied voltage for 10 periods, with a half-wave voltage V_π = 150 V.

two interferometer branches only. Further electro-optic modulation experiments will investigate the effect of post-deposition poling of the films, as well as applying an electric field across both branches of the MZ interferometer.

9.4.2 Focused ion beam processed photonic crystal slabs

Figure 9.10(a) shows an ion beam scanning image of a waveguide structure defined in the PLZT epilayer by FIB etching. The micrograph demonstrates that the PCS patterns are accurately reproduced and may be precisely aligned with preprocessed features, implying that maskless FIB etching is well suited for processing of PCS lattices and nanostructured waveguides in perovskite thin films. Drift of the ion beam was not significant over the time period required to process large patterns and devices.

Figure 9.10(b) displays a cross-section SEM image of air holes perforating the PLZT epilayer and the MgO substrate. The image shows that the sidewalls are inclined by an angle θ of approximately

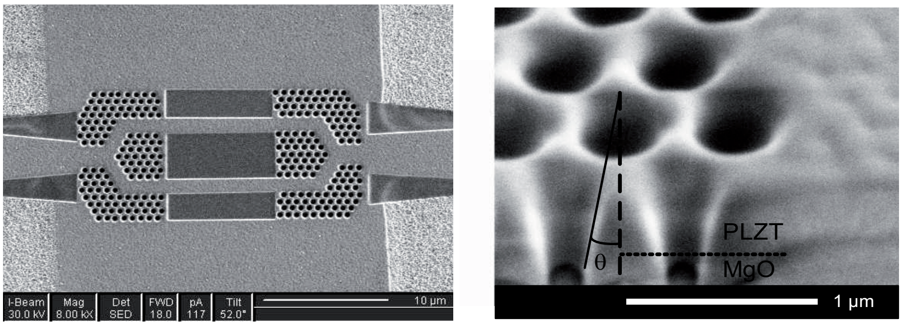

(a) (b)

Figure 9.10: (a) Scanning ion beam image of photonic crystal waveguide structure processed in the PLZT epilayer by FIB etching. (b) Cross-section SEM image of the 2D photonic crystal lattice of air holes. The hole sidewall angle θ is approximately 8–12° off the film surface normal.

8–12°, measured with respect to the film surface normal and decreasing slightly with depth into the PLZT layer. This deviation from ideal vertical sidewalls is caused by sputter redeposition during FIB etching, and has been reported in previous studies using FIB processing for definition of PCSs [43, 44]. Moreover, the hole profile in Figure 9.10(b) shows that the etched air holes fully perforate the ~500 nm thick PLZT layer. Extending the air holes of the 2D crystal lattice into the substrate will lower the effective refractive index in the region of the substrate where guided modes have a non-negligible field amplitude [45]. Numerical analysis of the PLZT PCS on MgO shows that the effective TE stop band broadens and offers increased attenuation when the air holes are extended into the substrate by a depth equal to the lattice constant. In this case, modes that are localized in the slab will couple less strongly to the background and the expansion of the TE stop band suggests that the TE-TM mode coupling is suppressed. Moreover, construction of air-bridged slabs, providing out-of-plane structural symmetry and strong vertical confinement of the light, can be achieved by removing the underlying substrate, e.g., fabrication of air-suspended PLZT PCSs may be realized by deposition of thin films on silicon substrate (cf. Chapter

7), for which etching techniques capable of controlled removal of the substrate support are known.

The propagation of TE polarized light ($\lambda_0 = 1500$ nm) through a PCS waveguide structure defined in the PLZT epilayer was investigated experimentally by observation of the out-of-plane scattered intensity. Figure 9.11 shows an IR image (dashed frame) superimposed on an optical microscope image of a double 60° waveguide bend formed by omitting three rows of holes from the 2D crystal lattice. The distribution of scattered light in the recorded IR image suggests that the incoming waves are guided through the first 60° waveguide bend (upper left) and subsequently arrive at the second bend, recognized by the increased amount of scattered intensity at the corner of this bend. The inset in Figure 9.11 shows the recorded out-of-plane scattered intensity as a function of position along the indicated line segment bisecting the waveguide structure. The plot shows that the scattered intensity is significantly lower at the second bend compared to that at the first. This suggests that transmission of light through these PCS waveguide bends is not very efficient. Moreover, the measurements reveal an increased level of scattered intensity at the transition regions between the PCS structures and the ridge-type waveguides, which indicates substantial reflection losses in these regions.

FIB processing entails collateral ion implantation of the sample, which may affect the physical properties of the material [46], e.g., formation of an amorphous surface region in ferroelectric single crystals [47], modified conductivity of ZnO nanorods [48], or increased optical absorption for implantation of Ga^+ ions in hydrogenated amorphous SiC thin films [49]. Hence, implantation of Ga^+ ions may impair the ferroelectric and optical properties of the PLZT epilayer. The SEM image in the inset of Figure 9.12 shows a region of the PLZT film surface, with indication of three different spots for which the film surface composition was locally analyzed using the Auger microprobe. Pos. 1 corresponds to an area scanned with the FIB during optimization of the PCS fabrication process, i.e., the surface was continuously scanned to produce an ion beam image used for adjusting focus and stigmatism. Pos. 2 is located inside a processed PCS structure, whereas pos. 3 corresponds to a surface region that was

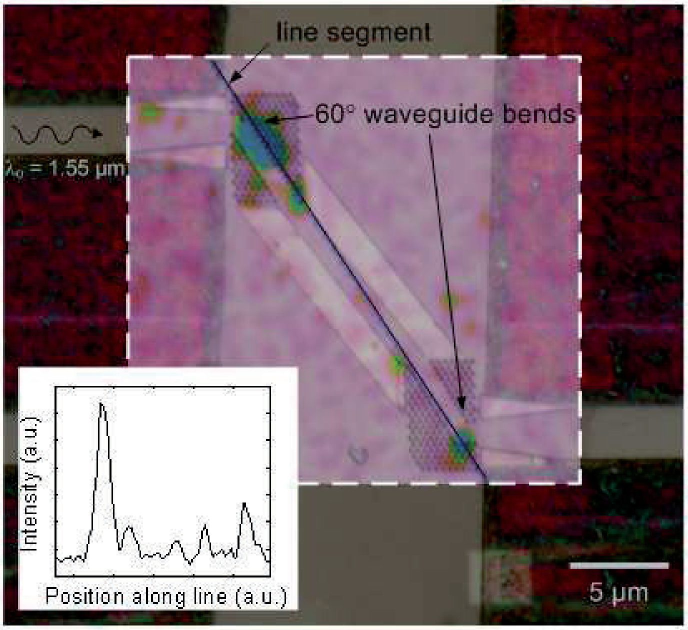

Figure 9.11: IR image superimposed on an optical microscope image of a double 60° photonic crystal waveguide bend (green and blue indicate levels of high intensity). The inset shows the out-of-plane scattered intensity of IR light vs. position along the line segment bisecting the waveguide structure.

never exposed to the Ga^+ ion beam. The relative concentration of gallium vs. depth into the PLZT epilayer for positions 1–3 is shown in Figure 9.12. For pos. 2, the Auger data shows a maximum Ga concentration at a projection range of ~20 nm, while the tail of the implantation profile extends ~55 nm into the PLZT layer. Beyond a depth of 60 nm, the concentration of implanted gallium is negligible for both positions 1 and 2, suggesting that the implantation of Ga^+ ions into the PLZT epilayer is confined to the uppermost ~50 nm of this layer. The measured Ga concentration in pos. 3 is negligible, which implies that the ion implantation is restricted to the surface regions that have been directly exposed to the FIB.

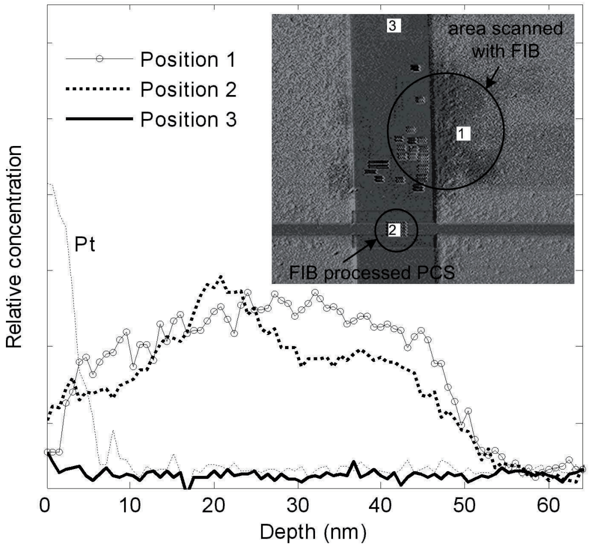

Figure 9.12: Auger depth profiles of Ga in the PLZT epilayer. The inset shows the different positions (1–3) locally analyzed by the Auger microprobe.

9.5 Conclusions

A ridge-type MZ interferometer with an electro-optic interaction length of 3 mm was processed in a PLZT epilayer on MgO(001) substrate, using UV lithography and chemical wet etching. Electro-optic response was verified, with a ~80 % modulation of the optical intensity for a half-wave voltage $V_\pi \approx 150$ V. The corresponding Pockels coefficient was estimated at $\mathfrak{r}_{51} \approx 8.3$ pm/V. The propagation losses for ridge-type waveguides were measured at ~10 dB/cm for $\lambda_0 = 1550$ nm. FIB etching was used to define PCSs with a hexagonal hole configuration in the PLZT thin film epilayer. The sidewalls of the FIB etched holes were inclined by an angle of ~8–12° with respect to the film surface normal. Numerical simulations showed that the transmission properties of the PCS are impaired by out-of-plane structural asymmetries, such as those caused by the presence of a dielectric substrate and tapered geometry of the FIB etched air holes. Propagation of IR light through a 60° PCS waveguide bend was demonstrated. Auger depth profile measurements showed that the Ga^+ ion implantation was confined to the uppermost ~50 nm of the PLZT epilayer surface.

References

[1] Haertling, G. H., "PLZT electrooptic materials and applications – a review," *Ferroelectrics*, vol. 75, pp. 25–55, 1987.

[2] Hardtl, K. H., and Hennings, D., "Distribution of A-site and B-site vacancies in (Pb,La)(Ti,Zr)O_3 ceramics," *J. Am. Ceram. Soc.*, vol. 55, pp. 230–231, 1972.

[3] Haertling, G. H., and Land, C. E., "Hot pressed (Pb,La)(Zr,Ti)O_3 ferroelectric ceramics for electrooptic applications," *J. Am. Ceram. Soc.*, vol. 54, pp. 1–11, 1971.

[4] Garcia-Cabanes, A., Cabrera, J. M., and Agullo-Lopez, F., *Encyclopedia of Optical Engineering.* New York: Marcel Dekker Inc., 2003.

[5] Sato, K., Ishii, M., Kurihara, K., and Kondo, M., "Crystal orientation dependence of the electro-optic effect in epitaxial lanthanum-modified lead zirconate titanate films," *Appl. Phys. Lett.*, vol. 87, p. 251927, 2005.

[6] Nakada, M., Ohashi, K., and Akedo, J., "Optical and electro-optical properties of Pb(Zr,Ti)O_3 and (Pb,La)(Zr,Ti)O_3 films prepared by aerosol deposition method," *J. Cryst. Growth*, vol. 275, pp. 1275–1280, 2005.

[7] Uchiyama, K., Kasamatsu, A., Otani, Y., and Shiosaki, T., "Electro-optic properties of lanthanum-modified lead zirconate titanate thin films epitaxially grown by the advanced sol-gel method," *Jpn. J. Appl. Phys.*, vol. 46, pp. L244–L246, 2007.

[8] Kawaguchi, T., Adachi, H., Setsune, K., Yamazaki, O., and Wasa, K., "PLZT thin-film waveguides," *Appl. Opt.*, vol. 23, pp. 2187–2191, 1984.

[9] Thapliya, R., Okano, Y., and Nakamura, S., "Electrooptic characteristics of thin-film PLZT waveguide using ridge-type Mach-Zehnder modulator," *J. Lightwave Technol.*, vol. 21, pp. 1820–1827, 2003.

[10] Gill, D. M., Conrad, C. W., Ford, G., Wessels, B. W., and Ho, S. T., "Thin film channel waveguide electro-optic modulator in epitaxial $BaTiO_3$," *Appl. Phys. Lett.*, vol. 71, pp. 1783–1785, 1997.

[11] Yablonovitch, E., "Inhibited spontaneous emission in solid-state physics and electronics," *Phys. Rev. Lett.*, vol. 58, pp. 2059–2062, 1987.

[12] John, S., "Strong localization of photons in certain disordered dielectric superlattices," *Phys. Rev. Lett.*, vol. 58, pp. 2486–2489, 1987.

[13] Yin, Q. R., Li, G. R., Zeng, H. R., Liu, X. X., Heiderhoff, R., and Balk, L. J., "Ferroelectric domain structures in $(Pb,La)(Zr,Ti)O_3$ ceramics observed by scanning force microscopy," *Appl. Phys. A*, vol. 78, pp. 699–702, 2004.

[14] Ivey, M., and Bolie, V. W., "Birefringent light scattering in PLZT ceramics," *IEEE Trans. Ultrason. Ferroelectr. Freq. Control*, vol. 38, pp. 579–584, 1991.

[15] Takeda, H., and Yoshino, K., "Tunable photonic bandgap in two-dimensional photonic crystals by temporal modulation based on the Pockels effect," *Phys. Rev. E*, vol. 69, p. 016605, 2004.

[16] Xiong, S., and Fukshima, H., "Analysis of light propagation in index-tunable photonic crystals," *J. Appl. Phys.*, vol. 94, pp. 1286–1288, 2003.

[17] Scrymgeour, D., Malkova, N., Kim, S., and Gopalan, V., "Electro-optic control of the superprism effect in photonic crystals," *Appl. Phys. Lett.*, vol. 82, pp. 3176–3178, 2003.

[18] Li, B., Zhou, J., Li, L., Wang, X. J., Liu, X. H., and Zi, J., "Ferroelectric inverse opals with electrically tunable photonic band gap," *Appl. Phys. Lett.*, vol. 83, pp. 4704–4706, 2003.

[19] Chow, E., Lin, S. Y., Wendt, J. R., Johnson, S. G., and Joannopoulos, J. D., "Quantitative analysis of bending efficiency in photonic-crystal waveguide bends at $\lambda = 1.55$ µm wavelengths," *Opt. Lett.*, vol. 26, pp. 286–288, 2001.

[20] Notomi, M., Shinya, A., Yamada, K., Takahashi, J., Takahashi, C., and Yokohama, I., "Structural tuning of guiding modes of line-defect waveguides of silicon-on-insulator photonic crystal slabs," *IEEE J. Quantum Electron.*, vol. 38, pp. 736–742, 2002.

[21] Andreani, L. C., and Agio, M., "Photonic bands and gap maps in a photonic crystal slab," *IEEE J. Quantum Electron.*, vol. 38, pp. 891–898, 2002.

[22] Okuyama, M., Usuki, T., Hamakawa, Y., and Nakagawa, T., "Epitaxial growth of ferroelectric PLZT thin films and their optical properties," *Appl. Phys.*, vol. 21, pp. 339–343, 1980.

[23] McKee, R. A., Walker, F. J., Specht, E. D., Jellison, G. E., Boatner, L. A., and Harding, J. H., "Interface stability and the growth of optical quality perovskites on MgO," *Phys. Rev. Lett.*, vol. 72, pp. 2741–2744, 1994.

[24] Nordseth, Ø., Tybell, T., and Grepstad, J. K., "Epitaxial (Pb,La)(Zr,Ti)O_3 thin films on buffered Si(100) by on-axis radio frequency magnetron sputtering," *Thin Solid Films*, vol. 517, pp. 2623–2626, 2009.

[25] Nordseth, Ø., Røyset, A., Tybell, T., and Grepstad, J. K., "Sputter-deposited (Pb,La)(Zr,Ti)O_3 thin films: Effect

of substrate and optical properties," *J. Vac. Sci. Technol. A*, vol. 27, pp. 548–553, 2009.

[26] Synowicki, R. A., and Tiwald, T. E., "Optical properties of bulk c-ZrO_2, c-MgO and a-As_2S_3 determined by variable angle spectroscopic ellipsometry," *Thin Solid Films*, vol. 455, pp. 248–255, 2004.

[27] Nordseth, Ø., Tybell, T., and Grepstad, J. K., "Simulation of photonic band gap waveguides in lead-lanthanum zirconate-titanate, in: 2006 Northern Optics Conference Proceedings," pp. 51–54, 2006.

[28] Johnson, S. G., and Joannopoulos, J. D., "Block-iterative frequency-domain methods for Maxwell's equations in a planewave basis," *Opt. Express*, vol. 8, pp. 173–190, 2001.

[29] Johnson, S. G., Fan, S., Villeneuve, P. R., and Joannopoulos, J. D., "Linear waveguides in photonic-crystal slabs," *Phys. Rev. B*, vol. 62, pp. 8212–8222, 2000.

[30] Berenger, J. P., "A perfectly matched layer for the absorption of electromagnetic waves," *J. Comput. Phys.*, vol. 114, pp. 185–200, 1994.

[31] Qiu, M., "Band gap effects in asymmetric photonic crystal slabs," *Phys. Rev. B*, vol. 66, p. 033103, 2002.

[32] Takana, Y., Asano, T., Akahane, Y., Song, B. S., and Noda, S., "Theoretical investigation of two-dimensional photonic crystal slab with truncated cone air holes," *Appl. Phys. Lett.*, vol. 82, pp. 1661–1663, 2003.

[33] Vlasov, Y. A., Moll, N., and McNab, S. J., "Mode mixing in asymmetric double-trench photonic crystal waveguides," *J. Appl. Phys.*, vol. 95, pp. 4538–4544, 2004.

[34] Takana, Y., Sugimoto, Y., Ikeda, N., Nakamura, H., Watanabe, Y., Asakawa, K., and Inoue, K., "Guided modes of a width-reduced photonic-crystal slab line-defect

waveguide with asymmetric cladding," *J. Lightwave Technol.*, vol. 23, pp. 2749–2755, 2005.

[35] Wessels, B. W., Nystrom, M. J., Chen, J., Studebaker, D., and Marks, T. J., "Epitaxial niobate thin films and their nonlinear optical properties," *Mater. Res. Soc. Symp. Proc.*, vol. 401, pp. 211–218, 1996.

[36] Zheng, K., Lu, J., and Chu, J., "A novel wet etching process of Pb(Zr,Ti)O_3 thin films for applications in microelectromechanical system," *Jpn. J. Appl. Phys.*, vol. 43, pp. 3934–3937, 2004.

[37] Payne, F. P., and Lacey, J. P. R., "A theoretical analysis of scattering loss from planar optical waveguides," *Opt. Quant. Electr.*, vol. 26, pp. 977–986, 1994.

[38] Yap, K. P., Delage, A., Lamontagne, B., Janz, S., Xu, D. X., Lapointe, J., Waldron, P., Schmid, J., Chow-Chong, P., Post, E., and Syrett, B., "Scattering loss measurement of SOI waveguides using 5×17 integrated optical star coupler," *Proc. of SPIE*, vol. 6477, p. 64770J, 2007.

[39] Lee, K. K., Lim, D. R., Kimerling, L. C., Shin, J., and Cerrina, F., "Fabrication of ultralow-loss Si/SiO_2 waveguides by roughness reduction," *Opt. Lett.*, vol. 26, pp. 1888–1890, 2001.

[40] Baude, P. F., Ye, C., Tamagawa, T., and Polla, D. L., "Fabrication of sol-gel derived ferroelectric $Pb_{0.865}La_{0.09}Zr_{0.65}Ti_{0.35}O_3$ optical waveguides," *J. Appl. Phys.*, vol. 73, pp. 7960–7962, 1993.

[41] Escoubas, L., Huguet-Chantome, P., Jelinek, M., Flory, F., Drouard, E., Lancok, J., Simon, J. J., and Mazingue, T., "Optical and electro-optical properties of pulse laser deposited PLZT thin films," *Opt. Eng.*, vol. 42, pp. 3579–3584, 2003.

[42] Jin, G. H., Zou, Y. K., Fuflyigin, V., Liu, S. W., Lu, Y. L., Zhao, J., and Cronin-Golomb, M., "PLZT film waveguide Mach-Zehnder electrooptic modulator," *J. Lightwave Technol.*, vol. 18, pp. 807–812, 2000.

[43] Dale, G., Langford, R. M., Ewen, P. J. S., and Reeves, C. M., "Fabrication of photonic band gap structures in $As_{40}S_{60}$ by focused ion beam milling," *J. Non-Cryst. Solids*, vol. 266, pp. 913–918, 2000.

[44] Cryan, M. J., Hill, M., Sanz, D. C., Ivanov, P. S., Heard, P. J., Tian, L., Yu, S., and Rorison, J. M., "Focused ion beam-based fabrication of nanostructured photonic devices," *IEEE J. Quantum Electron.*, vol. 11, pp. 1266–1277, 2005.

[45] Johnson, S. G., Fan, S., Villeneuve, P. R., Joannopoulos, J. D., and Kolodziejski, L. A., "Guided modes in photonic crystal slabs," *Phys. Rev. B*, vol. 60, pp. 5751–5758, 1999.

[46] Xu, X., Chen, H., Xiong, Z., Jin, A., Gu, C., Cheng, B., and Zhang, D., "Fabrication of photonic crystals on several kinds of semiconductor materials by using focused-ion beam method," *Thin Solid Films*, vol. 515, pp. 8297–8300, 2007.

[47] Schilling, A., Adams, T., Bowman, R. M., and Gregg, J. M., "Strategies for gallium removal after focused ion beam patterning of ferroelectric oxide nanostructures," *Nanotechnology*, vol. 18, p. 035301, 2007.

[48] Weissenberger, D., Durrschnabel, M., Gerthsen, D., Perez-Willard, F., Reiser, A., Prinz, G. M., Feneberg, M., Thonke, K., and Sauer, R., "Conductivity of single ZnO nanorods after Ga implantation in a focused-ion-beam system," *Appl. Phys. Lett.*, vol. 91, p. 132110, 2007.

[49] Takahashi, S., Dawson, P., Zayats, A. V., Bischoff, L., Angelov, O., Dimova-Malinovska, D., Tsvetkova, T.,

and Townsend, P. D., "Optical contrast in ion implanted amorphous silicon carbide nanostructures," *J. Phys. D: Appl. Phys.*, vol. 40, pp. 7492–7496, 2007.

Chapter 10

Conclusions and outlook

Adopting epitaxial (Pb,La)(Zr,Ti)O_3 (PLZT) thin films for planar photonic device applications is motivated by a range of attractive functional properties of this perovskite oxide, such as strong electro-optic response, high remanent polarization, and high transparency at infrared frequencies. Monocrystalline $Pb_{0.92}La_{0.08}Zr_{0.4}Ti_{0.6}O_3$ thin films were grown on $SrTiO_3$(001), MgO(001), and buffered Si(001) substrates by on-axis radio frequency magnetron sputtering. XRD measurements showed that *c*-axis oriented PLZT epilayers can be grown on these substrates with high crystalline quality. The measured surface roughness satisfies the requirements for low-loss optical mode propagation in waveguide devices defined in such films. Electro-optic modulation up to 80 % of the guided light intensity was achieved for a ridge-type Mach-Zehnder interferometer processed in PLZT on MgO(001). Photonic crystal slabs were designed by numerical simulation and defined in the PLZT epilayer by focused ion beam (FIB) etching. The out-of-plane structural asymmetry, such as that introduced by the conical shape of the FIB-etched air holes and the presence of an underlying substrate, was found to impair the optical isolation properties of the photonic crystal slab.

In conclusion, the most significant results emanating from this thesis work are:

- Synthesis of optically transparent, ferroelectric PLZT thin film epilayers of high crystalline quality by sputter deposition.

- Demonstration of electro-optic response in a PLZT thin film Mach-Zehnder interferometer, defined by conventional UV lithography and wet etching techniques.
- Design and fabrication of planar photonic crystal slabs and line-defect waveguides in the PLZT epilayers.

These findings promise unprecedented opportunity for application of such sputter-deposited thin film epilayers in electro-optic and photonic devices.

Suggestions for further work

The electro-optic measurements unveiled a modest Pockels coefficient for the PLZT thin film waveguide devices processed in this study ($\mathfrak{r}_{51} \sim 8.3$ pm/V). Directions for further work may include:

- Post-deposition poling of the PLZT epilayer. With the present configuration of the Mach-Zehnder interferometer, i.e., the optical axis of PLZT oriented along the film *c*-axis (normal to the film plane) and co-planar electrode geometry, such poling may affect the magnitude of the electro-optic response.
- Investigating the dependence of the electro-optic response on the film crystalline orientation, by growing PLZT epilayers with a different orientation, e.g., (111)-oriented PLZT, cf. Chapter 6.3, or by aligning the waveguide device with co-planar electrodes along the [110] direction of the substrate, rather than along the [100] direction.

For Si-integrated thin films, a cladding layer with low refractive index is required between PLZT and the substrate, in order to ensure index guiding and to reduce propagation losses due to optical absorption in the semiconductor substrate. Perovskite oxides which can be prepared with optical grade, e.g., $Pb(Zr,Ti)O_3$ and $BaTiO_3$, are suitable candidates for such thin film heterostructures, with a small lattice mismatch for subsequent growth of the PLZT epilayer. Thus, further work could involve:

- Incorporation of a Pb(Zr,Ti)O_3 undercladding between PLZT and the SRO electrode layer. Growth of epitaxial Pb(Zr,Ti)O_3 thin films on SRO/STO(001), with a crystalline quality similar to that of PLZT, was demonstrated in the present study (unpublished).

- Preparation of a heteroepitaxial thin film stack with $BaTiO_3$ undercladding. Numerical analysis suggests that a $BaTiO_3$ layer of thickness ∼1 µm is sufficient to serve as an undercladding. The growth of epitaxial $BaTiO_3$ thin films of high crystalline quality on STO(001) substrate by pulsed layer deposition was demonstrated in the present study (unpublished).

- Increasing the thickness of the optically transparent STO buffer layer to ∼1 µm. The 8 nm MBE-deposited STO buffer layer is not sufficiently thick to serve as undercladding. The thickness of this layer could be increased by sputter deposition or pulsed laser deposition of STO on the buffered Si(001) substrate.

- Incorporation of MgO as undercladding, possibly by e-beam evaporation on STO-buffered Si(001).

Appendix A

Electromagnetic waves in periodic dielectric media

In general, propagation of electromagnetic waves in a dielectric medium can be described by Maxwell equations [1], which in cgs units read,

$$
\begin{aligned}
\vec{\nabla} \times \vec{E}(\vec{r}, t) &= -\frac{1}{c}\frac{\partial \vec{H}(\vec{r}, t)}{\partial t}, && \text{(A.1)}\\
\vec{\nabla} \times \vec{H}(\vec{r}, t) &= \frac{4\pi}{c}\vec{J}(\vec{r}, t) + \frac{1}{c}\frac{\partial \varepsilon(\vec{r})\vec{E}(\vec{r}, t)}{\partial t}, && \text{(A.2)}\\
\vec{\nabla} \cdot \vec{E}(\vec{r}, t) &= \frac{4\pi\rho}{\varepsilon(\vec{r})}, && \text{(A.3)}\\
\vec{\nabla} \cdot \vec{H}(\vec{r}, t) &= 0, && \text{(A.4)}
\end{aligned}
$$

where $\vec{E}(\vec{r}, t)$ and $\vec{H}(\vec{r}, t)$ are the time-dependent electric and magnetic fields, respectively, c is the wave velocity, $\vec{J}(\vec{r}, t)$ is the free current density, $\varepsilon(\vec{r})$ is the dielectric function, and ρ is the free charge density.

The present discussion is based on the following assumptions; (1) the dielectric function $\varepsilon(\vec{r})$ is linear, i.e., independent of the electric field, (2) the dielectric medium is non-dispersive in the frequency range of interest (optical and near-infrared wavelengths), i.e., $\varepsilon(\vec{r})$ is real for low-loss dielectric materials, (3) there are no free charges and currents in the dielectric medium, i.e., the material contains no sources of electromagnetic radiation, which implies $\vec{J} = 0$, (4) the medium is non-magnetic, i.e., the relative magnetic permeability $\mu_r(\vec{r}) = 1$, (5) there are no sinks or point sources of magnetic and displacement fields in the medium, which implies that the divergence of the electric and magnetic fields both equal zero. For transverse electromagnetic waves, Eqs. A.1 and A.2 can be combined to relate the time-dependent electric $\vec{E}(\vec{r},t)$ and magnetic fields $\vec{H}(\vec{r},t)$ according to,

$$\begin{aligned} \vec{\nabla} \times \left(\frac{1}{\varepsilon(\vec{r})} \nabla \times \vec{H}(\vec{r},t) \right) &= -\frac{1}{c^2} \frac{\partial^2 \vec{H}(\vec{r},t)}{\partial t^2}, && \text{(A.5)} \\ \frac{1}{\varepsilon(\vec{r})} \vec{\nabla} \times \left(\nabla \times \vec{E}(\vec{r},t) \right) &= -\frac{1}{c^2} \frac{\partial^2 \vec{E}(\vec{r},t)}{\partial t^2}, && \text{(A.6)} \end{aligned}$$

commonly referred to as the wave equations.

For harmonic waves with angular frequency ω, i.e., $\vec{E}(\vec{r},t) = \vec{E}(\vec{r})\mathrm{e}^{-j\omega t}$ and $\vec{H}(\vec{r},t) = \vec{H}(\vec{r})\mathrm{e}^{-j\omega t}$, the eigenvalue equation for the magnetic field can be written on the form

$$\vec{\nabla} \times \left(\frac{1}{\varepsilon(\vec{r})} \vec{\nabla} \times \vec{H}(\vec{r}) \right) = \Theta_H \vec{H}(\vec{r}) = \left(\frac{\omega}{c} \right)^2 \vec{H}(\vec{r}). \tag{A.7}$$

This implies that $\vec{H}(\vec{r})$ is completely defined on an infinite domain by a Hermitian eigenvalue problem for which a complete basis exists. An important property of Eq. A.7 and the Maxwell equations is their scale-independent character, i.e., there is no absolute length scale and no fundamental value for the dielectric constant. Hence, reducing the magnitude of the dielectric function $\varepsilon(\vec{r})$ by a factor f_1^2 will not affect the harmonic modes, except for scaling of the frequencies by f_1. Correspondingly, changing the geometric proportions by a factor f_2 results in scaling of the mode frequencies by the same factor [2].

In contrast to the linear differential operator Θ_H in Eq. A.7, the corresponding operator for the electric field,

$$\Theta_E = \frac{1}{\varepsilon(\vec{r})} \vec{\nabla} \times \vec{\nabla} \times, \tag{A.8}$$

is not self-adjoint (i.e., non Hermitian), which implies that the eigenfunctions are not necessarily orthogonal, and a complete basis is not guaranteed [3]. The characteristics of the two differential operators combined with the requirement of a transverse $\vec{H}(\vec{r},t)$ speak in favor of solving the eigenvalue problem for $\vec{H}(\vec{r})$ rather than for $\vec{E}(\vec{r})$.

Bloch's theorem [4], implies that the solutions to Eq. A.7 for wave propagation in a periodic dielectric medium, e.g., a photonic crystal, can be chosen on the form

$$\vec{H}(\vec{r}) = \vec{h}_{\vec{k}}(\vec{r})\mathrm{e}^{i\vec{k}\vec{r}}, \tag{A.9}$$

where $\vec{k} = k_1\vec{b}_1 + k_2\vec{b}_2 + k_3\vec{b}_3$ is an arbitrary wave vector in the first Brillouin zone and $\vec{h}_{\vec{k}}(\vec{r})$ is a function with the same periodicity as the crystal lattice. Substitution of Eq. A.9 into Eq. A.7 yields

$$\left(\vec{\nabla} + i\vec{k}\right) \times \left(\frac{1}{\varepsilon(\vec{r})}\left(\vec{\nabla} + i\vec{k}\right) \times \vec{h}_{\vec{k}}(\vec{r})\right) = \left(\frac{\omega(\vec{k})}{c}\right)^2 \vec{h}_{\vec{k}}(\vec{r}). \tag{A.10}$$

The periodicity of $\vec{h}_{\vec{k}}(\vec{r})$ implies that Eq. A.10 needs only be considered on a finite domain, resulting in a discrete set of eigenvalues for this eigenvalue problem [5]. By solving Eq. A.10 numerically, the eigenfrequencies ω can be plotted as function of the wave vector $\vec{k}$, cf. Figure 4.6.

References

[1] Maxwell, J. C., "A dynamical theory of the electromagnetic field," *Philosophical Transactions of the Royal Society of London*, vol. 155, pp. 459–512, 1865.

[2] Joannopoulos, J. D., Johnson, S. G., Winn, J. N., and Meade, R. D., *Photonic Crystals - Molding the Flow of Light.* New Jersey, USA: Princeton University Press, 2nd ed., 2008.

[3] Sakoda, K., *Optical Properties of Photonic Crystals.* Berlin, Germany: Springer, 2001.

[4] Kittel, C., *Introduction to Solid State Physics.* New York, USA: Wiley, 6th ed., 1986. pp. 163–164.

[5] Johnson, S. G., and Joannopoulos, J. D., *Photonic Crystals - The Road from Theory to Practice.* Massachusetts, USA: Kluwer Academic Publishers, 2002. pp. 27–28.

Appendix B

Basic theory of prism coupling

Assessment of the film thickness d and refractive index n_{film} is based on the measured angles of incidence θ_{in} for which m-lines appear. This requires a set of equations which completely describes the coupling of light. The equations relating d, n_{film}, and θ_{in} cannot be solved on closed form, i.e., they must be solved numerically. The range of propagation vectors that can be excited with a given prism is determined by the refractive index n_{p} and the opening angle α, cf. Figure 3.11 on page 56. The effective refractive index for a waveguide mode of order m is given by [1]

$$N_{\text{m}} = \sin\theta_{\text{in}}\cos\alpha + \sin\alpha\sqrt{n_{\text{p}}^2 - \sin^2\theta_{\text{in}}}. \tag{B.1}$$

For a mode m guided in the thin film, the total phase shift is [2]

$$m\pi = \Gamma - \phi_{\text{upper}} - \phi_{\text{lower}}, \tag{B.2}$$

where Γ is the waveguide phase shift, and ϕ_{upper} and ϕ_{lower} are phase shifts resulting from reflection at the upper and lower boundary of the film, respectively. The waveguide phase shift is defined by

$$\Gamma = kd\sqrt{n_{\text{film}}^2 - N_m^2}, \tag{B.3}$$

where $k = \frac{\omega}{c} = \frac{2\pi}{\lambda}$ is the free space propagation constant. Correspondingly, the phase shift for the reflection at an interface is given by [3]

$$\phi_j = \tan^{-1}\sqrt{\left(\frac{n_{\text{film}}}{n_j}\right)^{2\rho}\left(\frac{N_m^2 - n_j^2}{n_{\text{film}}^2 - N_m^2}\right)}, \tag{B.4}$$

where j denotes the media above or below the film, and $\rho = 0, 1$ indicates the polarization of the propagating light (TE = 0, TM = 1). By solving Eqs. B.1–B.4 numerically, the relation between d, n_{film}, and θ_{in} can be determined. Prism coupling measurements can also be used to assess the optical anisotropy of thin films [4].

References

[1] Ulrich, R., and Torge, R., "Measurement of thin film parameters with a prism coupler," *Appl. Opt.*, vol. 12, pp. 2901–2908, 1973.

[2] Tien, P. K., "Light waves in thin film and integrated optics," *Appl. Opt.*, vol. 10, pp. 2395–2413, 1971.

[3] Tang, X., Yuan, Y., Wongchotigul, K., and Spencer, M. G., "Dispersion properties of aluminum nitride as measured by an optical waveguide technique," *Appl. Phys. Lett.*, vol. 70, pp. 3206–3208, 1997.

[4] Ay, F., Kocabas, A., Kocabas, C., Aydinli, A., and Agan, S., "Prism coupling technique investigation of elasto-optical properties of thin polymer films," *J. Appl. Phys.*, vol. 96, pp. 7147–7153, 2004.

Appendix C

Design of Mach-Zehnder interferometer

The relevant design parameters and approximations used in the numerical analysis were given in section 9.2. Referring to the coordinate axes in Figure 9.1(a), the transverse electric (TE) modes have fields that are defined by E_{y} and $H \approx H_{\mathrm{z}}$, with a small component H_{x}. Conversely, the transverse magnetic modes have fields that are defined by H_{y} and $E \approx E_{\mathrm{z}}$, with a small component E_{x}.

An important aspect of the design is to minimize the propagation losses for the device. Besides material and waveguide dispersion, light scattering at surfaces and interfaces contributes to the propagation losses. By choosing an appropriate combination of width and height for the ridge waveguide, scattering from the surfaces can be minimized. At the same time, the ridge geometry must provide strong confinement of the propagating (fundamental) mode. Losses associated with mode propagation through waveguide bends depend both on the radius of curvature and on the confinement capability of the ridge. Moreover, the waveguide fabrication process may place constraints on the design parameters.

The physical dimensions of the ridge-type waveguide were chosen so as to provide single-mode propagation, i.e., the waveguide supports the fundamental TE_0 mode, only. Figure C.1 shows the cutoff condition for the TE_1, TE_2, and TE_3 modes for various combinations of ridge height d and width W.

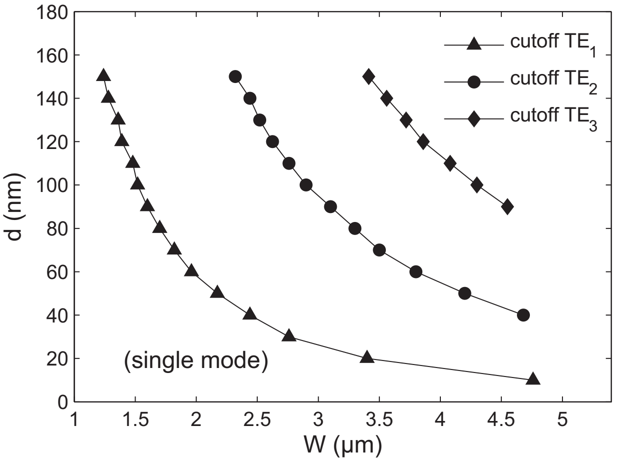

Figure C.1: Cutoff of TE$_1$, TE$_2$, and TE$_3$ for different combinations of d and W.

The results presented below refer to propagation of the TE$_0$ mode. A schematic representation of the Mach-Zehnder (MZ) interferometer is depicted in Figure 9.1(b). The parameters s_x and s_y represent the radius of curvature for the s-bends, which constitute the Y-junction of the interferometer. The mathematical function S used to define the curvature of the bend is given by

$$S(x) = s_y \sin^2\left(\frac{\pi}{2s_x}x\right). \tag{C.1}$$

The power loss for the s-bend versus s_x for three different ridge dimensions is shown in Figure C.2. In this analysis, s_y was fixed at 100 µm. The data shows that for $s_x < 0.8$ mm the losses increase rapidly with decreasing s_x. Also, for s_x larger than ~0.6 mm the bend losses decrease for increasing ridge height, suggesting enhanced light confinement.

Metal electrodes were introduced in a co-planar geometry. The relevant design parameters for the electrodes are shown Figure 9.1(b), and include the interaction length L and the separation g_e between adjacent electrodes. Figure C.3 shows plots of the propagation losses

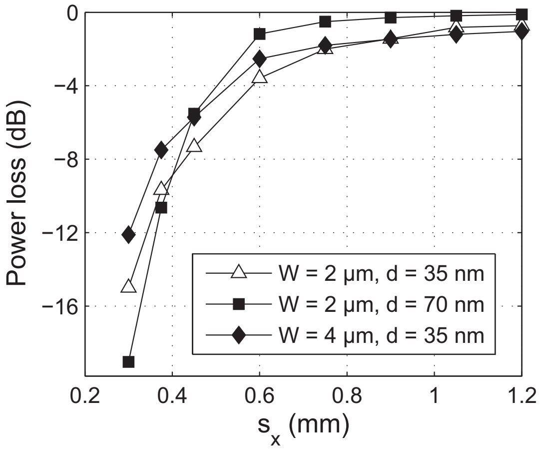

Figure C.2: S-bend power loss vs. s_x for three different ridges and s_y fixed at 50 µm.

for the ridge-type waveguide, caused by optical absorption in the electrodes, as a function of g_e for (a) $W = 2$ µm and (b) $W = 4$ µm. The calculations show that for a given ridge width the losses increase with decreasing height, and that for a given g_e the losses are larger for $W = 4$ µm, compared to $W = 2$ µm. Furthermore, the analysis reveals that the propagation losses are not significantly affected by the thickness of the electrodes, as long as it exceeds ∼10 nm. The data presented in Figure C.3 pertains to an electrode thickness of 250 nm, and the refractive index and absorption coefficient for these electrodes were set at $n = 0.562$ and $\alpha = 7.98 \times 10^5$ cm^{-1}, respectively, corresponding to those for gold at $\lambda = 1550$ nm.

Numerical analysis (data not shown) reveals that for a given electrode gap the electrode absorption is significantly higher for the TE$_1$ mode ($>$ 20 dB/cm for $g_e = 8$ µm) compared to that for the TE$_0$ mode. Hence, the MZ interferometer functions as a mode filter, which implies that the geometry of the ridge is not critical in order to achieve single-mode propagation for the device. As for the electrode gap, there is a trade-off between the magnitude of optical absorption and the strength of the electric field applied across the ridge, i.e., a small gap implies a strong field and high propagation

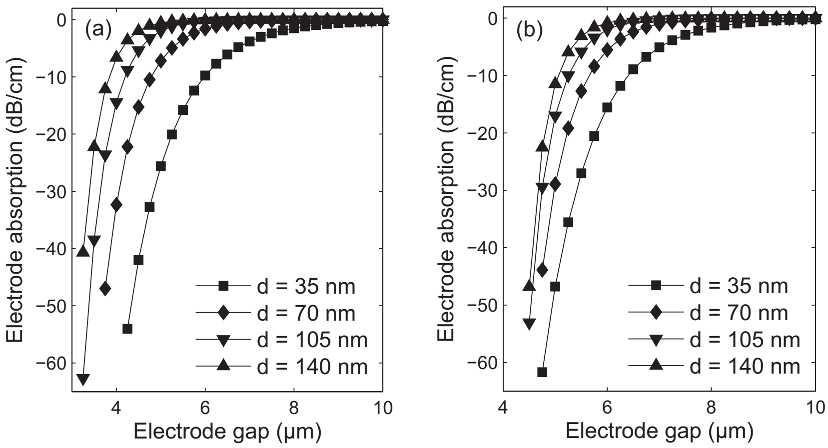

Figure C.3: Electrode absorption vs. electrode gap g_e for different ridge heights and (a) $W = 2$ μm, (b) $W = 4$ μm.

losses.

The phase shift of the MZ interferometer is given by

$$\Gamma(E) = \frac{L\pi}{\lambda}\mathfrak{r}n^3 E, \tag{C.2}$$

where L is the interaction length, $\mathfrak{r}$ is the Pockels coefficient, n is the refractive index, and λ is the wavelength. Rearranging this expression and inserting for V/g_e for E lead to an interaction length

$$L = \frac{g_\text{e}\lambda}{\mathfrak{r}n^3 V_\pi}, \tag{C.3}$$

where V_π denotes the *half-wave voltage*, which corresponds to the voltage required to induce a phase shift π between light in the two branches of the MZ interferometer. For $g_\text{e} = 8$ μm, $V_\pi = 5$ V, and $\mathfrak{r}$ = 50 pm/V, Eq. C.3 yields an interaction length $L \sim 3$ mm.

Based on the data presented in this section, the design parameters shown in Table C.1 were chosen for the MZ interferometer. The total losses were estimated at ~5 dB for the TE_0 mode.

Table C.1: Design parameters for the ridge-type Mach-Zehnder interferometer defined in PLZT on MgO substrate.

Parameter	**Value**
Wavelength	$\lambda = 1550$ nm
Film index	$n_{\text{film}} = 2.45$
Substrate index	$n_{\text{sub}} = 1.715$
Film thickness	$h = 500$ nm
Ridge width	$W = 2$–3 µm
Ridge height	$d = 50$–100 nm
S-bend curvature	$s_x = 1$ mm, $s_y = 100$ µm
Electrode length	$L = 3$ mm
Electrode gap	$g_{\text{e}} = 8$ µm
Electrode thickness	50–250 nm

Appendix D

Computational techniques

The growing interest in photonic crystals can to a large extent be ascribed to recent advances in micro- and nanofabrication processing technologies. However, it still remains a challenge to fabricate structures with a periodicity on the scale of the optical wavelength. Hence, it is imperative to start with an appropriate design. Quantitative predictions for periodic dielectric systems commonly derive from numerical calculations based on Maxwell equations. A number of different algorithms have been proposed for simulations of photonic crystals, including the plane wave expansion method [1, 2], the beam propagation method [3], the transfer matrix method [4], the diffraction grating approach [5], the scattering matrix method [6], the multiple scattering technique [7, 8], the eigenmode expansion method [9], the finite element method [10, 11], and the finite-difference time-domain [12, 13] method. In the present work, the numerical analysis was carried out using the plane wave expansion (PWE) and the finite-difference time-domain (FDTD) methods.

Plane wave expansion

The PWE method involves expanding the periodic function $\vec{h}_{\vec{k}}(\vec{r})$ in a Fourier series and inserting this expansion in Eq. A.10. The Fourier expansion is truncated to a finite number of terms, N, which yields a generalized eigenvalue problem [14]

$$A\vec{h} = \omega^2 B\vec{h}, \tag{D.1}$$

where $\vec{h}$ is the eigenvector and A and B are $N \times N$ matrices. Here, the discretization is chosen so that A and B are Hermitian and B is positive definite [15], whereas the transversality constraint is imposed by choosing a basis that is inherently transverse [14].

MIT Photonic-Bands (MPB) [14] is a freely available software package[1] which computes the eigenmodes of periodic dielectric structures, based on a preconditioned conjugate-gradient minimization [16] of the block Rayleigh quotient [17] in a plane wave basis. To this end, expansion in terms of plane waves $\mathrm{e}^{i\vec{G}\cdot\vec{r}}$ is adopted, where $\vec{G}$ is the reciprocal lattice vector. An iterative eigensolver algorithm [18] is used to obtain an initial value for the eigenvector $\vec{h}$ and to run a number of recursive steps in order to minimize the electromagnetic energy functional, also referred to as Rayleigh quotient minimization, given by [14]

$$\omega_0^2 = \min \frac{\vec{h}^\dagger A\vec{h}}{\vec{h}^\dagger B\vec{h}}, \tag{D.2}$$

where ω_0^2 is the smallest eigenvalue and † denotes the conjugate transpose.

Finite-difference time-domain

The FDTD method [12] is widely used for numerical simulations of electromagnetic wave propagation in real space [13]. The algorithm is based on solving Eqs. A.1–A.4 in a discretized domain, for which the cells of the computational grid are congruent. This is achieved by using a uniform Cartesian grid with a rectangular unit cell and a staircase approximation for features that are not parallel to the coordinate axes of the grid. Figure D.1 shows a schematic of the Cartesian grid unit cell in 3D, commonly referred to as the Yee cell [12].

---

[1] Freely available for download at *http://ab-initio.mit.edu/mpb/*

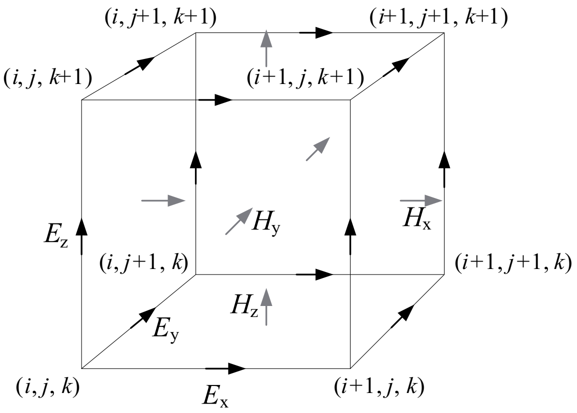

Figure D.1: Schematic of the Cartesian grid unit cell in 3D, along with the electric (E_x, E_y, E_z) and magnetic (H_x, H_y, H_z) field components [19].

For a point on this grid,

$$(i, j, k) = (i\Delta x, j\Delta y, k\Delta z), \tag{D.3}$$

where i, k, j are integers and Δx, Δy, Δz are the grid increments in the x, y, z coordinates, an arbitrary function $F(\vec{r}, t)$ can be expressed on the form,

$$F(i\Delta x, j\Delta y, k\Delta z, n\Delta t) = F^n(i, j, k), \tag{D.4}$$

where n is an integer and Δt is the increment in time. By using centered finite-difference expressions for the space and time derivatives, the first partial space derivative of $F(\vec{r}, t)$ in the x-direction becomes,

$$\frac{\partial F}{\partial x} = \frac{F^n(i + 1/2, j, k) - F^n(i - 1/2, j, k)}{\Delta x} + O\left[(\Delta x)^2\right] \tag{D.5}$$

when evaluated at a fixed time. The corresponding expression for the time derivative of $F(\vec{r}, t)$ evaluated at a fixed point in space is given by

$$\frac{\partial F}{\partial t} = \frac{F^{n+1/2}(i, j, k) - F^{n-1/2}(i, j, k)}{\Delta t} + O\left[(\Delta t)^2\right]. \tag{D.6}$$

The complete set of equivalent finite-difference equations for the Maxwell equations is derived from Ref. 12, where a scheme referred to as *leapfrog* is used to obtain the time evolution of $\vec{E}$ and $\vec{H}$, i.e., the $\vec{E}$-field at a given instant in time is computed and stored, based on the $\vec{H}$-field acquired in the previous time step, and vice versa. This time-stepping process is lossless, which implies that the waves do not decay upon propagating through the computational grid, e.g., due to a non-physical artifact of the process itself.

It is essential to define an appropriate grid size in order to prevent significant changes to the electromagnetic field over one increment in space. For accurate results, an increment in space corresponding to a small fraction of the wavelength must be adopted. Typically, at least 10–20 samplings per wavelength are required. Moreover, the time and space increments are closely interrelated. In order to ensure numerical stability of the algorithm, this relation must comply with the following condition [12],

$$\sqrt{(\Delta x)^2 + (\Delta y)^2 + (\Delta z)^2} > c\Delta t. \tag{D.7}$$

In the present work, FDTD simulations of photonic crystal slabs (PCSs) were carried out using commercially available software[2]. This package is implemented with a *forward difference* algorithm, which implies that the curl of the electric field is computed from the difference between the field vector in adjacent cells of the computational grid with a forward increment δ, i.e., $\Delta_\delta F = F(x+\delta) - F(x)$, whereas the curl of the magnetic field is computed from a backward increment, $\Delta_\delta F = F(x) - F(x-\delta)$. Numerical stability of the algorithm is ensured by adopting a time interval which complies with the Courant stability criterion [20].

Boundary conditions

A computational domain of finite size is required for numerical simulations, mainly due to the limited storage capacity (memory resources) of a computer. Thus, boundary conditions must be defined

---

[2] CrystalWave ver. 4.0, Photon Design Ltd.

for the outer perimeter of the computational domain, without introducing significant error in the computation. In the present study, periodic boundary conditions were adopted for the numerical analysis in the frequency domain, whereas a perfectly matched layer was used for the FDTD simulations.

Periodic boundary conditions

MPB makes use of the periodicity of the photonic crystal lattice by imposing periodic boundary conditions. This implies defining a computational unit cell which is periodically repeated in all spatial directions. Thus, the eigenvalue problem (Eq. A.10) can be solved for this unit cell with general validity for the entire PCS [21]. The schematic in Figure D.2(a) illustrates periodic boundaries applied to the computational unit cell for a PCS. The resulting structure consists of a vertically repeated sequence of PCSs which extends infinitely in the x-y plane. In order to eliminate coupling between guided modes in adjacent PCSs, a unit cell with sufficient vertical size (z-period) is required. In MPB, only the Bloch states (guided modes) for the infinitely extended structure are calculated, i.e., the nonguided (leaky) modes are neglected.

Line-defects defined in PCSs break the translation symmetry of the 2D crystal lattice. By assuming waveguide modes that are strongly localized to the line-defect, a computational domain consisting of several unit cells, i.e., a *supercell*, can be defined [18, 22]. Figure D.2(b) shows a schematic of a $1a \times 4a$ supercell constructed around a line-defect waveguide formed in a hexagonal 2D crystal lattice. This supercell represents the new unit cell of the system, and periodic boundaries can be applied at its perimeter. The localized modes decay exponentially away from the line-defect. Thus, by increasing the size of the supercell the solution converges exponentially to the desired isolated-defect solution. The periodicity of the supercell is artificial, which may result in spurious interactions between neighboring defect sites. The relevance of these interactions decreases exponentially with increasing size of the supercell. In practice, only a few extra periods of the thin film photonic crystal needs to be included on each side of the line-defect in order to

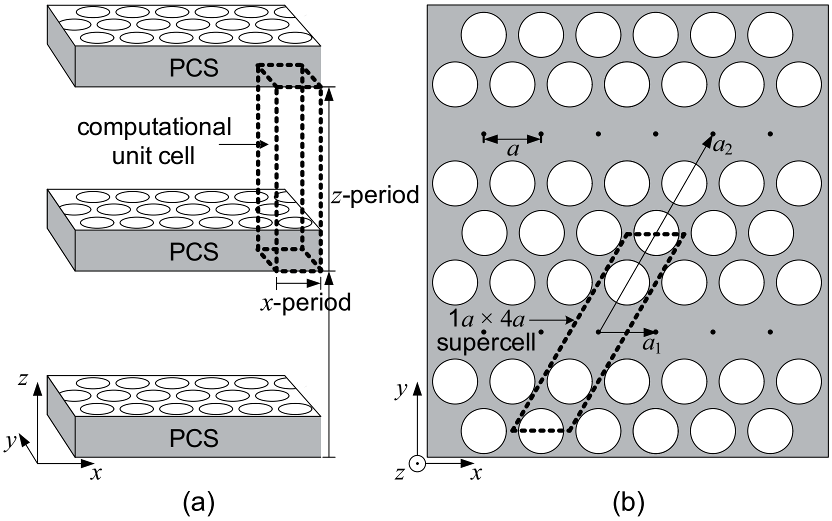

Figure D.2: Schematic of (a) a computational unit cell for a PCS repeated periodically in the x-, y-, and z-direction, and (b) a supercell (1a × 4a) constructed around a line-defect waveguide formed in a hexagonal 2D crystal lattice. a_1 *and* a_2 *are the basis vectors of the superlattice.*

ensure convergence.

Perfectly matched layer

A perfectly matched layer (PML) is a virtual, absorbing material which is added to the edges of the computational domain in order to eliminate reflections from outgoing (radiating) waves [23–26]. The PML allows unbounded electromagnetic problems to be solved with FDTD simulations [27]. The schematic in Figure D.3 shows a cross-section of the computational domain adopted in the present FDTD analysis, with a PML added next to the domain boundary. The reflectance of a plane wave striking the vacuum-PML interface is zero for all frequencies and angles of incidence [23].

In the PML medium, the electromagnetic fields are split in two *non-physical* fields, a technique referred to as the field splitting technique, and losses are assigned individually to each field component. Thus, the PML is an artificial damping layer of finite width, where a

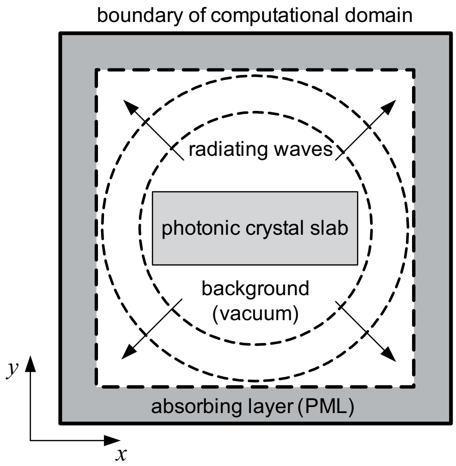

Figure D.3: Schematic of an absorbing layer (PML) added next to the boundary of the computational domain, absorbing outgoing waves without reflection.

modified set of equations have to be solved. It can be shown that for a TE polarized wave propagating in the z-direction, for which the electric field vector forms an angle φ with the y-axis, the wave function Ψ for the TE wave and the impedance Z of the PML medium are given by [23],

$$\Psi = \Psi_0 \mathrm{e}^{j\omega(t-(x\cos\varphi+y\sin\varphi)/c)}\mathrm{e}^{-\frac{\sigma_x\cos\varphi}{\varepsilon_0 c}x}\mathrm{e}^{-\frac{\sigma_y\sin\varphi}{\varepsilon_0 c}y}, \qquad (D.8)$$

$$Z = \sqrt{\frac{\mu_0}{\varepsilon_0}}, \qquad (D.9)$$

where ω is the angular frequency, t is the time, c is the speed of light, σ_x and σ_y correspond to electric conductivities, μ_0 is the free space permeability, and ε_0 is the free space permittivity.

References

[1] Griffin, P., Nagel, P., and Koshel, R. D., "The plane-wave expansion method," *J. Math. Phys.*, vol. 15, pp. 1913–1917, 1974.

[2] Leung, K. M., and Liu, Y. F., "Full vector wave calculation of photonic band structures in face-centered-cubic dielectric media," *Phys. Rev. Lett.*, vol. 65, pp. 2646–2649, 1990.

[3] Koshiba, M., Tsuji, Y., and Hikari, M., "Time-domain beam propagation method and its application to photonic crystal circuits," *J. Lightwave Technol.*, vol. 18, pp. 102–110, 2000.

[4] Pendry, J. B., and MacKinnon, A., "Calculation of photonic dispersion relations," *Phys. Rev. Lett.*, vol. 69, pp. 2772–2775, 1992.

[5] Lalanne, P., and Benisty, H., "Out-of-plane losses of two-dimensional photonic crystals waveguides: Electromagnetic analysis," *J. Appl. Phys.*, vol. 89, pp. 1512–1514, 2001.

[6] Whittaker, D. M., and Culshaw, I. S., "Scattering-matrix treatment of patterned multilayer photonic structures," *Phys. Rev. B*, vol. 60, pp. 2610–2618, 1999.

[7] Tayeb, G., and Maystre, D., "Rigorous theoretical study of finite-size two-dimensional photonic crystals doped by microcavities," *J. Opt. Soc. Am. A, Opt. Image Sci.*, vol. 14, pp. 3323–3332, 1997.

[8] Boscolo, S., and Midrio, M., "Three-dimensional multiple-scattering technique for the analysis of photonic-crystal slabs," *J. Lightwave Technol.*, vol. 22, pp. 2778–2786, 2004.

[9] Bienstman, P., and Baets, R., "Optical modelling of photonic crystals and VCSELs using eigenmode expansion and perfectly matched layers," *Opt. Quantum Electron.*, vol. 33, pp. 327–341, 2001.

[10] Bathe, K. J., and Wilson, E. L., *Numerical Methods in Finite Element Analysis.* Princeton, New Jersey: Prentice Hall, 1976.

[11] Hiett, B. P., Generowicz, J. M., Cox, S. J., Molinari, M., Beckett, D. H., and Thomas, K. S., "Application of

finite element methods to photonic crystal modelling," *IEEE Proc.-Sci. Meas. Technol.*, vol. 149, pp. 293–296, 2002.

[12] Yee, K. S., "Numerical solution of initial boundary value problems involving Maxwell's equations in isotropic media," *IEEE Trans. Antennas Propag.*, vol. 14, pp. 302–307, 1966.

[13] Taflove, A., *Computational Electrodynamics: The Finite-Difference Time-Domain Method.* Norwood, MA: Artech House, 1995.

[14] Johnson, S. G., and Joannopoulos, J. D., "Block-iterative frequency-domain methods for Maxwell's equations in a planewave basis," *Opt. Express*, vol. 8, pp. 173–190, 2001.

[15] Joannopoulos, J. D., Johnson, S. G., Winn, J. N., and Meade, R. D., *Photonic Crystals - Molding the Flow of Light.* New Jersey, USA: Princeton University Press, 2nd ed., 2008. pp. 255–257.

[16] Payne, M. C., Tater, M. P., Allan, D. C., Arias, T. A., and Joannopoulos, J. D., "Iterative minimization techniques for ab initio total-energy calculations: molecular dynamics and conjugate gradients," *Rev. Mod. Phys.*, vol. 64, pp. 1045–1097, 1992.

[17] Ismail-Beigi, S., and Arias, T. A., "New algebraic formulation of density functional calculation," *Comp. Phys. Commun.*, vol. 128, pp. 1–45, 2000.

[18] Meade, R. D., Rappe, A. M., Brommer, K. D., Joannopoulos, J. D., and Alerhand, O. L., "Accurate theoretical analysis of photonic band-gap materials," *Phys. Rev. B*, vol. 48, pp. 8434–8437, 1993.

[19] Taflove, A., "Application of the finite-difference time-domain method to sinusoidal steady-state electromagnetic-penetration problems," *IEEE Trans. Electromagn. Compat.*, vol. 22, pp. 191–202, 1980.

[20] Courant, R., Friedrichs, K. O., and Lewy, H., "Über die partiellen differenzengleichungen der mathematischen physik," *Math. Annalen*, vol. 100, pp. 32–74, 1928.

[21] Joannopoulos, J. D., Johnson, S. G., Winn, J. N., and Meade, R. D., *Photonic Crystals - Molding the Flow of Light.* New Jersey, USA: Princeton University Press, 2nd ed., 2008.

[22] Sakoda, K., *Optical Properties of Photonic Crystals.* Berlin, Germany: Springer, 2001.

[23] Berenger, J. P., "A perfectly matched layer for the absorption of electromagnetic waves," *J. Comput. Phys.*, vol. 114, pp. 185–200, 1994.

[24] Katz, D. S., Thiele, E. T., and Taflove, A., "Validation and extension to three dimensions of the Berenger PML absorbing boundary condition for FD-TD meshes," *IEEE Microwave and Guided Wave Letters*, vol. 4, pp. 268–270, 1994.

[25] Rickard, Y. S., Georgieva, N. K., and Huang, W. P., "A perfectly matched layer for the 3-D wave equation in the time domain," *IEEE Microwave Wireless Comp. Lett.*, vol. 12, pp. 181–183, 2002.

[26] Rickard, Y. S., Georgieva, N. K., and Huang, W. P., "Application and optimization of PML ABC for the 3-D wave equation in the time domain," *IEEE Trans. Antennas Propagat.*, vol. 51, pp. 286–295, 2003.

[27] Berenger, J. P., "Three-dimensional perfectly matched layer for the absorption of electromagnetic waves," *J. Comput. Phys.*, vol. 127, pp. 363–379, 1996.

Index